The synthesis and characterization of semiconductor nanorods as active materials for light emitting diodes

The Synthesis and Characterization of Semiconductor Nanorods as Active Materials for Light Emitting Diodes

A Master Thesis Presented to the Department of Chemistry

at the University of Limerick

By

Na Jia

Supervisors:

Prof. Tewfik Soulimane & Dr. Ning Liu

Submitted to the University of Limerick, December 2022

Abstract

This Master's thesis describes the preparation of nanorod (NR) semiconductors and its application in light emitting diodes (LEDs). The synthesis was carried out by the hot injection method and the closely packed nanorods layers were obtained for the LED devices. The assemblies provide a realistic path to incorporate these materials into devices. The technique of fabrication of LED was undertaken by synthesis of II-VI semiconductor nanorods, assembling them using electrophoretic deposition. Typically, the supercrystal films consisting of highly ordered and vertically aligned $CdSe_{1-x}S_x$ nanorods, CdSe nanorod and CdS nanorod were prepared as the emitters which are regarded as one of the most promising LED materials due to their tunable and directional emission spectra, high damage threshold and low energy formation processes. In addition, preparation of highly monodisperse CdSe/CdS core/shell nanorods with tunable aspect ratios is described. The optical properties are compositionally tunable with the size of the CdSe core. Importantly, the influence of reaction time on shape/size control of the CdSe core is explored to achieve the desired nanorod Photoluminescence (PL). The synthetic protocol is reliable to allow good control over the PL of nanorod from green (535nm) to red (621nm), suited for the application in the LEDs with vertical superstructures.

The electrophoretic deposition (EPD) is employed to the fabrication of the emission layer. The green and red NR-LEDs show a peak external quantum efficiency (EQE) of 0.041 % and 0.0003% respectively. This performance is low, the performance can be enhanced by the formation of vertically aligned NRs made by EPD, which can reduce the resistance of the carrier transport and balance the carrier injection.

Declaration

I hereby declare that this submission is my own work and contains no material which has been submitted to any other University or higher education institution or far any academic award in this University. Where use has been made of the work of other people, it has been fully acknowledged and reference accordingly.

Signed: ___________ Date ____/___/____

Acknowledgements

I would first like to thank my supervisors Prof. Tewfik Soulimane and Dr. Ning Liu, as well as my co-supervisor Prof. Christophe Silien. Thank you for accepting me into your wonderful research group. It is such as wonderful journey for my going through this unique research Master experience. These two years have been the most wonderful years of my life. I would like to express my gratitude to the many people who have contributed.

I am grateful for Dr. Ning Liu's guidance and support. Prof. Tewfik Soulimane gave me the freedom and patience to explore independently, which makes me to get more research experience and lab skills. I would also like to thank Prof. Tofail A. M. Syed for providing the financial support and opportunities to my living and research. And also I would like to thank Prof. Christophe Silien, Dr. Pritam Khan and Dr. Ehtsham U haq for the support and help of ASINA project.

Finally, an enormous gratitude to my my family for their support and understanding, my mother would call me every day to comfort and help me in life and mood, and my father would give me support for spirit. Especially to my husband and my daughter, my husband gives me trust and help, so that I can continue to breakthrough myself, to achieve self-value. My daughter's understanding is also an important support for me to concentrate on my research.

Table of Contents

Abstract 2

Declaration 3

Acknowledgements 4

Table of Contents 5

List of Abbreviations 9

List of Publications 11

1. Introduction 12

1.1. Semiconductor Nanocrystal 12

1.2. Nanorods 12

1.3. Importance of the Study 13

1.4. Scope of Thesis 13

Reference 15

2. Literature Review 17

2.1 Nanocrystals 17

2.1.1 General Synthesis Scheme 20

2.1.2 NCs Growth 22

2.1.3 Shape Control 24

2.1.4 Size Control 28

2.1.5 Precursors 33

2.1.6 Ligands ... 35

2.2 Structural Properties of NCs ... 39

2.2.1 Core/Shell Structure ... 40

2.2.2 Alloy ... 41

2.3 Nanorods ... 43

2.4 Electrophoretic Deposition(EPD) ... 46

2.4.1 Source of Dipole Moment ... 46

2.4.2 EPD ... 47

Reference ... 51

3. Experimental Procedures and Characterisation Techniques ... 63

3.1 Synthetic Experimental Equipment ... 63

3.1.1 Hot Injection ... 63

3.1.2 Synthesis Experiment ... 64

3.1.3 Electrophoretic deposition (EPD) ... 65

3.2 Characterisation Techniques ... 66

3.2.1 Photoluminescence (PL) ... 66

3.2.2 Photoluminescence Quantum Yield (PLQY) ... 67

3.2.3 Scanning Electron Microscopy (SEM) ... 69

3.2.4 Ultraviolet-Visible Spectroscopy (UV-Vis) ... 71

3.2.5 X-ray diffraction (XRD) ... 73

3.3 LED Fabrication and Characterization ... 77

Reference 79

4. The Synthesis and Characterization of CdSe, CdS and $CdSe_{1-x}S_x$ Nanorods 81

4.1 Introduction 81

4.2 Experiments 83

4.2.1 Chemicals 83

4.2.2 Synthesis of Cadmium Selenium Nanorods 84

4.2.3 Synthesis of Cadmium Sulfide Nanorods 84

4.2.4 Synthesis of Cadmium Selenium Sulfide Nanorods 85

4.3 Characterization 85

4.4 Results and Discussion 86

4.5 Conclusion 95

Reference 96

5. The Synthesis and Characterization of CdSe/CdS core/shell Nanorods and Their Application in RGB LEDs 99

5.1 Introduction 99

5.2 Experiments 101

5.2.1 Chemicals 101

5.2.2 Synthesis of Cadmium Selenium core 101

5.2.3 Synthesis of Cadmium Selenium / Cadmium Sulphide Core/Shell Nanorods 102

5.2.4 Device Fabrication 102

5.3 Results and Discussion 103

Reference 115

6. Future Work 120

6.1 Blue-Emitting Perovskite (CsPbX3; X = Cl, Br, I) Nanorods 120

6.2 Chemicals and Synthesis 121

6.3 Result and Discussion 121

6.4 Conclusion 122

Reference 123

List of Abbreviations

(NC) Nanocrystal

(CdSe) Cadmium Selenium

(CdS) Cadmium Sulphide

(CdSeS) Cadmium Selenium Sulphide

(eV) Electron Volt

(QD) Quantum Dot

(TOPO) Trioctylphospine oxide

(HPA) Hexylphosphonic acid

(V) Volt

(ITO) Indium Tin Oxide

(TEM) Transmission Electron Microscopy

(SEM) Scanning Electron Microscopy

(mV) Mili-Volt

(TOP) Trioctylphosphine

(XRD) X-ray Diffraction

(WZ) Wurtzite

(nm) Nanometre

(DC) Direct Current

(CdO) Cadmium Oxide

(ODPA) Octadecylphosphonic acid

(TDPA) Tetradecylphosphonic acid

(HPA) n- hexylphosphonic acid

(μL) Microlitre

(kV) Kilovolt

(IPA) Isopropanol

(PL) Photoluminescence

(EL) Electroluminescence

(UV-Vis) Ultraviolet-Visible Spectroscopy

(EPD) Electrophoretic Deposition

(LED) Light-emitting diode

(LCD) Liquid Crystal Display

(NR) Nanorod

(PLQY) Photoluminescence Quantum Yield

(EQE) External Quantum Efficiency

List of Publications

Patent

1. Yongliang Zhang; Na Jia; Christophe Silien; Kevin M. Ryan, Ning Liu. (2022) Inverted All-inorganic Light Emitting Diodes Via by Electrophoretic Deposition Approach. (Invention Disclosure)

1. Introduction

1.1. Semiconductor Nanocrystals

Semiconductor Nanocrystals (NCs) has attracted much attention due to its abundant raw materials, stable chemical properties [1]. The past few decades have witnessed remarkable progress in the wet-chemical colloidal synthesis of semiconductor nanocrystals (NCs), where one can grow anisotropic NCs in large quantity with relatively high uniformity and often with structural complexity. The progress has placed intricate control over size, shape, and composition of anisotropic NCs and their assembled structures into the hands of even modestly equipped researchers. This has been a boon not only to application-based technological development but also to our understanding of the physics of anisotropic quantum confinement and directional interparticle interactions [2].

Therefore semiconductor nanocrystals are a new class of functional materials developed in recent years. They have potential applications in solar cells, light-emitting diodes, photodetectors, biological markers, nonlinear optics and other fields [3].

1.2. Nanorods

One type of NCs, which gained considerable attention in recent years, is seeded nanorods. These NCs, in which a core of type of semiconductor is embedded in a rod shaped shell of another type of semiconductor, have become a major and significant branch in the heterostructured anisotropic NCs family. Such particles share unique properties which emerge from the integration of domains with different dimensions and dimensionalities in the same particle [4]. There are several unique optical properties that can make NRs potentially more appealing than quantum dots (QDs) [5]. Semiconductor NRs, in addition to the tunable range of wavelengths of the emitted light (achieved for example by the variation of the NR diameter or the diameter of core in a core-shell configuration), also exhibiting linearly polarized emission, such as in the case of CdSe NRs and CdSe/CdS “dot-in-a-rod”nanocrystals [6]. Additionally, NRs exhibit a larger Stokes shift, faster radiative decay and slower bleaching kinetics than QDs [7].

1.3. Importance of the Study

It has been shown that various types of semiconductor nanorods have unique optical properties that make them appealing for applications in solar cells, light emitting diodes, lasers and in cell labeling [8] [9] [10]. In general, the incorporation of anisotropic nanoparticles in NCs has been investigated to achieve-long range alignment, large scale orientation manipulation, and for faster switching speed of NCs devices [11] [12] [13]. As an example Acharya et al. [14] found that nanorods of proper dimension couple locally with the NC director field in a favorable energetic configuration which enhances long range ordering and device performance [15].

CdSe/CdS core/shell nanorods present very appealing optical characteristics and similar materials were already employed in order to study enhanced orientational photorefractive effects generated in doped nematic crystals [16] [17].

1.4. Scope of Thesis

Chapter 1 Introduces the research field of nanocrystal and nanorods, outlining the recent progress and the applications of the nanorods.

Chapter 2 The background of nanorods and semiconductor nanocrystals are reviewed.

Chapter 3 The equipment, methods and experimental techniques used in the whole process of research and experiment are introduced.

Chapter 4 The synthesis and characterization of CdSe, CdS and $CdSe_{1-x}S_x$ nanorods are described.

Chapter 5 The synthesis and characterization of CdSe/CdS core/shell nanorods are described, as well as the regulation of red light to green light.

Chapter 6 Future work.

Reference

1. Yin, Y. and A.P. Alivisatos, *Colloidal nanocrystal synthesis and the organic–inorganic interface.* Nature, 2005. **437**(7059): p. 664-670.
2. Kim, D. and D.C. Lee, *Surface ligands as permeation barrier in the growth and assembly of anisotropic semiconductor nanocrystals.* The Journal of Physical Chemistry Letters, 2020. **11**(7): p. 2647-2657.
3. Van Embden, J., et al., *Review of the synthetic chemistry involved in the production of core/shell semiconductor nanocrystals.* Australian Journal of Chemistry, 2007. **60**(7): p. 457-471.
4. Sitt, A., I. Hadar, and U. Banin, *Band-gap engineering, optoelectronic properties and applications of colloidal heterostructured semiconductor nanorods.* Nano Today, 2013. **8**(5): p. 494-513.
5. Yong, K.T., et al., *Multiplex imaging of pancreatic cancer cells by using functionalized quantum rods.* Advanced Materials, 2008. **20**(8): p. 1412-1417.
6. Hu, J., et al., *Linearly polarized emission from colloidal semiconductor quantum rods.* Science, 2001. **292**(5524): p. 2060-2063.
7. Shabaev, A. and A.L. Efros, *1D exciton spectroscopy of semiconductor nanorods.* Nano letters, 2004. **4**(10): p. 1821-1825.
8. Scholes, G.D., *Controlling the optical properties of inorganic nanoparticles.* Advanced Functional Materials, 2008. **18**(8): p. 1157-1172.
9. Kislyuk, V. and O. Dimitriev, *Nanorods and nanotubes for solar cells.* Journal of nanoscience and nanotechnology, 2008. **8**(1): p. 131-148.
10. Cozzoli, P.D., T. Pellegrino, and L. Manna, *Synthesis, properties and perspectives of hybrid nanocrystal structures.* Chemical Society Reviews, 2006. **35**(11): p. 1195-1208.
11. Yada, M., J. Yamamoto, and H. Yokoyama, *Direct observation of anisotropic interparticle forces in nematic colloids with optical tweezers.* Physical review letters, 2004. **92**(18): p. 185501.

12. Wu, K.-J., et al., *CdS nanorods imbedded in liquid crystal cells for smart optoelectronic devices.* Nano Letters, 2007. **7**(7): p. 1908-1913.

13. Lapointe, C., et al., *Elastic torque and the levitation of metal wires by a nematic liquid crystal.* Science, 2004. **303**(5658): p. 652-655.

14. Acharya, S., et al., *Nanorod-Driven Orientational Control of Liquid Crystal for Polarization-Tailored Electro-Optic Devices.* Advanced Materials, 2009. **21**(9): p. 989-993.

15. Petti, L., et al., *Optically induced light modulation in an hybrid nanocomposite system of inorganic CdSe/CdS nanorods and nematic liquid crystals.* Optical Materials, 2010. **32**(9): p. 1011-1016.

16. Khoo, I.-C., K. Chen, and Y.Z. Williams, *Orientational photorefractive effect in undoped and CdSe nanorods-doped nematic liquid crystal—bulk and interface contributions.* IEEE Journal of selected topics in quantum electronics, 2006. **12**(3): p. 443-450.

17. Suh, D.J., et al., *Observation of the photorefractive behaviors in the polymer nanocomposite based on p-PMEH-PPV/CdSe-nanoparticle matrix.* Optical Materials, 2003. **21**(1-3): p. 365-371.

2. Literature Review

2.1 Nanocrystals

Colloidal nanocrystals are sometimes referred to as ‘artificial atoms’ because the density of their electronic states-which controls many physical properties-can be widely and easily tuned by adjusting the crystal's composition, size and shape. The combination of size- and shape-dependent physical properties and ease of fabrication and processing makes nanocrystals promising building blocks for materials with designed functions [1] [2], for example, as inorganic fluorophores in biomedical assays. But the ability to control the uniformity of the size, shape, composition, crystal structure and surface properties of the nanocrystals is not only of technological interest: access to defined nanoscale structures is essential for uncovering their intrinsic properties unaffected by sample heterogeneity [3].

The physical and chemical properties of a material are determined by the type of motion allowed for its electrons to execute. The latter is determined by the space in which the electrons are confined. Unbound (unconfined) electrons have motion that is not quantized and can thus absorb any amount of energy given to them and use it simply to move more rapidly. Once bound in an atom, a molecule or a material, their motion becomes highly confined and quantization sets in. The allowed types of motion in atomic or molecular orbitals are found to have well-defined energies that are separated from one another. The smaller the space in which the bound motion takes place, (i.e., the stronger the confinement) the larger the energy separation between the allowed energies of the different types of motion becomes. The nuclear confinement is the strongest type of confinement of the motion of subatomic particles. The motion of the nucleons within the atomic nucleus is confined to the femtometer scale. This is followed by electronic confinement in atoms. In the hydrogen atom, the electron is confined to a length scale of ~ 50 pm [2] [4].

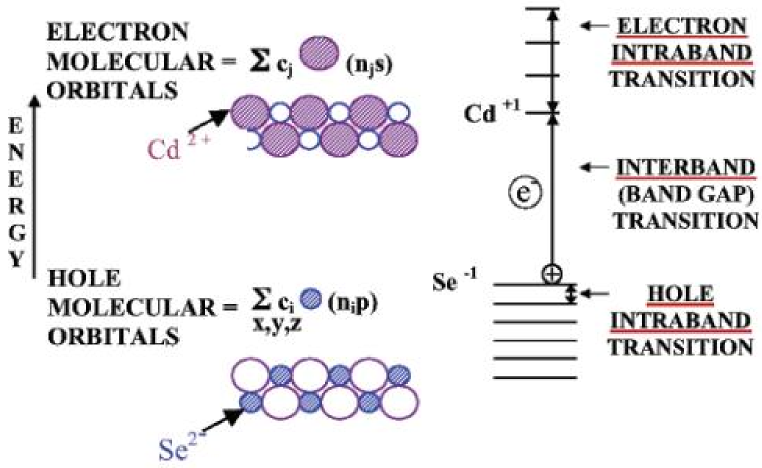

Figure 2.1. Molecular orbitals are different in a semiconductor nanoparticle than in a conducting polymer: (left) the molecular orbitals of the hole (bottom) in the Se^{2-} electronic system and the electron (top) in the Cd^{2+} electronic system in a CdSe semiconductor nanoparticle; (right) the band gap (interband or HOMO to LUMO) transition (separating the electron and hole) and the different intraband transitions of the electron (top) and hole (bottom) in a semiconductor nanoparticle. The interband transition is a charge transfer type of transition from the Se^{2-} MOs to the Cd^{2+} MOs to form a delocalized Cd^{+} and Se^{-} electronic system in the band gap state [2].

In a semiconductor nanoparticle like CdSe or HgS, the occupied molecular orbitals (MOs) are made of a linear combination of atomic orbitals (ao) on the negatively charged anions (e.g., S^{2-}, Se^{2-}, ...), while the unoccupied MOs are made of ao on the metallic cations (Cd^{2+}, Hg^{2+}, ...) (Figure 2.1). Thus, the band gap excitation involves a charge transfer of an electron from the HOMO in the Se^{2-} or S^{2-} electronic system to the vacant LUMO of the Cd^{2+} or Hg^{2+} (the bottom of the conduction band in the bulk). This creates a hole in the HOMO (which corresponds to the top of the valence band in the bulk). Thus, the holes always occupy the anion MOs, while the excited electrons occupy the cation MOs. Because of this and the high dielectric constant of the semiconductor material, the charge carriers in a semiconductor nanoparticles are weakly coupled and thus are not strongly correlated. They can be excited, be trapped, and relax nonradiatively almost independently of one another. Furthermore, excitation of the excited electron formed in band gap absorption takes place between different

MOs of the metal cation. The holes formed in the band gap absorption can be excited to other higher energy anion MOs. The excitation of either charge carrier formed in the band gap absorption is called the intraband excitation, while the band gap excitation itself is termed the interband excitation (Figure 2.1). In II-VI semiconductors, the different MOs made from the n p atomic orbitals of the negatively charged anion are much closer to one another in energy than those formed from the five s atomic orbitals on the positively charged cations. For this reason, the electron intraband absorption occurs at higher energy than the hole intraband absorption, which is observed in the infrared region [2].

Over the past decades, chemists have come to appreciate that, from the point of view of synthesis, colloidal inorganic nanocrystals can be thought of as a class of macromolecule, with preparative strategies that are similar in many ways to those employed with artificial organic polymers. For nanocrystals of 1-100 nm diameter, it is possible to define the average and the dispersion of the diameter, as well as the aspect ratio. The degree of precision with which the desired structure is synthesized is similar to that achieved with synthetic polymers, where the preparative methods at our disposal allow us to define the mean number of monomer units in a polymer and the variance of this number, and to build complex topologies through joining or branching of simpler macromolecules. As with artificial polymers, some principles have now emerged that give us the ability to control the size and shape of colloidal nanocrystals. After more than two decades, impressive progress has been made towards the tailored synthesis of colloidal nanocrystals that have well-defined structures. A wide variety can now be successfully produced using a number of methods, such as co-precipitation in aqueous phase, using reverse micelles as templates, hydrothermal/solvothermal synthesis and surfactant-controlled growth in a hot organic solvent [5] [6] [7].

Quantum dots (QDs) are one of the NCs which are spherical inorganic particles containing a few thousand atoms, with sizes commonly about 2-20 nm [8]. In the last 30 years, a significant amount of research has been reported covering QD synthesis, their fundamental physical properties and potential uses [9]. The attractiveness of QDs for potentially groundbreaking applications lies in the basic property that by varying the size of the QD, the photophysical characteristics of the exciton (electron-hole pair) can be tuned [10]. For example, the electronic structure of QDs can be tuned over a range of energies by varying the size of the QD (Figure 2.2). Also, many potential applications of QDs rely on their ability to combine the robustness of inorganic, crystalline semiconductors with the solution processability and easy handling of solution-phase small molecules.

Figure 2.2. Colloidal cadmium selenide (CdSe) QDs demonstrating a range of fluorescent colors based on variable particle sizes. The QD size increases from green (about 2.5 nm) to red (about 6 nm) [11] .

2.1.1 General Synthesis Scheme

A typical synthesis system for colloidal nanocrystals consists of three components: precursors, organic surfactants and solvents. In some cases, surfactants also serve as solvents. Upon heating a reaction medium to a sufficiently high temperature, the precursors chemically transform into active atomic or molecular species (monomers);

these then form nanocrystals whose subsequent growth is greatly affected by the presence of surfactant molecules. The formation of the nanocrystals involves two steps: nucleation of an initial 'seed' and growth. In the nucleation step, precursors decompose or react at a relatively high temperature to form a supersaturation of monomers followed by a burst of nucleation of nanocrystals. These nuclei then grow by incorporating additional monomers still present in the reaction medium. The three components of a colloidal synthesis are shown in Figure 2.3, the chemistry that occurs with precursors, ligands, and solvents will be discussed later.

The modern field of colloidal nanocrystals started in 1993 with the seminal paper of Murray, Norris, and Bawendi [12]. The formation of CdSe, CdS, and CdTe nanocrystals was reported from dimethylcadmium, tri-n-octylphosphine (TOP), tri-n-octylphosphine oxide (TOPO), and an appropriate chalcogen precursor. This report contained the basic components for the following three decades of research: precursors that convert at high temperature in the presence of surfactants (ligands), thus forming colloidal objects that are organic/inorganic hybrids. Over the years, the field has acquired more control over the nanocrystal size distribution [13], shape [14], composition [15], and heterostructure [16], while at the same time using safer, less toxic precursors [17].

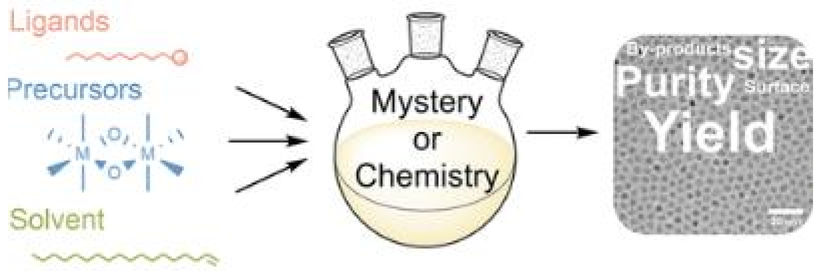

Figure 2.3 The diagram of NCs synthesis with three essential components:precursors, ligands, and solvents [18].

2.1.2 Nanocrystals Growth

The general dependence of the growth rate on the radius of the crystal is illustrated in Figure 2.4. It is interesting to note the presence of a maximum at a radius of 2r. If all crystals present in the solution have a radius larger than this value, the smallest crystals grow fastest, and therefore the size distribution becomes narrower over time. The value of r depends mainly on the overall concentration of free monomers, but also on the reaction temperature and on the surface tension s. During the run of the reaction the concentration of monomers decreases and the critical size shifts to higher values. If the critical size is sufficiently small the system is said to be in the narrowing or size focussing regime. During the run of the synthesis the critical size increases and as soon as the size of maximal growth rate, 2r , has reached a value situated in the lower end of the size distribution of the nanocrystals, the system enters in the broadening regime. Ultimately, when r is larger than the radius of the smallest nanocrystals present, the system enters into the Ostwald ripening regime, which is characterised by a large broadening of the size distribution and more important by a decrease of the total concentration of the nanocrystals. The smallest nanocrystals melt to free monomers that are incorporated into the larger nanocrystals [3].

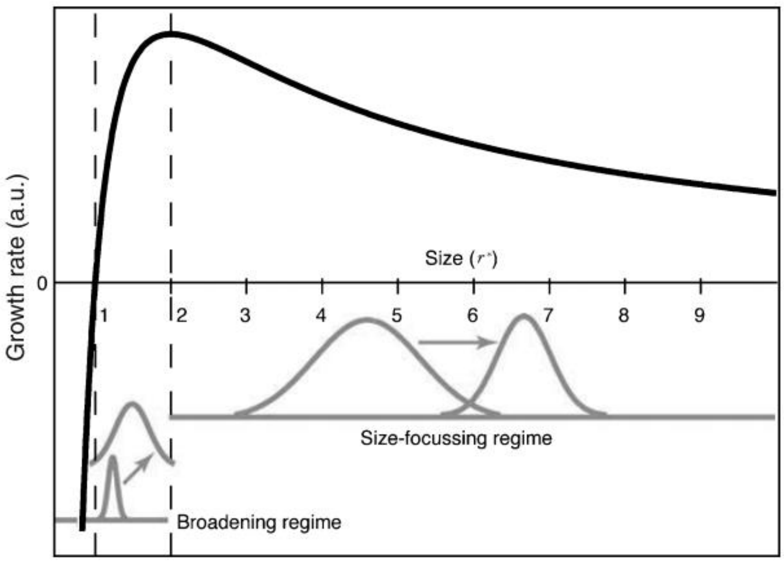

Figure 2.4 Sketch of the growth rate of the nanocrystals in units of the critical size r . As examples two size distributions and their development with time are displayed. Note that in the example for

the broadening regime, the smallest particles are larger than r. Therefore the mean size of the particles still increases. The situation would be different if the size distribution would comprise nanocrystals smaller [3].

In an experiment the effect of the size focusing is limited by the broadness of the initial size distribution, in other words, the nucleation event has a strong influence on the size distribution of the final sample [19]. Ideally the nucleation event should be finished well before the system enters into the diffusion controlled growth regime. The sharpness (in terms of time duration) of this event is therefore of great importance [19]. If on the contrary the nucleation event spans a considerable amount of time, those nanocrystals that nucleated first have grown already too far, resulting in a broad size distribution. In that case the effect of the size focusing might not be sufficient to obtain a reasonably narrow distribution at the desired average size of the nanocrystals. The limiting factor here is that the effect of the size focussing is always accompanied with an overall growth of all nanocrystals.

In some synthesis schemes it is inevitable to consume the reservoir of monomers and thus obtain a broadening of the fluorescence band. In these cases the system can be maintained in focussing regime by repeated injections of fresh monomers [20] [21]. Experimentally it is not always possible to obtain a perfect size distribution. In some cases the distribution is broadened or shows several distinct peaks. A possible, but somewhat laborious way to improve the size distribution is to perform a size selective precipitation after the synthesis is completed [22].

A landmark development in the synthesis of NCs occurred in 1993 with the report of a relatively simple synthetic procedure for CdS, CdSe, and CdTe quantum dots (QDs） with significantly enhanced control over nanoparticle size and the production of a narrow size distribution (<5% in QD diameter) [12]. This breakthrough in the ability to control particle size was largely due to the use of phosphine-chalcogenide precursors, (in this case, based on trin-octylphosphine (TOP)), and a coordinating solvent (in this case, trioctylphosphine oxide (TOPO)). QD size could be continuously tuned from 1.2 to over 11.0 nm with excellent crystal lattice properties equivalent to the bulk material (Figure 2.5). Pyrolysis of the reagent dimethyl cadmium in a hot solvent led to rapid nucleation separated from growth, which allowed for the synthesis of (at that time) relatively large quantities of QDs with highly desirable optical properties [11].

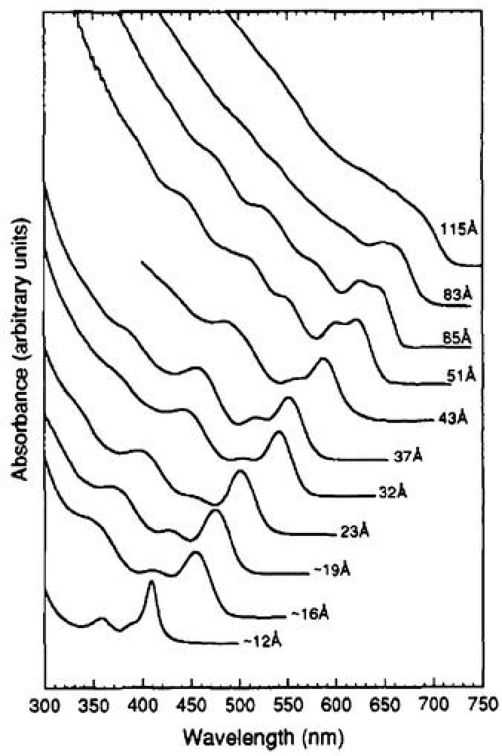

Figure 2.5 . Absorption spectra for cadmium selenide (CdSe) QDs with diameters from 1.2 to 11.5 nm [12].

2.1.3 Shape Control

Mastery over the shape of a nanocrystal enables control of its properties and enhancement of its usefulness for a given application. After controlling the shape of the nanocrystals, the resulting properties are also changed . For metal nanocrystals, shape not only determines their intrinsic physical and chemical properties but also their relevance for electronic, magnetic, optical, catalytic, and sensing applications [14]. With some nanocrystals the faceted shape becomes obvious, as for instance on octahedral PbSe nanocrystals [23], silver nanocubes [24] or pencil-shaped Co nanocrystals [25] (Figure 2.6). Indeed, the growth of spherical crystals is more an exception than the rule. For instance macroscopic quartz is usually found in an elongated shape with six large facets that intersect under an angle of 120 °C. The tip of the crystal shows a series of facets, all inclined with respect to the long axis of the crystal. Generally the shape of a crystal depends on the relative speeds at which the individual facets grow. Here, the speed of growth of a facet is measured as the speed at which the distance of its centre to the centre of the entire crystal increases. The faster a crystal grows on one facet the more likely to disappear is this facet [26].

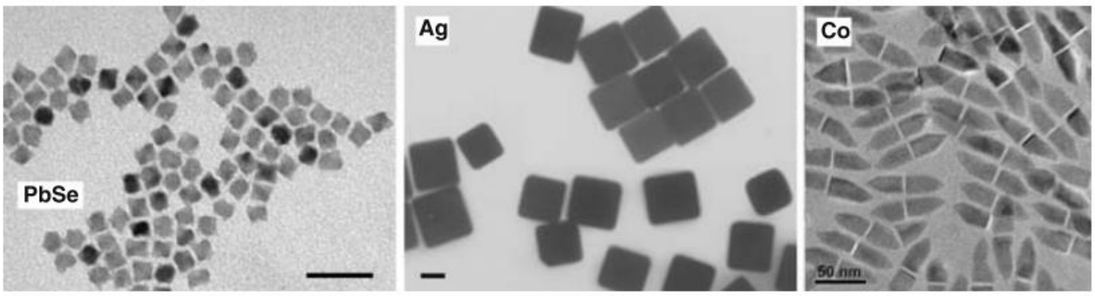

Figure 2.6 Examples of faceting of nanocrystals. TEM images of differently shaped nanocrystals: octahedron-shaped PbSe [23], cube-shaped silver [24] and pencil-shaped Co O [25].

A benchmark preparation is the growth of nearly spherical II–VI and III–V nanocrystals by injection of precursor molecules into a hot surfactant [27] [28]. Peng et al. [29] demonstrated that control of the growth kinetics of the II–VI semiconductor cadmium selenide can be used to vary the shapes of the resulting particles from a nearly spherical morphology to a rod-like one, with aspect ratios as large as ten to one. This method should be useful, not only for testing theories of quantum confinement, but also for obtaining particles with spectroscopic properties that could prove advantageous in biological labeling experiments [30] [31] and as chromophores in light-emitting diodes [32] [33].

In general, the ligand plays an important role in the shape of the NCs. Close to perfect rods with a high aspect ratio were generated at high temperatures and using ODPA as the ligands instead of HPA or TDPA [34]. This is consistent with the relatively fast diffusion at high temperatures and the relatively low reactivity of the complexes with long ligands. Presumably, high temperatures should promote the diffusion flux rapidly flowing toward the fast growth facet, the (001) facet, which is an ideal 1D-growth mode and yields perfect rod-shaped nanocrystals. The longer the rods are, the more difficult such directional diffusion would be, and thus the higher the temperature must be provided. The complex with long ligands may slow the diffusion rate, but its significantly low reactivity may have made a stronger impact, which provides the monomers a longer time for adjusting the position before adhering onto the surface of the nanocrystals. One example of CdSe nanocrystals with a shape close to a perfect rod grown by the mechanisms described in this paragraph is shown on the top of the middle panel in Figure 2.7.

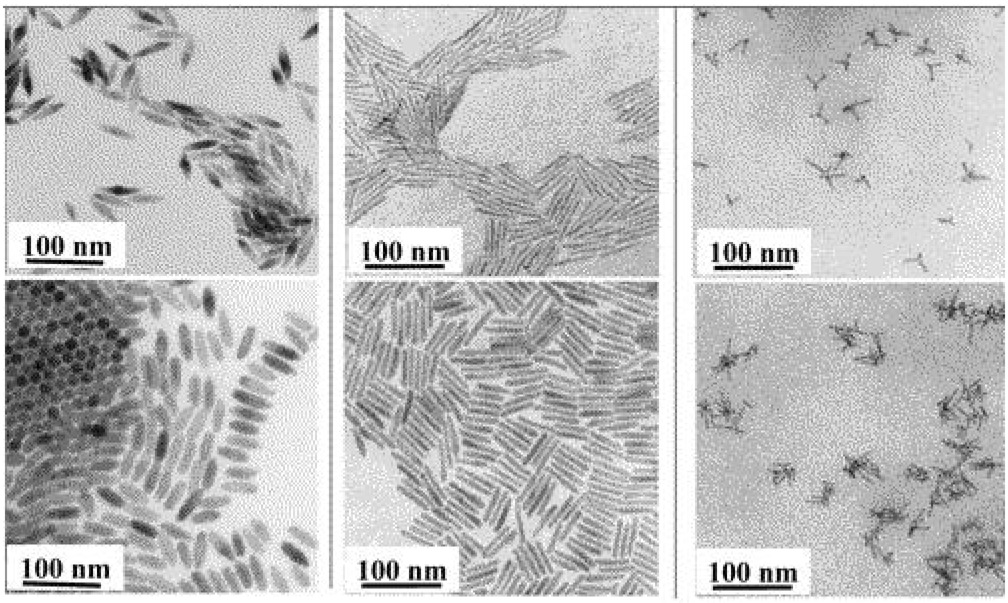

Figure 2.7 As-prepared CdSe nanocrystals with different shapes. Left panel: Rice-shaped nanocrystals synthesized by multiple injections (top) and by a single injection (bottom). Note: Some of the rice-shaped nanocrystals aligned with their c-axis perpendicular to the substrate in the bottom picture. Middle panel: Rod-shaped nanocrystals grown through straight 1D-growth mode (top) and after staying in 1D/2D-ripening for certain amount of time (bottom). Left panel: Branched nanocrystals grown at 300 °C (top) and at 180 °C (bottom) [34].

In CdE (E ¼ S, Se, Te) nanocrystals it serves as the directional axis for the asymmetric growth [35]. In the case of Co nanocrystals in the phase growth along this axis is suppressed [36]. But the asymmetric growth is not restricted to materials that expose a hexagonal structure [37]. CaF_2 nanorods grow in the cubic fluorite structure along the (1 1 1) axis [38]. PbSe grows in the highly symmetric cubic rock salt structure, but with the help of bulky surfactants a unique growth direction can be assigned and nanowires are formed [80]. For the materials of interest in this chapter (CdS, CdSe, CdTe) generally the crystalline structure is the wurtzite structure. For instance, nanorods of CdSe (Figure 2.7) preferentially grow in wurtzite structure, as can be inferred from XRD measurements and high resolution TEM [29].

A higher level of complexity is observed in branched nanocrystals (Figure 2.8). An intriguing example of such structures is the tetrapod. It is composed of four rods that are fused together in a central core. This shape is observed in several materials, such as ZnO [39], ZnSe [40] [41], ZnS [42], CdSe [43] [44] [45], CdTe [46], Pt [47] and Fe_2O_3 [48]. Generally, the growth mode of the tetrapods is driven by the same mechanism as the growth of the rods. During growth monomers are deposited onto the high energy facets of the arms, i.e. on their tips, whereas deposition of monomers onto the lateral facets of the arms is hindered. The main difference in the growth process resides in the nucleation event and the very early stage of the growth, when the core of the tetrapod is formed.

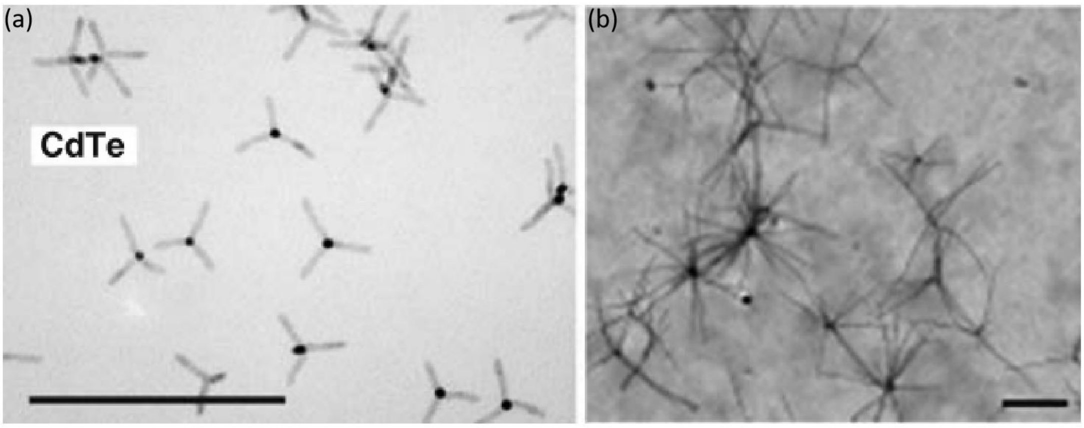

Figure 2.8 TEM images of branched CdTe. (a) The nanocrystals consist of four rods that are fused together in one point so that they span a tetrahedral angle between two legs. In the projection of the TEM, three legs can easily be identified, the forth legs points directly upwards. Due to the longer distance that the electron beam has to travel through the material this leg appears as a dark spot. (b) Hyperbranched particles of CdTe. The scale bars represent 200 nm. Hyper-branched particles reprinted from [49].

2.1.4 Size Control

Talapin et al. [50] performed a numerical simulation of the time evolution of the particle size in an ensemble by using the Monte Carlo method (Figure 2.9). They used Equation (2-1 to 2-5) to calculate the growth rate for an individual particle.

$$\frac{\mathrm{d}r^*}{\mathrm{d}\tau} = \frac{S - \exp(1/r^*)}{r^* + K\exp(\alpha/r^*)} \qquad 2\text{-}1$$

$$r^* = \frac{RT}{2\gamma V_m} r \qquad 2\text{-}2$$

$$\tau = \frac{R^2 T^2 D C^o_{s,eq}}{4\gamma^2 V_m} t \qquad 2\text{-}3$$

$$K = \frac{RT}{2\gamma V_m} \frac{D}{K^0_p} \qquad 2\text{-}4$$

$$r_{zero} = \frac{2\gamma V_m}{RTr^*_{zero}} = \frac{2\gamma V_m}{RT \ln S}$$ 2-5

Here r* is the dimensionless radius, r is the particle radius, τ is the dimensionless time, S is the degree of supersaturation, K is a dimensionless parameter describing the type of the control of the process (the ratio between diffusion and reaction rate constants for a flat interface); α is the transfer coefficient, γ is the surface free energy per unit area, Vm is the molar volume, the coefficient 2γVm/(RT) called "capillary length" is usually of the order of 1 nm. D is the diffusion coefficient, k_p^0 is the rate constant for the bulk crystal (r= ∞) $C^0_{s,eq}$ is the equation image is the equilibrium surface concentration of the bulk crystal (r→∞).

The initial size distributions of the ensembles of particles are set to normal distributions with various relative standard deviations and a mean value of r_0=1 nm. With these given ensembles of particles, simulations of the growth process were started with an initial supersaturation S_0. Figure 2.9 a shows the time evolution of the size distribution of the particle ensemble. The initial reaction solution is highly supersaturated and the growth reaction operates under the diffusion-controlled condition. Two periods in the growth process can be distinguished in this figure. Initially ($0<\tau<10^{-2}$), the mean radius increases rapidly and the size distribution becomes narrower. In this period, the supersaturation is so high that equation image is far below the mean radius 〈r*〉 and consequently, all of the particles are in the "focusing" region. In the second stage ($10^{-2}<\tau$), the growth rate declines sharply and the size distribution broadens. In this period, the supersaturation is low because of the rapid consumption of the monomer during the early period. As a result, the value of equation image becomes comparable to that of 〈r*〉 and many of the particles in the ensemble fall into the "defocusing" region (Figure 2.9 b). Figure 2.9 c depicts the relationship between the mean radius and the relative standard deviation of the size distribution for different initial supersaturations: A high initial supersaturation causes the “focusing” period to be maintained for a large mean radius, resulting in a low relative standard deviation at the end of the “focusing” period. Figure 2.9 c also shows that the “defocusing” period leads to a similar equilibrium relative standard deviation regardless of the initial supersaturation. In the “defocusing” and equilibrium periods in which r_{zero} lies near $\langle r^* \rangle$, Ostwald ripening occurs. In this process, smaller particles dissolve and larger particles grow by receiving the monomers from the dissolving particles (This process was described in the previous section as an explanation for the decrease of the particle concentration during the growth stage). When the Ostwald ripening process is under pseudoequilibrium state, the dissolving rate and reprecipitation rate of the monomers are balanced and the degree of supersaturation declines very slowly. Generally, the Ostwald ripening broadens the standard deviation of the particle size distribution. At the same time, the mean size of the particle ensemble is also increased. As a result, the relative standard deviation (the standard deviation divided by the mean value) converges to a certain value as the reaction system enters the pseudoequilibrium state. According to the simulation results by Talapin et al., the relative standard deviation in the equilibrium period is almost independent of the initial size distribution but is lowered when the surface free energy is high.

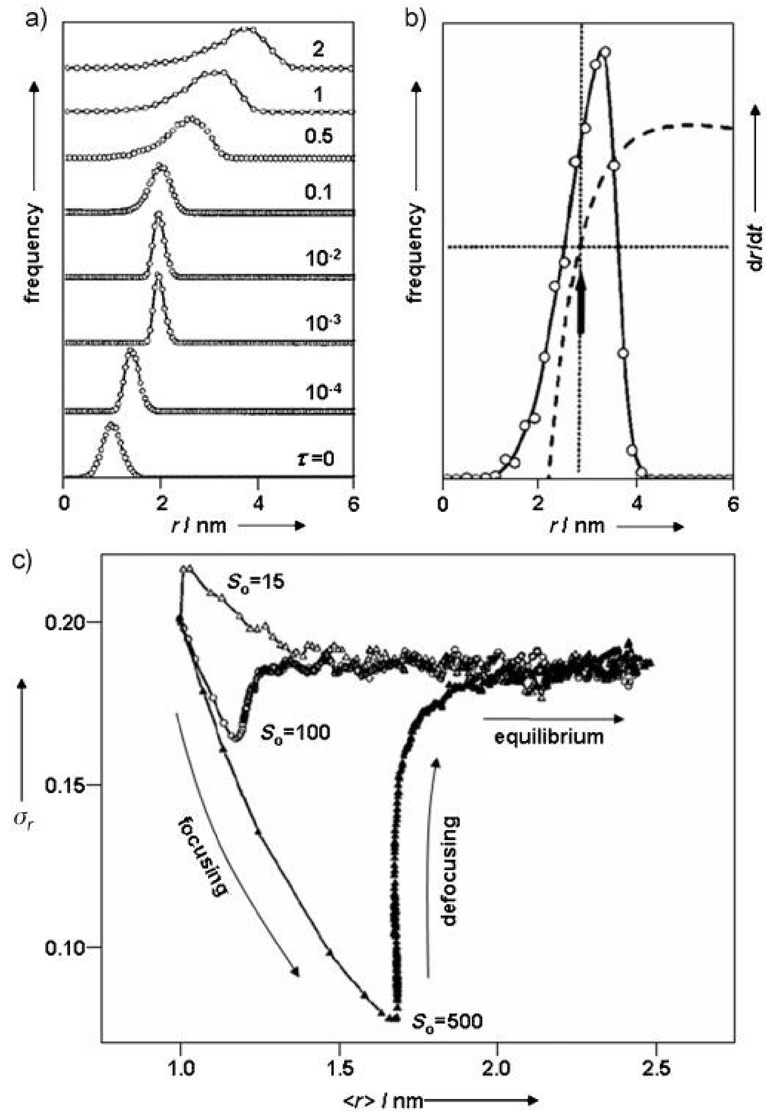

Figuew 2.9 a) Time evolution of the size distribution of the ensemble of particles. b) The size distribution of particles (open circles and solid line) and the growth rate as a function of radius (dashed line) in the later period of the reaction. The arrow indicates the position of r_{zero}. c) Relative standard deviation versus mean radius for different initial levels of supersaturation. The data are excerpted from references [51].

Peng et al. [20] demonstrated the temporal evolution of the size distribution for one CdSe nanocrystal growth experiment as shown in Figures 2.10 and 2.11, left. The size distribution starts out with a standard deviation of 20 %. Over the next 190 min, there are two distinct kinetic regimes: during the first 22 min, the average size increases relatively rapidly (from 2.1 to 3.3 nm diameter), and the size distribution is "focused" from 20 % to 7.7 %. Subsequently, the nanocrystals grow more slowly (from 3.3 nm to 3.9), and the nanocrystal size distribution broadens to 10.6%. A second injection of molecular precursors increases the growth rate and refocuses the size distribution to 8.7%. Particle yield data revealed that the number of particles keeps constant during "focusing" and "refocusing" and decreases during "defocusing". The monomer concentration, determined by particle yield, exhibits a dramatic drop during focusing and refocusing and keeps approximately constant during the defocusing. Similar growth kinetics are observed for InAs (Figure 2.11, right) . The nanocrystal yield from the reaction is high, and the resulting particles are faceted.

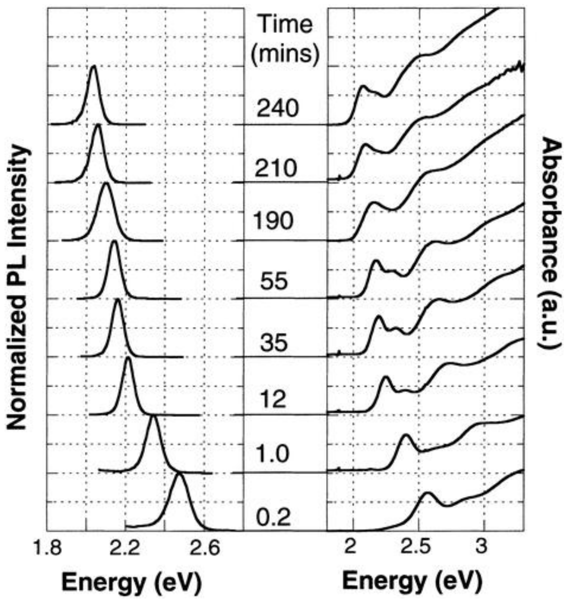

Figure 2.10 Room-temperature PL and absorption spectra from the sample of CdSe nanocrystals. Note that a secondary injection of monomer occurs at 190 min [20] .

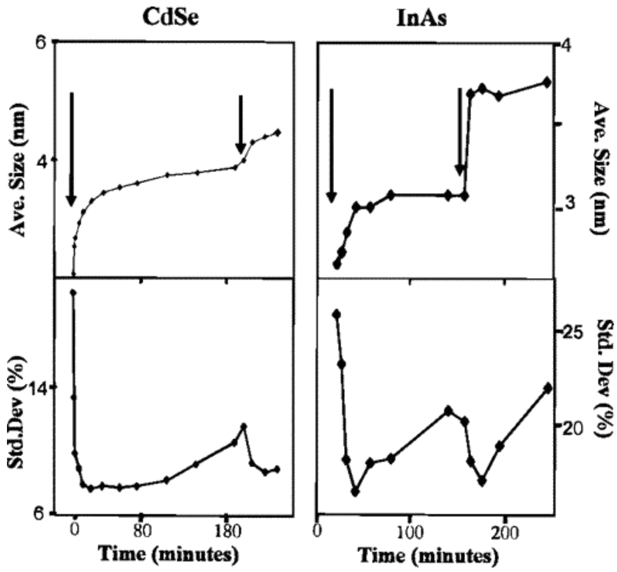

Figure 2.11 Left: The mean size and the size distribution extracted from the data in Figure 2.10. Right: The same data extracted from the PL for a synthesis of InAs. Arrows indicate injections [20].

2.1.5 Precursors

It is the ambition of many nanochemists to achieve a level of mechanistic understanding that enables the retro-synthesis of particular nanocrystal shapes, compositions, sizes, and heterostructures. Precursors are molecules or metal complexes that contain the individual elements of the final nanocrystal in a different form. Therefore, the first step in colloidal synthesis is usually the conversion of the precursors into the intended product. Given its importance, precursor conversion has been studied in many nanocrystal systems: metals [52] [53] [54], metal sulfides and selenides [17] [55] [56] [57], metal oxides [58] [59] [60], lead halides [61], and metal pnictides [62] [63] [64]. In such efforts, nanochemists aim to write down the complete and balanced chemical equation, after determining the correct stoichiometry of the reaction and identifying reaction by-products. Ideally, this is complemented with a rigorous kinetics study to obtain further details about the mechanism. Mechanistic insight is very useful to develop new syntheses and to optimize existing ones.

The synthesis of group II−VI colloidal nanocrystals by thermal decomposition of organometallic precursors has been extensively used in the past decades. This synthetic approach was first reported for the synthesis of cadmium chalcogenide quantum dots [12], nanorods [29], and tetrapods [46] in tri-n-octylphosphine oxide (TOPO) using $CdMe_2$ and tri-n-octylphosphine selenide (TOPSe) as precursors. Later, a more synthetically convenient precursor, CdO [65], was introduced to replace $CdMe_2$, and noncoordinating solvents, such as octadecene (ODE), were used to replace TOPO [66]. Besides its application in the syntheses of quantum dots, rods, and tetrapods of cadmium chalcogenides, this thermal decomposition method has also been extended to the synthesis of ZnS and ZnSe nanocrystals [67] as well as core−shell dots and rods [68] [69] branched rods and tetrapods [70] [49], and quantum dot−quantum well structures [71] [72].

Experiments suggested that trialkylphosphine chalcogenides deoxygenate the alkylphosphonate or alkylcarboxylate surfactants, liberating the chalcogen atom. A mechanism is proposed where nucleophiles such as alkylphosphonate and alkylcarboxylate attack a Lewis acid activated (TOPE)M (E = S, Se, Te; M = Zn, Cd) complex, breaking the PE double bond [55]. Table 2.1 shows Precursors, stabilizers and solvents used in the synthesis of various II–VI semiconductor NCs.

Table 2.1 Precursors, stabilizers and solvents used in the synthesis of various II–VI semiconductor NCs [73]

Material	Precursors and stabilizers	Solvent(s)	Method[a]
CdS, CdSe, CdTe	$CdMe_2$/TOP, $(TMS)_2Se$ or $(TMS)_2S$ or $(BDMS)_2Te$	TOPO	HI
CdSe	$CdMe_2$/TOP, TOP-Se	TOPO, HDA	HI
CdSe, CdTe	CdO, TDPA, TOP-Se or TOP-Te	TOPO	HI
CdSe	CdO or $Cd(ac)_2$ or $CdCO_3$, TOP-Se, TDPA or SA or LA	TOPO	HI
CdS, CdSe	CdO, S/ODE or TBP-Se/ODE, OA	ODE	HI
CdSe	$Cd(st)_2$, TOP-Se, HH or BP	HDA, octadecane	HI
CdSe	$Cd(my)_2$, Se, OA/ODE	ODE	HU
CdSe	CdO, Se/ODE, OA	ODE	HI
CdSe	CdO, Se, OA	Olive oil	HI
CdSe	$Cd(st)_2$, TBP-Se, SA, DDA	ODE	HI
CdS	$Cd(ac)_2$, S, MA	ODE	HU
CdS, ZnS	$Cd(hdx)_2$ or $Cd(ex)_2$ or $Cd(dx)_2$ or $Zn(hdx)_2$	HDA	HU
CdS, ZnS	$CdCl_2$/OAm or $ZnCl_2$/OAm/TOPO, S/OAm	OAm	HU
CdTe	$CdMe_2$, TOP-Te	DDA	HI
CdTe	CdO, TBP-Te/ODE or TOP-Te/ODE, OA	ODE	HI
CdTe	CdO, TBP-Te, ODPA	ODE	HU
ZnS	$Zn(st)_2$, S/ODE	ODE, Tetracosane	HI
ZnS	$ZnEt_2$, S	HDA/ODE	HU
ZnSe	$ZnEt_2$, TOP-Se	HDA	HI
ZnSe	$Zn(st)_2$, TOP-Se	Octadecane	HI
ZnTe	Te and $ZnEt_2$ in TOP	ODA, ODE	HI
HgTe	$HgBr_2$, TOP-Te	TOPO	HI
$Cd_{1-x}Zn_xSe$	$ZnEt_2$/TOP, $CdMe_2$/TOP	TOPO, HDA	HI
$Cd_{1-x}Zn_xSe$	$Zn(st)_2$, $Cd(st)_2$, TOP-Se	ODE	HI
$Cd_{1-x}Zn_xS$	CdO, ZnO, S/ODE, OA	ODE	HI
$CdSe_{1-x}Te_x$	CdO, TOP-Se, TOP-Te	TOPO, HDA	HI

2.1.6 Ligands

The surface ligands used in the high-temperature synthesis of high-quality nanocrystals are usually quite bulky, with a small anchoring group for bonding onto the surface of nanocrystals and a long/large hydrocarbon chain . Without a rapid dynamics of these bulky surface ligands [74], it would be difficult to understand the coexistence of a decent growth rate and the well-passivated surface of the resulting high-quality nanocrystals. It is also known that ligands with strong anchoring group(s) to the surface atoms of nanocrystals are often not good choices for synthesizing the nanocrystals [75]. This fact is again consistent with the dynamic bonding of the surface ligands. This is so because ligands with strong anchoring groups would not allow them to be dynamic through a medium-level thermal excitation in the temperature range between roughly 250 and 350 °C.

The results suggest that the surface ligand dynamics is not only a function of the reaction temperature but also strongly depends on the interligand interactions. For fatty amine ligands bonded onto the surface of CdSe nanocrystals under elevated temperatures, the boiling/melting points of the free ligands provide reasonable reference points to manipulate the surface ligand dynamics. The active surface ligand dynamics was found to play a critical role for determining the size, size distribution, growth rate, and even Ostwald ripening of a synthetic system. The results further indicate that, without sacrificing the quality of the nanocrystals, the growth temperature of high-quality CdSe nanocrystals can be significantly reduced (~ 150 °C) than what are considered as today's standards (about 250−350 °C) [74].

2.1.6.1 Decomposition of TOPO

During the synthesis of nanocrystals at 300-360 °C, the ligand/solvent tri-n-octylphosphine oxide (TOPO) oxidizes to di-n-octylphosphinic acid and n-octylphosphonic acid [76]. The octylphosphonic acid dehydrates and forms an anhydride. Although the oxidation only proceeds to a small extent (probably consuming adventitious oxygen), the formed decomposition products have a much higher affinity for the metal oxide nanocrystal surface than TOPO itself. Thus, the nanocrystal surface adsorbs the decomposition products and the surface becomes highly complex with three different species present; see Figure 2.12. 1-Octene is a by-product of the oxidation and is observed refluxing in the reaction setup [77].

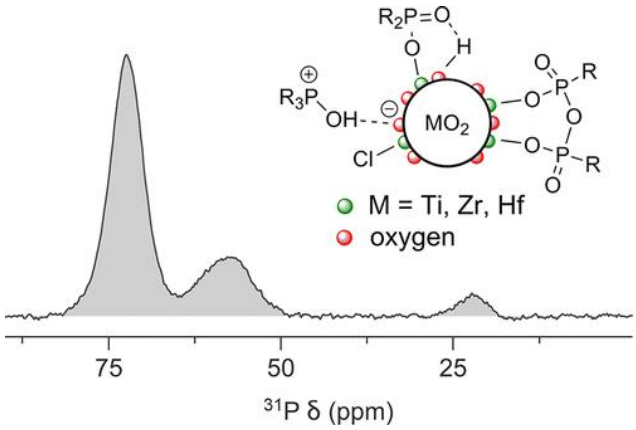

Figure 2.12 Titanium, zirconium, and hafnium oxide nanocrystals synthesized in TOPO are capped with TOPO and its decomposition products, resulting in a complex ligand shell. The three species are present in the phosphorus NMR spectrum [76].

2.1.6.2 Oxidation of Oleylamine to Oleic Acid

The oleylamine is oxidized to aldimine by nitrate in the synthesis. The reaction does not stop there but can proceed all the way to carboxylic acid [78]. For example, the synthesis of CeO_2 nanocrystals, from cerium nitrate and oleylamine. The metal nitrate first forms a complex with oleylamine, which subsequently decomposes, producing a myriad of by-products; The primary aldimine is hydrolyzed by adventitious water to aldehyde, which is further oxidized to carboxylic acid (presumably by nitrate or one of the nitrous decomposition products). Since carboxylates have a higher binding affinity to oxide surfaces than oleylamine, the final particles were capped with carboxylate and not with oleylamine [78].

2.1.6.3 Oligomerization of Phosphonic Acid

Phosphonic acids are often used for colloidal syntheses above 300 °C, because metal carboxylates decompose at these temperatures [79]. Phosphonic acids do not decompose but still dehydrate to form phosphonic acid anhydride; see Scheme in Figure 2.13 [80]. The reaction can proceed with the second acidic group, producing phosphonic acid anhydride oligomers. In the presence of this oligomer, CdSe nanocrystals can aggregate or form a gel [81].

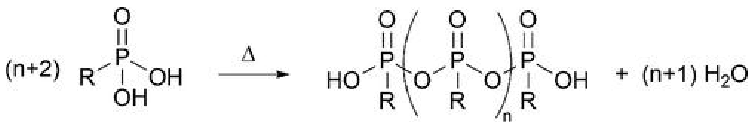

Figure 2.13 Formal Dehydration of Phosphonic Acids. In practice, often a dehydration agent is also present in the reaction mixture [80].

Impurities in reagents can exhibit side reactions, inhibit or accelerate nanocrystal growth, or steer anisotropic growth. For example, (di)alkylphosphinic acid and alkylphosphonic acid impurities in TOPO were shown to change the shape of the CdSe nanocrystals. The concentration of these impurities showed a large bath-to-batch variation. To achieve reproducible results, it is recommended to recrystallize TOPO before use [82] [83]. The nanochemist can subsequently add a controlled amount of co-surfactant to the reaction. As a second example, oleylamine contains several impurities that reduce its capacity to dissolve salts [84]. Purification as a salt and subsequent vacuum distillation is recommended. Furthermore, the use of technical oleylamine, with a varying blend of cis, trans, and saturated chains, creates irreproducibility in the ligand shell structure, with implications on nanocrystal assembly, and its use is not recommended for certain applications [85]. Oleylamine and TOPO received quite some attention because they are commonly used ligands. However, there can be impurities in every reagent that is used, including metal precursors and other organic molecules [56]. Techniques such as vacuum distillation and recrystallization should thus be part of the nanochemist's skill set. It is good chemical practice to perform some type of check of the reagents before use. For organic molecules one can easily take a 1H NMR (and 31P NMR) measurement before use.

2.2 Structural Properties of NCs

Most binary octet semiconductors crystallize either in the cubic zinc blende (ZB) or in the hexagonal wurtzite (W) structure, both of which are four-coordinate and vary in the layer stacking along (111), showing an ABCABC or an ABAB sequence, respectively (Figure 2.14). The room temperature ground state structures of selected II–VI, III–V and IV–VI semiconductors are given in Table 2.2. In cases of relatively low difference in the total energy between the ZB and the W structure (e.g. CdTe, ZnSe), the materials exhibit the so-called W–ZB polytypism [86]. Depending on the experimental conditions, nucleation and growth of the NCs can take place in either structure and also the coexistence of both structures in the same nanoparticle is possible. Lead chalcogenide NCs crystallize in the six-coordinate rocksalt structure, and it has been shown that also CdSe NCs can exist in this crystal structure at ambient pressure, provided that their diameter exceeds a threshold size of 11 nm, below which they transform back to the four-coordinate structure [87].

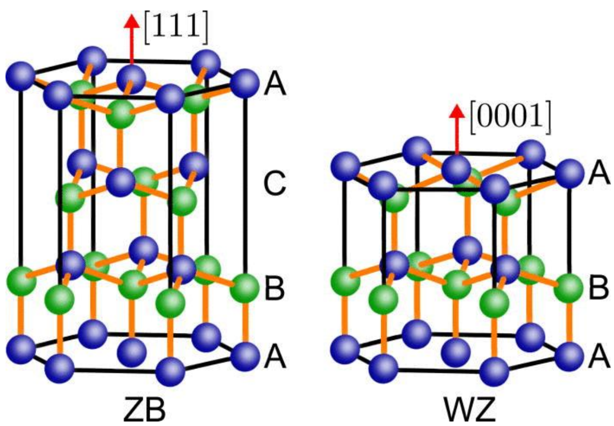

Figure 2.14 ZB (left) and WZ (right) structures and their stacking sequence. The ZB is presented in the [111] direction. In this direction, the unit cell is twice as large as the usual ZB unit cell. The WZ is presented in the [0001] direction. The arrows (red lines) are the growth directions in NWs [88].

Table 2.2 Structural parameters of selected bulk semiconductors [89] [90]

Material	Structure (300 K)	Type	E_{gap} (eV)	Lattice parameter (Å)	Density (kg/m^3)
ZnS	Zinc blende	II–VI	3.61	5.41	4090
ZnSe	Zinc blende	II–VI	2.69	5.668	5266
ZnTe	Zinc blende	II–VI	2.39	6.104	5636
CdS	Wurtzite	II–VI	2.49	4.136/6.714	4820
CdSe	Wurtzite	II–VI	1.74	4.3/7.01	5810
CdTe	Zinc blende	II–VI	1.43	6.482	5870
GaN	Wurtzite	III–V	3.44	3.188/5.185	6095
GaP	Zinc blende	III–V	2.27 i[a]	5.45	4138
GaAs	Zinc blende	III–V	1.42	5.653	5318
GaSb	Zinc blende	III–V	0.75	6.096	5614
InN	Wurtzite	III–V	0.8	3.545/5.703	6810
InP	Zinc blende	III–V	1.35	5.869	4787
InAs	Zinc blende	III–V	0.35	6.058	5667
InSb	Zinc blende	III–V	0.23	6.479	5774
PbS	Rocksalt	IV–VI	0.41	5.936	7597
PbSe	Rocksalt	IV–VI	0.28	6.117	8260
PbTe	Rocksalt	IV–VI	0.31	6.462	8219

2.2.1 Core/Shell Structure

In the case of semiconductor NCs, the concept of combining different materials in a single nanoparticle has been mainly studied in the context of core/shell NCs, in which the shell material has a considerably wider gap than the material of the core [91] [92] [93]. In this approach, the electron and hole experience a confinement potential that tends to localize both of the carriers in the NC core (Type-I localization), which reduces their interactions with surface trap states and improves the NC emission quantum yields. Core/shell NCs can also provide “spatially indirect” states, in which electrons and holes are spatially separated between the core and the shell (Type-II localization) [94] [95] [96].

Figure 2.15 gives an overview of the band alignment of the bulk materials, which are mostly used in NC synthesis. Two main cases can be distinguished, denominated type I and type II band alignment, respectively. In the former, the band gap of the shell material is larger than that of the core one, and both electrons and holes are confined in the core. In the latter, either the valence band edge or the conduction band edge of the shell material is located in the band gap of the core. The resulting staggered band alignment leads upon excitation of the NC to a spatial separation of the hole and the electron in different regions of the core/shell structure.

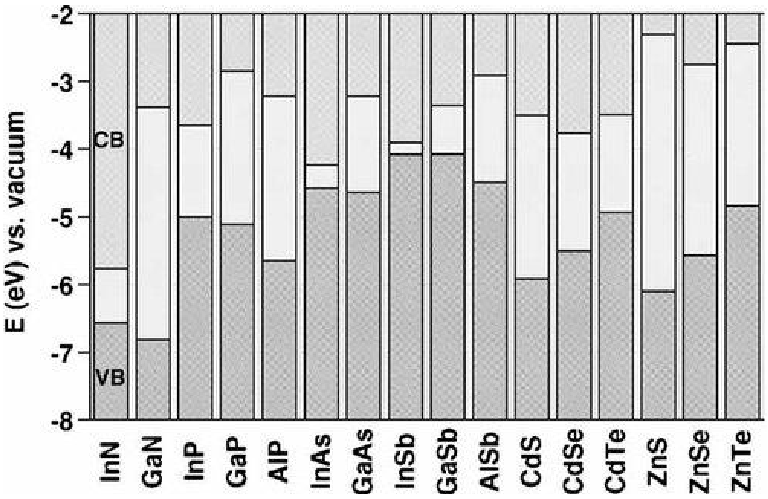

Figure 2.15 Electronic energy levels of selected III–V and II–VI semiconductors using the valence-band offsets (VB: valence band, CB: conduction band) [97].

2.2.2 CdX(X=Se, S, Te, ZnSe, Zn S) Alloy

2.2.2.1 Binary Alloy System

The hot-injection technique for the synthesis of monodisperse CdSe, CdS, CdTe NCs via experienced a number of modifications since 1993 reported [12]. The latter can be classified into two groups, the first one aiming at the further improvement of the particles size and shape control, and the second one at the simplification of the experimental protocol. The addition of HDA to the TOPO/trioctylphosphine (TOP) mixed solvent [98] can led to an unprecedented low size distribution of the as-prepared CdSe NCs of the order of 5%. Later, the replacement of the pyrophoric Cd precursor dimethylcadmium by much easier to handle compounds such as cadmium oxide, cadmium acetate or cadmium nitrate and the substitution of the coordinating solvent TOPO by the non-coordinating one 1-octadecene (ODE) was proposed [99] [65] [66]. The ODE offers a number of practical advantages (liquid at room temperature, lower price and more environmentally benign than TOPO).

Moreover, the use of ODE allows for a better fine-tuning of the reactivity of the Cd precursor, as the solvent does not have the additional function of being the stabilizing ligand. It has been demonstrated that the mean size and size dispersion depend on the length of the carbonaceous chain.

Another example for the binary NCs is ZnSe, which was reported in 2004 [100]. pyrophoric diethylzinc was replaced by an air-stable and easy to manipulate precursor (zinc stearate), while keeping the established Se precursor (TOPSe) and using the saturated non-coordinating solvent octadecane. In the growth process zinc stearate served not only as the cation precursor but also as a source of stabilizing stearate ligands. The size of the obtained ZnSe could be varied from 3 to 7 nm by adjusting the concentration of the zinc precursor in the reaction mixture and/or varying the temperature, yielding samples emitting in the range of 390-440 nm (FWHM 12-17 nm).

2.2.2.2 Ternary Alloy System

As aforementioned, by taking advantage of the quantum confinement effect it is possible to tune, through size control, the fluorescence wavelength of semiconductor NCs. The formation of a ternary structure is an alternative way to influence the band gap of the NCs, not by changing their size but their composition. Although the term alloy is, in its strict sense, limited to solid solutions of two or more metals, it is also widely applied in literature for the description of ternary systems comprising chalcogenide ions. A typical example is $Cd_{1-x}Zn_xSe$, corresponding to ZnSe NCs, in which a fraction of the Zn atoms is substituted by Cd ones in the crystal lattice. The band gap of the resulting ternary alloy is in between those of pure ZnSe and of pure CdSe NCs of the same size. In contrast to the crystal lattice parameters, which show, according to Vegard's law, a linear evolution with composition, the curve describing the corresponding evolution of the band gap shows a deviation from linear behavior.

However, this difference is not very pronounced for common anion systems such as $Cd_{1-x}Zn_xSe$ or $Cd_{1-x}Zn_xS$ [101] [102].

2.2.2.3 Doped Nanocrystals

Doping – the introduction of a small amount of impurities into the crystal lattice – is an attractive way to change the NCs physical properties. An important example is the doping of II–VI semiconductors with paramagnetic Mn^{2+} ions (S ¼ 5/2), yielding materials denominated dilute magnetic semiconductors (DMS), which exhibit interesting magnetic and magneto-optical properties [103]. At the same time, the host NC can act as an antenna for the absorption of energy (e.g. light) and excitation of the dopant ions via energy transfer. In this case, mostly UV-absorbing NCs are chosen as the hosts, such as ZnS or ZnSe. Mn-doped ZnSe is an instructive example for the development of doped II–VI semiconductor NCs. Bulk ZnSe:Mn exhibits PL at 582 nm (2.13 eV), commonly assigned to an optically forbidden d–d transition of Mn^{2+} ($^4T_1$ to $^6A_1$) [104] [105].

A general problem encountered in essentially all attempts of NCs doping is the fact that the host matrix tends to expel the dopant ions to the surface, in some sort of selfpurification process. Therefore, even in the favourable case of dopant ions, having the same valence state and similar ionic radius as the corresponding host ions, successful (volume) doping is difficult to achieve in a straightforward approach by simply adding a small amount of dopant precursor during the synthesis of the host NCs.

2.3 Nanorods

Nanorods are of great interest for both fundamental research and technical applications due to several unique electrical and optical properties, such as linearly polarized emission [106] [107], exciton storage [108], electroluminescence [108], and efficient 1D electrical transport [109] [110], which are determined by their anisotropic shape. In particular, core−shell nanorods fabricated by the seeded growth approach have several advantageous properties for optoelectronic applications [111]. Due to their core−shell structure, such rods are highly luminescent and their emission wavelength can be tuned within certain limits not only by the shape of the rod but also even more efficiently by the size of the core. Moreover, the seeded growth approach yields a narrow distribution in nanorod length and diameter, which greatly facilitates their oriented assembly [112], and ordered nanorod assemblies over micrometer length scales have been reported by microfluidic [113] and electric field-assisted assembly approaches [114]. In order to obtain nanorod assemblies with a controlled orientation with respect to an external electric field, the electrodes can be fabricated prior to the nanorod deposition on a variety of substrates [115]. Such devices with ordered assemblies of nanorods should exhibit novel properties and improved current transport compared to spherical nanocrystal arrays [116] . Of particular interest for photoelectrical applications is the effect of the polarization of the incident light, as well as the impact of the applied electric field on exciton ionization, the charge transport through the inter-rod barrier [117], the carrier trapping and band-to-band recombination processes. All of these processes should depend strongly on the nanorod orientation [118].

For example, control over the long-range orientational order of the liquid crystal (LC) is critical for obtaining superior optical switching and display-device performance [119]. The ultrasmall nanorods possess a strong inherent dipole moment, and show excellent miscibility in the LC host, forming well-organized locally aligned arrays. This localordering affects significantly the global ordering of the blend, allowing a more rapid response of the electro-optic properties. Importantly, the blend shows tunable polarizations from vertical to grazing view angles, with a significant adjustable an isotropy for improvement of contrast ratios and viewing angles of LC displays. The perpendicular polarization axis persists in an orthogonal state relative to the axis of orientation of the rods and blend. An external field can affect the orientational order of the blend within which the orthogonal state of polarization persists, allowing the electro optic properties to be tailored between vertical and grazing view angles. The strong inherent dipole moment of the rods modulates the faster operating voltage fulfilling commercial requirements [120] [121].

The CdSe/CdS semiconductor nanorods is the typical one which are fabricated with a seeded type growth approach getting narrow distributions of rod lengths and diameters, as shown in Figure 2.16. These materials present very appealing optical characteristics [79] and similar materials were already employed in order to study enhanced orientational photorefractive effects generated in doped nematic liquid crystals [122].

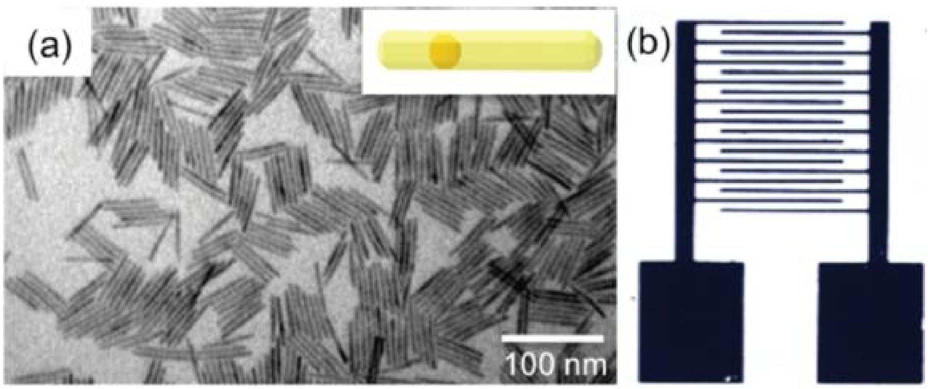

Figure 2.16 (a) Transmission electron microscope image of core-shell CdSe/CdS nanorods with 60 nm length and 4.5 nm diameter deposited on a carbon-coated grid. The inset illustrates the core−shell structure that resulted from the seeded growth approach. (b) Optical microscope image of an interdigitated electrode structure fabricated on a glass substrate [121].

2.4 Electrophoretic Deposition (EPD)

2.4.1 Source of Dipole Moment

The dipole moment is important for understanding the mechanism of alignment of anisotropic nanoparticles under an external field. The source of a permanent dipole in nanocrystals comes from four aspects: (1) internal bonding geometry; (2) shape asymmetry; (3) surface strain; (4) surface localized charges [123]. It is ensured that the permanent dipole moment of wurtzite crystals is a consequence of the intrinsic polar character of the asymmetric crystal lattice [124]. The location distribution in a point-charge model of metal cations from group IIB and chalcogenide ions from group VIA can be clearly seen in Figure 2.17a. Moreover, because the overall dipole originated from the summation of the contribution of each monolayer, the shape and size of the nanocrystals also show a significant impact on the scaling of the permanent dipole. Figure 2.17b and c demonstrates that the addition of each monolayer to differently shaped crystals may lead to the values of dipoles showing linear or quadratic dependence on dimensions and the change of the direction of the dipole as well. Both wurtzite CdSe nanocrystals and zinc blende ZnSe nanocrystals demonstrate a size-dependent permanent dipole theoretically and experimentally [125].

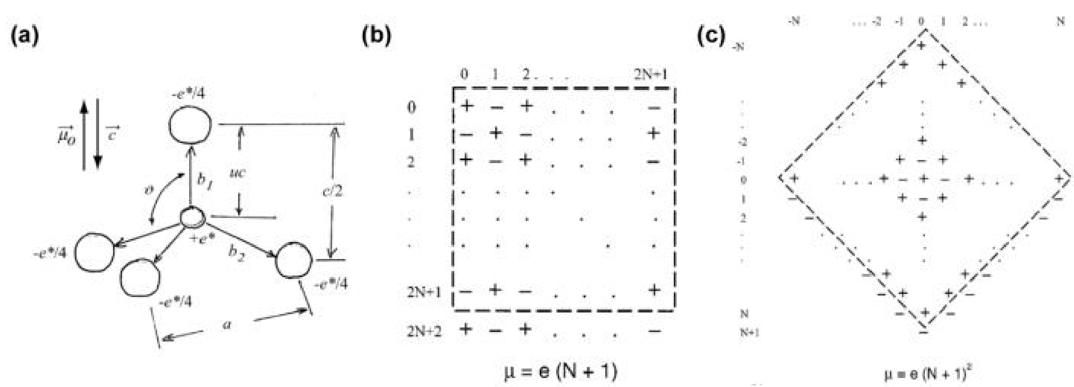

Figure 2.17 (a) Point-charge model for explaining the occurrence of a permanent electric dipole moment and spontaneous electric polarization in typical wurtzite structure [126]; (b) a simple 2D

ionic square lattice emphasizing neutral facets and (c) polar faces lead to a linear and quadratic dependence of the dipole [125].

The existence of the permanent dipole moment of wurtzite nanorods can be characterized by transient electric birefringence. One can attain the calculated dipole moment from the movement and rotation of elongated particles in response to an applied field, while the effects of solvent and particle interaction are considered necessarily during measurement. Table 2.3 gives the dipole moment of a few types of wurtzite semiconductor nanocrystals from both experiment and simulation.

Table 2.3 Dipole moment of some wurtzite nanocrystals.92

D (nm)	L (nm)	L/D	material	μ (D)
3.0−6.5	7.5−40	2−12	CdSe	29−971
3.0−3.7	18−60	6−20	CdSe	69−354
3−5	10−40	2−10	CdSe−CdS	77−863
3−5	4−50	1−10	CdS	76−2650
5	30	6	CdS	1590
8	40	5	CdSe	1105
3.4/6	38/50	11.1/8.4	CdSe/CdTe	189/−
5.2	24	4.6	CdSe−CdS	560
10	25	2.5	CdS	5300
5	15	3	CdS	795

2.4.2 EPD

EPD is a widely used in industry, including fuel cells, lithium batteries and other functional coatings. The dispersed charged particles in a liquid medium are deposited on one side of the electrode with the opposite charge in an external electric field. The principal driving force of deposition is the charge on the particles and electrophoretic mobility. Based on this mechanism, the factors influencing the process are from two parts: 1) those related to the suspension, such as concentration, surface charge, morphology of particles, dielectric constant and viscosity of the dispersing medium; 2) the factors related to the process, such as the surface chemistry of the substrate, voltage and time. Compared with other coating techniques, EPD is a very versatile method with advantages of short processing time, low-cost setup, few restrictions on the choices of the substrate and deposited materials and easy control of the thickness and morphology of the deposited films. There are some key parameters for the EPD. In a real system, an overly large dielectric constant for the solvent will cause aggregation of nanocrystals and also reduce the size of the double layer region and the electrophoresis mobility [127]. Table 2.4 lists the physical constants of a few polar and nonpolar solvents used generally.

Table 2.4 Physical parameters of some solvents [127].

	Viscosity (mP·s)	Relative dielectric constant[a]	Dipole moment (Debye)[b]	Vapor pressure (kPa)[c]
Methanol	0.544	32.7	2.87	12.8
Isopropanol	2.038	17.9	1.66	4.4
Water	0.89	80.1	1.8546	1.75
Toluene	0.560	2.38	0.375	2.9
Hexane	0.3	1.88	0.08	160
Cyclohexane	0.894	2.02	0	10.4
Chlorobenzene	0.753	5.62	1.69	1.2

It has been demonstrated that particles' size has an effect on the morphology of the resulting deposit: fewer cracks are observed from the EPD of smaller particles [128]. As a reflection of surface charge, the zeta potential is a key factor in EPD. It can affect the deposition rate, the direction of deposition, and the stability of the suspension. the deposit grows with the increases of the applied field. This voltage threshold is determined by the intrinsic dipole and shape of the nanorods. Once above this threshold, the thickness of the film increases. In a typical EPD process, it has been found that the deposition rate decreases under a fixed field as the time elapses

[129]. The uniformity and conductivity of the substrate are also critical for the preparation of a high-quality EPD film.

Table 2.5 gives a few commonly used ligands and their performance in electron conductivity. To increase the carrier transportation, those long-chain ligands could be replaced by shortchain ligands, which can benefit carrier transportation, or by exchanging with another particular type of molecule having bifunctional head groups (1,6-hexanedithiol, hydrazine, etc.). The typical ligand-exchange procedure is to immerse the nanocrystals'assembled films containing ligand A into a solution of ligand B, but the shortcoming of this method is that only ligands A that are on the surface will be partially replaced.

Table 2.5 Different types of surface ligands used in nanocrystals and nanocrystal Solids [130].

Ligand type	Molecular structure	Interparticle spacing	Functions, characteristics, typical examples
Molecules with single head group and a long hydrocarbon chain	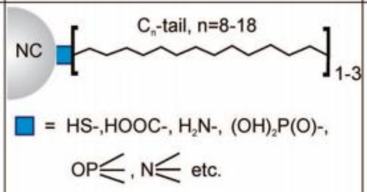	>1.5 nm	• Most common ligands used for NC synthesis • Form stable colloidal solutions • Hydrophobic surface • Form highly insulating NC solids, $\sigma \sim 10^{-12}$-10^{-9} S cm^{-1}
Short-chain molecules with single head group	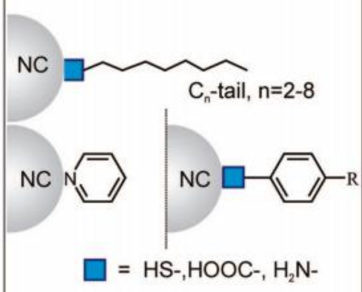	0.3-1 nm	• Treatment of NC solids or ligand-exchange in solutions • Decreased colloidal stability • Improved electronic transport compared to long-chain ligands • Reported detectivity of $\sim 10^{12}$-10^{13} Jones in photodetectors on PbS NCs caped with butylamine[270] • Conductivities of up to 10^{-1} S cm^{-1} in arrays of metallic NCs[267]
Cross-linking molecules with two end groups	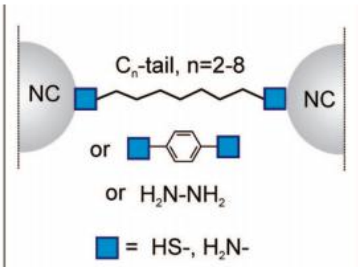	0.3-1 nm	• Mainly prepared by treating NC solids • μ up to 2 cm^2 V^{-1} s^{-1} in arrays of PbSe NCs treated with N_2H_4[23] • $\mu \sim 10^{-2}$ cm^2 V^{-1} s^{-1} in arrays of CdSe NCs treated with 1,4-phenylenediame[185] • Solar cells based on PbS and PbSe NC solids showed power conversion efficiencies of up to 2.1%[253,271,272]
Metal chalcogenide complexes	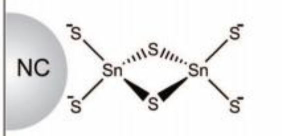	≥ 0.5 nm	• Prepared via solution phase ligand-exchange • Complete removal of original organic ligands • Hydrophilic surface • High conductivities of ~200 S cm^{-1} in Au-$Sn_2S_6^{4-}$NC solids[273]

Reference

1. Alivisatos, A.P., *Nanocrystals: building blocks for modern materials design.* Endeavour, 1997. **21**(2): p. 56-60.
2. El-Sayed, M.A., *Small is different: shape-, size-, and composition-dependent properties of some colloidal semiconductor nanocrystals.* Accounts of chemical research, 2004. **37**(5): p. 326-333.
3. Yin, Y. and A.P. Alivisatos, *Colloidal nanocrystal synthesis and the organic–inorganic interface.* Nature, 2005. **437**(7059): p. 664-670.
4. Steigerwald, M.L. and L.E. Brus, *Semiconductor crystallites: a class of large molecules.* Accounts of Chemical Research, 1990. **23**(6): p. 183-188.
5. Kazes, M., et al., *Lasing from semiconductor quantum rods in a cylindrical microcavity.* Advanced Materials, 2002. **14**(4): p. 317-321.
6. Cushing, B.L., V.L. Kolesnichenko, and C.J. O'connor, *Recent advances in the liquid-phase syntheses of inorganic nanoparticles.* Chemical reviews, 2004. **104**(9): p. 3893-3946.
7. Pileni, M.-P., *The role of soft colloidal templates in controlling the size and shape of inorganic nanocrystals.* Nature materials, 2003. **2**(3): p. 145-150.
8. Alivisatos, A.P., *Perspectives on the physical chemistry of semiconductor nanocrystals.* The Journal of Physical Chemistry, 1996. **100**(31): p. 13226-13239.
9. Smyder, J.A. and T.D. Krauss, *Coming attractions for semiconductor quantum dots.* Materials Today, 2011. **14**(9): p. 382-387.
10. Steigerwald, M.L. and L.E. Brus, *Synthesis, stabilization, and electronic structure of quantum semiconductor nanoclusters.* Annual Review of Materials Science, 1989. **19**(1): p. 471-495.
11. Sowers, K.L., B. Swartz, and T.D. Krauss, *Chemical mechanisms of semiconductor nanocrystal synthesis.* Chemistry of Materials, 2013. **25**(8): p. 1351-1362.

12. Murray, C., D.J. Norris, and M.G. Bawendi, *Synthesis and characterization of nearly monodisperse CdE (E= sulfur, selenium, tellurium) semiconductor nanocrystallites.* Journal of the American Chemical Society, 1993. **115**(19): p. 8706-8715.
13. Park, J., et al., *Synthesis of monodisperse spherical nanocrystals.* Angewandte Chemie International Edition, 2007. **46**(25): p. 4630-4660.
14. Xia, Y., et al., *Shape-controlled synthesis of metal nanocrystals: simple chemistry meets complex physics?* Angewandte Chemie International Edition, 2009. **48**(1): p. 60-103.
15. Buonsanti, R. and D.J. Milliron, *Chemistry of doped colloidal nanocrystals.* Chemistry of Materials, 2013. **25**(8): p. 1305-1317.
16. Buck, M.R. and R.E. Schaak, *Emerging strategies for the total synthesis of inorganic nanostructures.* Angewandte Chemie International Edition, 2013. **52**(24): p. 6154-6178.
17. Garcia-Rodriguez, R., et al., *Conversion reactions of cadmium chalcogenide nanocrystal precursors.* Chemistry of Materials, 2013. **25**(8): p. 1233-1249.
18. De Roo, J., *Chemical Considerations for Colloidal Nanocrystal Synthesis.* Chemistry of Materials, 2022. **34**(13): p. 5766-5779.
19. LaMer, V.K. and R.H. Dinegar, *Theory, production and mechanism of formation of monodispersed hydrosols.* Journal of the american chemical society, 1950. **72**(11): p. 4847-4854.
20. Peng, X., J. Wickham, and A. Alivisatos, *Kinetics of II-VI and III-V colloidal semiconductor nanocrystal growth:"focusing" of size distributions.* Journal of the American Chemical Society, 1998. **120**(21): p. 5343-5344.
21. Talapin, D.V., et al., *A novel organometallic synthesis of highly luminescent CdTe nanocrystals.* The Journal of Physical Chemistry B, 2001. **105**(12): p. 2260-2263.
22. Shah, P.S., et al., *Size-selective dispersion of dodecanethiol-coated nanocrystals in liquid and supercritical ethane by density tuning.* The Journal of Physical Chemistry B, 2002. **106**(10): p. 2545-2551.

23. Cho, K.-S., et al., *Designing PbSe nanowires and nanorings through oriented attachment of nanoparticles.* Journal of the American Chemical Society, 2005. **127**(19): p. 7140-7147.

24. Sun, Y. and Y. Xia, *Shape-controlled synthesis of gold and silver nanoparticles.* science, 2002. **298**(5601): p. 2176-2179.

25. An, K., et al., *Synthesis, characterization, and self-assembly of pencil-shaped CoO nanorods.* Journal of the American Chemical Society, 2006. **128**(30): p. 9753-9760.

26. Kleber, W., et al., *Einführung in die Kristallographie*, in *Einführung in die Kristallographie*. 2010, Oldenbourg Wissenschaftsverlag.

27. Trentler, T.J., et al., *Solution-liquid-solid growth of crystalline III-V semiconductors: an analogy to vapor-liquid-solid growth.* Science, 1995. **270**(5243): p. 1791-1794.

28. Heath, J.R., *A liquid-solution-phase synthesis of crystalline silicon.* Science, 1992. **258**(5085): p. 1131-1133.

29. Peng, X., et al., *Shape control of CdSe nanocrystals.* Nature, 2000. **404**(6773): p. 59-61.

30. Bruchez Jr, M., et al., *Semiconductor nanocrystals as fluorescent biological labels.* science, 1998. **281**(5385): p. 2013-2016.

31. Chan, W.C. and S. Nie, *Quantum dot bioconjugates for ultrasensitive nonisotopic detection.* Science, 1998. **281**(5385): p. 2016-2018.

32. Schlamp, M., X. Peng, and A.-l. Alivisatos, *Improved efficiencies in light emitting diodes made with CdSe (CdS) core/shell type nanocrystals and a semiconducting polymer.* Journal of applied physics, 1997. **82**(11): p. 5837-5842.

33. Mattoussi, H., et al., *Electroluminescence from heterostructures of poly (phenylene vinylene) and inorganic CdSe nanocrystals.* Journal of Applied Physics, 1998. **83**(12): p. 7965-7974.

34. Peng, Z.A. and X. Peng, *Nearly monodisperse and shape-controlled CdSe nanocrystals via alternative routes: nucleation and growth.* Journal of the American Chemical Society, 2002. **124**(13): p. 3343-3353.
35. Dalpian, G.M., et al., *Symmetry considerations in CdSe nanocrystals.* Nano letters, 2006. **6**(3): p. 501-504.
36. Puntes, V.F., et al., *Synthesis of hcp-Co nanodisks.* Journal of the American Chemical Society, 2002. **124**(43): p. 12874-12880.
37. Allen, P.B., *Nanocrystalline Nanowires: I. Structure.* Nano Letters, 2007. **7**(1): p. 6-10.
38. Mao, Y., F. Zhang, and S.S. Wong, *Ambient Template-Directed Synthesis of Single-Crystalline Alkaline-Earth Metal Fluoride Nanowires.* Advanced Materials, 2006. **18**(14): p. 1895-1899.
39. Nishio, K., et al., *Structure and growth mechanism of tetrapod-like ZnO particles.* Philosophical Magazine A, 1997. **76**(4): p. 889-904.
40. Hu, J., Y. Bando, and D. Golberg, *Sn-Catalyzed Thermal Evaporation Synthesis of Tetrapod-Branched ZnSe Nanorod Architectures.* small, 2005. **1**(1): p. 95-99.
41. Cozzoli, P.D., et al., *Shape and phase control of colloidal ZnSe nanocrystals.* Chemistry of Materials, 2005. **17**(6): p. 1296-1306.
42. Zhu, Y.-C., et al., *Nanocable-aligned ZnS tetrapod nanocrystals.* Journal of the American Chemical Society, 2003. **125**(52): p. 16196-16197.
43. Pang, Q., et al., *CdSe nano-tetrapods: controllable synthesis, structure analysis, and electronic and optical properties.* Chemistry of materials, 2005. **17**(21): p. 5263-5267.
44. Asokan, S., et al., *Shape-Controlled Synthesis of CdSe Tetrapods Using Cationic Surfactant Ligands.* Small, 2007. **3**(7): p. 1164-1169.
45. Nobile, C., et al., *Confinement effects on optical phonons in spherical, rod-, and tetrapod-shaped nanocrystals detected by Raman spectroscopy.* physica status solidi (a), 2007. **204**(2): p. 483-486.

46. Manna, L., et al., *Controlled growth of tetrapod-branched inorganic nanocrystals.* Nature materials, 2003. **2**(6): p. 382-385.
47. Teng, X. and H. Yang, *Synthesis of platinum multipods: an induced anisotropic growth.* Nano letters, 2005. **5**(5): p. 885-891.
48. Cozzoli, P.D., et al., *Colloidal synthesis and characterization of tetrapod-shaped magnetic nanocrystals.* Nano letters, 2006. **6**(9): p. 1966-1972.
49. Kanaras, A.G., et al., *Controlled synthesis of hyperbranched inorganic nanocrystals with rich three-dimensional structures.* Nano letters, 2005. **5**(11): p. 2164-2167.
50. Talapin, D.V., et al., *Evolution of an ensemble of nanoparticles in a colloidal solution: theoretical study.* The Journal of Physical Chemistry B, 2001. **105**(49): p. 12278-12285.
51. Park, Jongnam, et al., *Synthesis of monodisperse spherical nanocrystals.* Angewandte Chemie International Edition, 2007. **46**(25): p. 4630-4660.
52. Ojea-Jiménez, I., et al., *Small gold nanoparticles synthesized with sodium citrate and heavy water: insights into the reaction mechanism.* The Journal of Physical Chemistry C, 2010. **114**(4): p. 1800-1804.
53. Whitehead, C.B. and R.G. Finke, *Nucleation Kinetics and Molecular Mechanism in Transition-Metal Nanoparticle Formation: The Intriguing, Informative Case of a Bimetallic Precursor,{[(1, 5-COD) IrI· HPO4] 2} 2–.* Chemistry of Materials, 2019. **31**(8): p. 2848-2862.
54. Strach, M., et al., *Insights into reaction intermediates to predict synthetic pathways for shape-controlled metal nanocrystals.* Journal of the American Chemical Society, 2019. **141**(41): p. 16312-16322.
55. Liu, H., J.S. Owen, and A.P. Alivisatos, *Mechanistic study of precursor evolution in colloidal group II− VI semiconductor nanocrystal synthesis.* Journal of the American Chemical Society, 2007. **129**(2): p. 305-312.
56. Frenette, L.C. and T.D. Krauss, *Uncovering active precursors in colloidal quantum dot synthesis.* Nature communications, 2017. **8**(1): p. 1-8.

57. Hamachi, L.S., et al., *Kinetic control over CdS nanocrystal nucleation using a library of thiocarbonates, thiocarbamates, and thioureas.* Chemistry of Materials, 2017. **29**(20): p. 8711-8719.
58. Niederberger, M. and G. Garnweitner, *Organic reaction pathways in the nonaqueous synthesis of metal oxide nanoparticles.* Chemistry–A European Journal, 2006. **12**(28): p. 7282-7302.
59. Ito, D., et al., *Synthesis of ligand-stabilized metal oxide nanocrystals and epitaxial core/shell nanocrystals via a lower-temperature esterification process.* ACS nano, 2014. **8**(1): p. 64-75.
60. Pokratath, R., et al., *Mechanistic Insight into the Precursor Chemistry of ZrO2 and HfO2 Nanocrystals; towards Size-Tunable Syntheses.* JACS Au, 2022. **2**(4): p. 827-838.
61. Imran, M., et al., *Benzoyl halides as alternative precursors for the colloidal synthesis of lead-based halide perovskite nanocrystals.* Journal of the American Chemical Society, 2018. **140**(7): p. 2656-2664.
62. Tessier, M.D., et al., *Aminophosphines: a double role in the synthesis of colloidal indium phosphide quantum dots.* Journal of the American Chemical Society, 2016. **138**(18): p. 5923-5929.
63. Grigel, V., et al., *InAs colloidal quantum dots synthesis via aminopnictogen precursor chemistry.* Journal of the American Chemical Society, 2016. **138**(41): p. 13485-13488.
64. Chen, Y., et al., *Conversion Mechanism of Soluble Alkylamide Precursors for the Synthesis of Colloidal Nitride Nanomaterials.* Journal of the American Chemical Society, 2018. **140**(33): p. 10421-10424.
65. Qu, L., Z.A. Peng, and X. Peng, *Alternative routes toward high quality CdSe nanocrystals.* Nano letters, 2001. **1**(6): p. 333-337.
66. Yu, W.W. and X. Peng, *Formation of high-quality CdS and other II–VI semiconductor nanocrystals in noncoordinating solvents: tunable reactivity of monomers.* Angewandte Chemie International Edition, 2002. **41**(13): p. 2368-2371.

67. Li, L.S., et al., *High quality ZnSe and ZnS nanocrystals formed by activating zinc carboxylate precursors.* Nano letters, 2004. **4**(11): p. 2261-2264.
68. Manna, L., et al., *Epitaxial growth and photochemical annealing of graded CdS/ZnS shells on colloidal CdSe nanorods.* Journal of the American Chemical Society, 2002. **124**(24): p. 7136-7145.
69. Peng, X., et al., *Epitaxial growth of highly luminescent CdSe/CdS core/shell nanocrystals with photostability and electronic accessibility.* Journal of the American Chemical Society, 1997. **119**(30): p. 7019-7029.
70. Milliron, D.J., et al., *Colloidal nanocrystal heterostructures with linear and branched topology.* Nature, 2004. **430**(6996): p. 190-195.
71. Battaglia, D., et al., *Colloidal two-dimensional systems: CdSe quantum shells and wells.* Angewandte Chemie International Edition, 2003. **42**(41): p. 5035-5039.
72. Battaglia, D., B. Blackman, and X. Peng, *Coupled and decoupled dual quantum systems in one semiconductor nanocrystal.* Journal of the American Chemical Society, 2005. **127**(31): p. 10889-10897.
73. Rogach, A.L., *Semiconductor nanocrystal quantum dots.* Verlag: Wien, 2008.
74. Pradhan, N., et al., *Surface ligand dynamics in growth of nanocrystals.* Journal of the American Chemical Society, 2007. **129**(30): p. 9500-9509.
75. Peng, X. and J. Thessing, *Controlled synthesis of high quality semiconductor nanocrystals.* Semiconductor Nanocrystals and Silicate Nanoparticles, 2005: p. 79-119.
76. De Keukeleere, K., et al., *Stabilization of colloidal Ti, Zr, and Hf oxide nanocrystals by protonated tri-n-octylphosphine oxide (TOPO) and its decomposition products.* Chemistry of Materials, 2017. **29**(23): p. 10233-10242.
77. Wolcott, A., et al., *CdSe quantum rod formation aided by in situ TOPO oxidation.* Chemistry of Materials, 2010. **22**(9): p. 2814-2821.

78. Calcabrini, M., et al., *Ligand Conversion in Nanocrystal Synthesis: The Oxidation of Alkylamines to Fatty Acids by Nitrate.* JACS Au, 2021. **1**(11): p. 1898-1903.
79. Carbone, L., et al., *Synthesis and micrometer-scale assembly of colloidal CdSe/CdS nanorods prepared by a seeded growth approach.* Nano letters, 2007. **7**(10): p. 2942-2950.
80. Dhaene, E., et al., *Monoalkyl Phosphinic Acids as Ligands in Nanocrystal Synthesis.* ACS nano, 2022. **16**(5): p. 7361-7372.
81. Drijvers, E., et al., *Revisited wurtzite CdSe synthesis: A gateway for the versatile flash synthesis of multishell quantum dots and rods.* Chemistry of Materials, 2016. **28**(20): p. 7311-7323.
82. Wang, F., R. Tang, and W.E. Buhro, *The trouble with TOPO; identification of adventitious impurities beneficial to the growth of cadmium selenide quantum dots, rods, and wires.* Nano letters, 2008. **8**(10): p. 3521-3524.
83. Wang, F., et al., *Spectroscopic identification of tri-n-octylphosphine oxide (TOPO) impurities and elucidation of their roles in cadmium selenide quantum-wire growth.* Journal of the American Chemical Society, 2009. **131**(13): p. 4983-4994.
84. Baranov, D., et al., *Purification of oleylamine for materials synthesis and spectroscopic diagnostics for trans isomers.* Chemistry of Materials, 2019. **31**(4): p. 1223-1230.
85. Lang, E.N., et al., *Oleylamine impurities regulate temperature-dependent hierarchical assembly of ultranarrow gold nanowires on biotemplated interfaces.* ACS nano, 2021. **15**(6): p. 10275-10285.
86. Yeh, C.-Y., et al., *Zinc-blende–wurtzite polytypism in semiconductors.* Physical Review B, 1992. **46**(16): p. 10086.
87. Jacobs, K., J. Wickham, and A.P. Alivisatos, *Threshold size for ambient metastability of rocksalt CdSe nanocrystals.* The Journal of Physical Chemistry B, 2002. **106**(15): p. 3759-3762.

88. Faria Junior, P. and G. Sipahi, *Band structure calculations of InP wurtzite/zinc-blende quantum wells.* Journal of Applied Physics, 2012. **112**(10): p. 103716.

89. Landolt, H. and R. Börnstein, *Numerical Data and Functional Relationships in Science and Technology: Geophysics and space research. New series. Group 5*. Vol. 4. 1982: Springer-Verlag.

90. Yu, W.W., et al., *Experimental determination of the extinction coefficient of CdTe, CdSe, and CdS nanocrystals.* Chemistry of Materials, 2003. **15**(14): p. 2854-2860.

91. Hines, M.A. and P. Guyot-Sionnest, *Synthesis and characterization of strongly luminescing ZnS-capped CdSe nanocrystals.* The Journal of Physical Chemistry, 1996. **100**(2): p. 468-471.

92. Dabbousi, B.O., et al., *(CdSe) ZnS core− shell quantum dots: synthesis and characterization of a size series of highly luminescent nanocrystallites.* The Journal of Physical Chemistry B, 1997. **101**(46): p. 9463-9475.

93. Cao, Y.W. and U. Banin, *Synthesis and characterization of InAs/InP and InAs/CdSe core/shell nanocrystals.* Angewandte Chemie International Edition, 1999. **38**(24): p. 3692-3694.

94. Kortan, A., et al., *Nucleation and growth of CdSe on ZnS quantum crystallite seeds, and vice versa, in inverse micelle media.* Journal of the American Chemical Society, 1990. **112**(4): p. 1327-1332.

95. Kim, S., et al., *Type-II quantum dots: CdTe/CdSe (core/shell) and CdSe/ZnTe (core/shell) heterostructures.* Journal of the American Chemical Society, 2003. **125**(38): p. 11466-11467.

96. Balet, L., et al., *Inverted core/shell nanocrystals continuously tunable between type-I and type-II localization regimes.* Nano Letters, 2004. **4**(8): p. 1485-1488.

97. Reiss, P., M. Protiere, and L. Li, *Core/shell semiconductor nanocrystals.* small, 2009. **5**(2): p. 154-168.

98. Talapin, D.V., et al., *Highly luminescent monodisperse CdSe and CdSe/ZnS nanocrystals synthesized in a hexadecylamine− trioctylphosphine oxide− trioctylphospine mixture.* Nano letters, 2001. **1**(4): p. 207-211.
99. Peng, Z.A. and X. Peng, *Formation of high-quality CdTe, CdSe, and CdS nanocrystals using CdO as precursor.* Journal of the American Chemical Society, 2001. **123**(1): p. 183-184.
100. Reiss, P., et al., *Luminescent ZnSe nanocrystals of high color purity.* Materials Chemistry and Physics, 2004. **84**(1): p. 10-13.
101. Protière, M. and P. Reiss, *Highly luminescent Cd1− xZnxSe/ZnS core/shell nanocrystals emitting in the blue–green spectral range.* Small, 2007. **3**(3): p. 399-403.
102. Xinhua, Z., et al., *Alloyed ZnxCd1-xS nanocrystals with highly narrow luminescence spectral width.* Journal of the American Chemical Society, 2003. **125**(44): p. 13559-13563.
103. Furdyna, J.K., *Diluted magnetic semiconductors.* Journal of Applied Physics, 1988. **64**(4): p. R29-R64.
104. Oczkiewicz, B., A. Twardowski, and M. Demianiuk, *Intra-manganese absorption and luminescence in Zn1-xMnxSe semimagnetic semiconductor.* Solid state communications, 1987. **64**(1): p. 107-111.
105. Xue, J., et al., *Temperature evolution of the 2.1 eV band in the Zn1− xMnxSe system for low concentration.* Journal of luminescence, 1998. **78**(3): p. 173-178.
106. Hu, J., et al., *Linearly polarized emission from colloidal semiconductor quantum rods.* Science, 2001. **292**(5524): p. 2060-2063.
107. Kraus, R., et al., *Room-temperature exciton storage in elongated semiconductor nanocrystals.* Physical review letters, 2007. **98**(1): p. 017401.
108. Gudiksen, M.S., et al., *Electroluminescence from a single-nanocrystal transistor.* Nano letters, 2005. **5**(11): p. 2257-2261.
109. Steiner, D., et al., *Zero-dimensional and quasi one-dimensional effects in semiconductor nanorods.* Nano Letters, 2004. **4**(6): p. 1073-1077.

110. Steiner, D., et al., *Determination of band offsets in heterostructured colloidal nanorods using scanning tunneling spectroscopy.* Nano letters, 2008. **8**(9): p. 2954-2958.

111. Talapin, D.V., et al., *Seeded growth of highly luminescent CdSe/CdS nanoheterostructures with rod and tetrapod morphologies.* Nano letters, 2007. **7**(10): p. 2951-2959.

112. Baranov, D., et al., *Assembly of colloidal semiconductor nanorods in solution by depletion attraction.* Nano letters, 2010. **10**(2): p. 743-749.

113. Jana, N.R., *Shape effect in nanoparticle self-assembly.* Angewandte Chemie, 2004. **116**(12): p. 1562-1566.

114. Hu, Z., et al., *Electric-field-driven accumulation and alignment of CdSe and CdTe nanorods in nanoscale devices.* Nano letters, 2006. **6**(11): p. 2585-2591.

115. Nobile, C., et al., *Confined optical phonon modes in aligned nanorod arrays detected by resonant inelastic light scattering.* Nano letters, 2007. **7**(2): p. 476-479.

116. Romero, H.E., G. Calusine, and M. Drndic, *Current oscillations, switching, and hysteresis in CdSe nanorod superlattices.* Physical Review B, 2005. **72**(23): p. 235401.

117. Steiner, D., et al., *Electronic structure and self-assembly of cross-linked semiconductor nanocrystal arrays.* Nanotechnology, 2008. **19**(6): p. 065201.

118. Persano, A., et al., *Photoconduction properties in aligned assemblies of colloidal CdSe/CdS nanorods.* Acs Nano, 2010. **4**(3): p. 1646-1652.

119. Robbie, K., D. Broer, and M. Brett, *Chiral nematic order in liquid crystals imposed by an engineered inorganic nanostructure.* Nature, 1999. **399**(6738): p. 764-766.

120. Acharya, S., et al., *Polarization properties and switchable assembly of ultranarrow ZnSe nanorods.* Advanced Materials, 2007. **19**(8): p. 1105-1108.

121. Acharya, S., et al., *Nanorod-Driven Orientational Control of Liquid Crystal for Polarization-Tailored Electro-Optic Devices.* Advanced Materials, 2009. **21**(9): p. 989-993.

122. Khoo, I.-C., K. Chen, and Y.Z. Williams, *Orientational photorefractive effect in undoped and CdSe nanorods-doped nematic liquid crystal—bulk and interface contributions.* IEEE Journal of selected topics in quantum electronics, 2006. **12**(3): p. 443-450.
123. Li, L.-s. and A.P. Alivisatos, *Origin and scaling of the permanent dipole moment in CdSe nanorods.* Physical review letters, 2003. **90**(9): p. 097402.
124. Saintillan, D., E.S. Shaqfeh, and E. Darve, *Stabilization of a suspension of sedimenting rods by induced-charge electrophoresis.* Physics of Fluids, 2006. **18**(12): p. 121701.
125. Shim, M. and P. Guyot-Sionnest, *Permanent dipole moment and charges in colloidal semiconductor quantum dots.* The Journal of chemical physics, 1999. **111**(15): p. 6955-6964.
126. Nann, T. and J. Schneider, *Origin of permanent electric dipole moments in wurtzite nanocrystals.* Chemical Physics Letters, 2004. **384**(1-3): p. 150-152.
127. Liu, P., *Investigations of electric field assembly of colloidal rod shaped nanocrystals and their device applications.* 2017.
128. Grenci, G., et al., *Preparation and characterization of YBa2Cu3O7− x thick films deposited on silver substrates by the electrophoretic deposition technique for magnetic screening applications.* Superconductor Science and Technology, 2006. **19**(4): p. 249.
129. Wang, Y.C., I.C. Leu, and M.H. Hon, *Kinetics of electrophoretic deposition for nanocrystalline zinc oxide coatings.* Journal of the American Ceramic Society, 2004. **87**(1): p. 84-88.
130. Talapin, D.V., et al., *Prospects of colloidal nanocrystals for electronic and optoelectronic applications.* Chemical reviews, 2010. **110**(1): p. 389-458.

3. Experimental Procedures and Characterisation Techniques

In this work, all the experiments are carried out with different instruments in Bernal in UL. The semiconductors are prepared in the fuming cupboard which is equipped with a temperature controller, heating jacket, stirrer instrument, vacuum system and argon system. After the synthesis, the NCs is purified by a centrifuge with tunable speed and then stored in a refrigerator under 3 ℃. The as-synthesized NCs is characterized by different instrument, for examples, the X-ray diffraction instrument is used for the analysis the crystallinity and component, as well as the size. The micro-structure of the NCs is characterized by the scanning electron microscope. The optical performance of the NCs is observed by a photoluminescence instrument and a ultraviolet visible machine. There are many equipment used for the fabrication of the LED device, such as the spin coater and glovebox. All the characterization of the LED device are performed in the photonics lab.

3.1 Synthetic Experimental Equipment

3.1.1 Hot Injection

The method to prepare semiconductor nanocrystals involved the injection of a "cold" (room temperature) solution of precursor molecules (CdO) into hot liquid trioctylphospine oxide (TOPO) (above 300 °C). For the CdSe synthesis, The precursor solution consisted of Se or S in trioctyl phosphine (TOP). The injection leads to the instantaneous formation of nuclei of CdSe or CdS. Due to a drop in temperature, the formation of new nuclei is prevented. The result is a suspension of reasonably monodisperse nuclei together with considerable amounts of free Cd and Se precursors. Increasing the temperature to higher values leads to slow growth of the existing nuclei but not to new nucleation. The size of the resulting CdSe nanocrystals increases with increasing growth temperature. The omnipresent TOPO molecules (the solvent) slow down the growth considerably by coordinating the surface Cd atoms, thus forming a steric barrier for reactants. The slow growth at relatively high temperatures allows the nanocrystals to anneal and to form nearly defect-free wurtzite lattices, which are identical to the bulk lattice. It is noted that the use of alkylphosphine oxide molecules with shorter alkyl chains as the coordinating solvent leads to a much faster growth, which becomes uncontrolled at a sufficiently elevated temperature (230°C for butylphosphine oxide). After the synthesis, the nanocrystals can be separated from the growth solution by adding a polar solvent, and can then redissolved in a suitable organic solvent to form stable colloidal suspensions. The TOPO molecules remain attached to the surface Cd atoms, and the suspensions are sterically stabilized. Such CdSe nanocrystal suspensions have remarkable optical properties (the well-known size-dependent transmission and emission colors of semiconductor nanocrystals) [1].

3.1.2 Synthesis Experiment

A glass Schlenk line connected to vacuum pump and inert gas, round-bottom flask and temperature control unit are required for the NC synthesis (as shown in Figure 3.1). The three-necked round bottom flask is connected via a condenser to the Schlenk-line which is then connected to the vacuum pump via a tube and through a trap. A second tube from the Schlenk line is connected to an inert gas supply from one side and via an oil bubble to the exhaust. A thermocouple and a rubber septa are sealed in the two necks of the flask served for the temperature measurement and reactants injection respectively. The reaction is carried under an inert atmosphere in the flask with the mixture of ligands, solvent and the metal precursors.

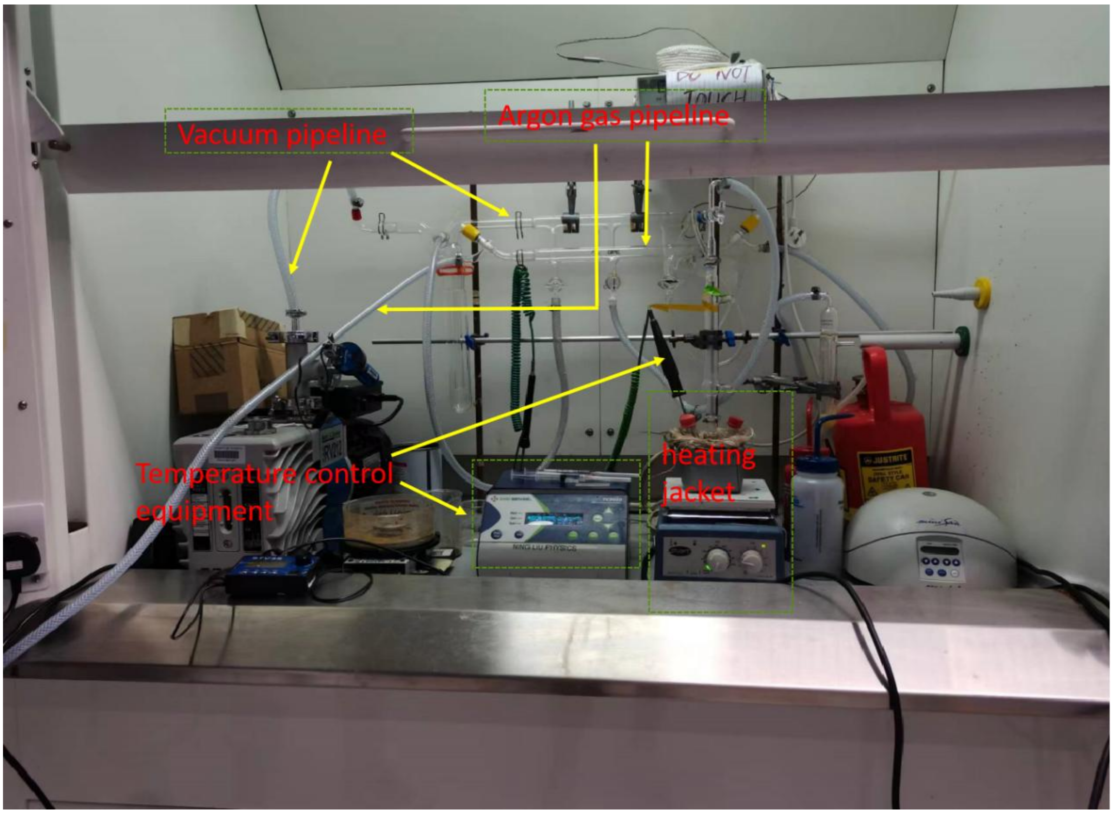

Figure 3.1. closer view of the flask equipped with condenser and thermocouple.

3.1.3 Electrophoretic deposition (EPD)

The principle of the EPD method is directing the orientation of the anisotropic nanoparticle in solution, under the influence of an electric field. The EPD setup includes several parts: the voltage generator, a program with a PC, rotary dip-coater with substrate holder and an electrolyte container (Figure 3.2). To eliminate the effect of disturbance when dipping and withdrawing the substrate, The company designed and installed the EPD sample holder inside a dip coater setup which is remotely controlled by a program. The substrates are automatically lifted, in a constant speed, out from the electrolyte solution when the deposition run finishes. The samples are dried in air for further characterization. A high voltage power supply unit TECHNIX SR-5-F-300, S/N: BU08/04971 is employed with the voltage monitored using a Black Star 3225 MP millimeter.

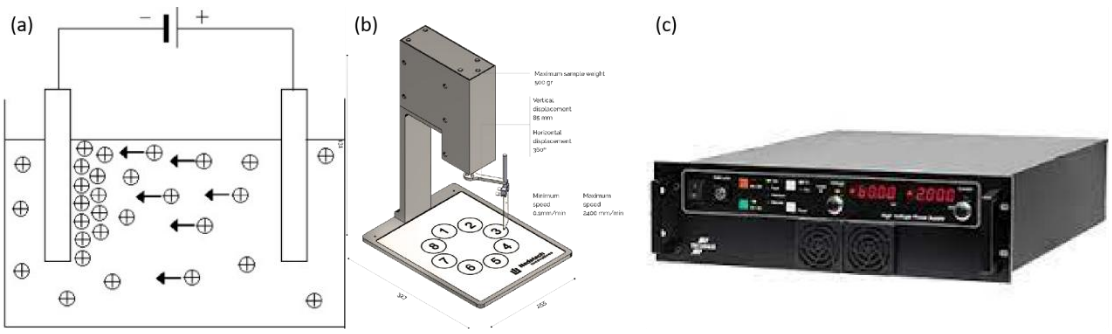

Figure 3.2 (a) Schematic showing the EPD of nanorods in DC field; (b) The rotary dip-coater used in this thesis to perform the EPD; (c) The DC power supplier and the program in the PC for the deposition.

3.2 Characterisation Techniques

3.2.1 Photoluminescence (PL)

Photoluminescence (PL) is used to investigate the separation of photogenerated charge carriers because the PL signal is resulted from recombination of photogenerated electron-hole pairs. Thus, high PL intensity indicates more recombination of charge carriers. In the case of an optimal heterojunction, the PL intensity is quenched due to maximum separation of charge carriers. The lifetime is also used to evaluate the rate of recombination of charge carriers. The longer lifetime plays a vital role in terms of efficient photocatalytic activity.

Photoluminescence is the radiation that is excited after absorbing electromagnetic radiation, and the excited atoms or molecules emit radiation with longer wavelength as the radiation in the process of de-excitation. When the excitation light source stops irradiating the sample, the re-emission process stops immediately, and this re-emitted light is called photoluminescence. A high-intensity lasers can lift a significant number of molecules in the absorbing matter to excited quantum states. Therefore, the sensitivity of photoluminescence spectrum is greatly improved. Laser-based photoluminescence spectroscopy is suitable for the detection of ultra-low concentration samples. The energy of the emitted light (photoluminescence) relies on the gap between the two energy states. (Figure 3.3). The PL Varian Cary Eclipse Fluorimeter was performed in transmission mode as shown in Figure 3.4.

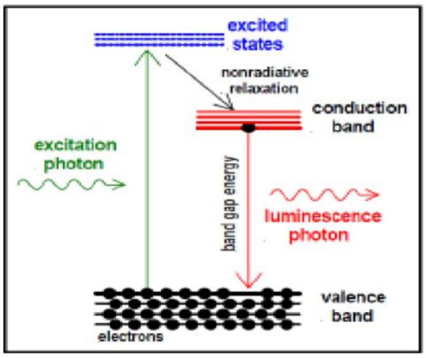

Figure 3.3 Energy diagram showing absorption of light and the processes involved in the emission of light as fluorescence and phosphorescence [2].

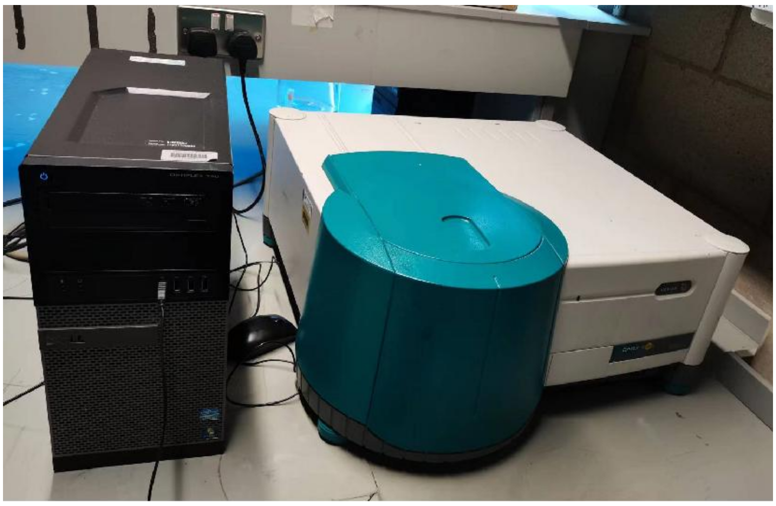

Figure 3.4 The PL Varian Cary Eclipse Fluorimeter

3.2.2 Photoluminescence Quantum Yield (PLQY)

Photoluminescence quantum yield (PLQY) is an important index to evaluate the properties of luminescent materials. It refers to the number of photons emitted per photon absorbed, a fundamental parameter that allows the initial classification of materials, and a quantity that is essential for the detailed analysis of many luminescence systems and processes.

Various ways to determine the PLQY are known. For solutions, a comparative method is frequently used that compares the luminescence of the molecule of interest to the one of a known standard [3]. Another way, which doesn't rely on the comparison to a second material is the direct determination of the PLQY by measuring the number of absorbed photons and the number of emitted photons. This method has originally been introduced by de Mello et al. in 1997 [4], however the basic principle was already published two years earlier from the same group [5]. Nowadays, this technique is widely used and is also tested for solutions. In contrast to the comparative method, the direct determination of the PLQY has several advantages. In addition to this, it is a fast technique and does not rely on a known standard. The PLQY is determined using the equations 3-1、3-2 and Figure 3.5 below [6]:

$$\emptyset_{PL} = \frac{E_{in}(\lambda) - (1-\alpha)E_{out}(\lambda)}{X_{out}(\lambda)\alpha} \qquad 3\text{-}1$$

With

$$\alpha = \frac{X_{out}(\lambda) - X_{in}(\lambda)}{X_{out}(\lambda)} \qquad 3\text{-}2$$

In these equations, $E_{in}(\lambda)$ and $E_{out}(\lambda)$ are the integrated luminescence as a result of direct excitation of the film (sample IN, see Figure 3.5) and secondary excitation (sample OUT), respectively. The latter emission is due to reflected excitation light from sphere walls hitting the sample. X empty(λ) is the Au integrated excitation profile with the empty sphere. α is the film absorptance (Absorptance, α, is the fraction of light absorbed, equal to one minus the transmittance (IUPAC definition), which is obtained by measuring the integrated excitation bands, i.e. the emission signal measured across the excitation wavelength (±5 nm), for two positions of the sample as follows: $X_{in}(\lambda)$ is the integrated excitation when the sample lies directly in the excitation path and $X_{out}(\lambda)$ is the integrated excitation when the excitation light first hits the sphere wall as previously explained.

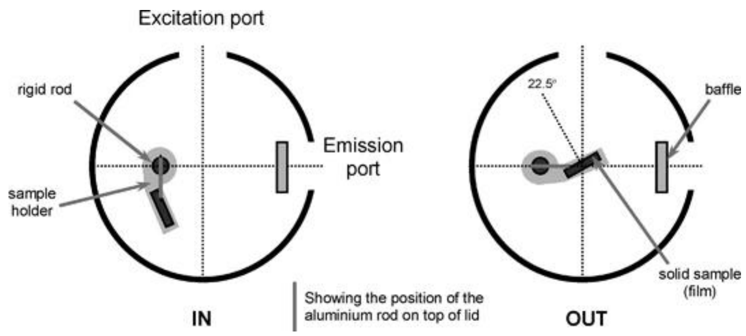

Figure 3.5 Diagram showing the position of the sample within the sphere and the deflecting baffle with the sample in and out of the beam [6].

3.2.3 Scanning Electron Microscopy (SEM)

Scanning electron microscopy (SEM) is a widely used technique for surface topography analysis. Unlike light microscopes, which use photons in the visible spectrum, the image obtained by scanning electrons is produced by the interaction of electron beams in a specific area of the surface of the swept sample. SEM mainly consists of three signals: (1) secondary electron; (2) backscattered electrons; (3) characteristic X-rays. Detectors for these signals can be found in a vacuum chamber (Figure 3.6). In addition, the electron column is the main component of the scanning electron microscope and generally includes: electron gun, lens, scanning coil, scanning emitter, electron collector and high vacuum pump. Sample preparation requirements the sample must be dry, and must be conductive. To make a sample conductive, it is usually coated with a conductive material, such as magnesium and gold, which must be thick enough to allow the current deposited on the sample to circulate, and thin enough so that the surface features of interest are not affected. The accelerated electrons will disappear due to the electron-sample interaction. When the incident electrons are decelerated on the surface of a solid sample, their kinetic energy is used in the generated signal, and secondary electron and backscattering electrodes are commonly used to produce clear and detailed images.

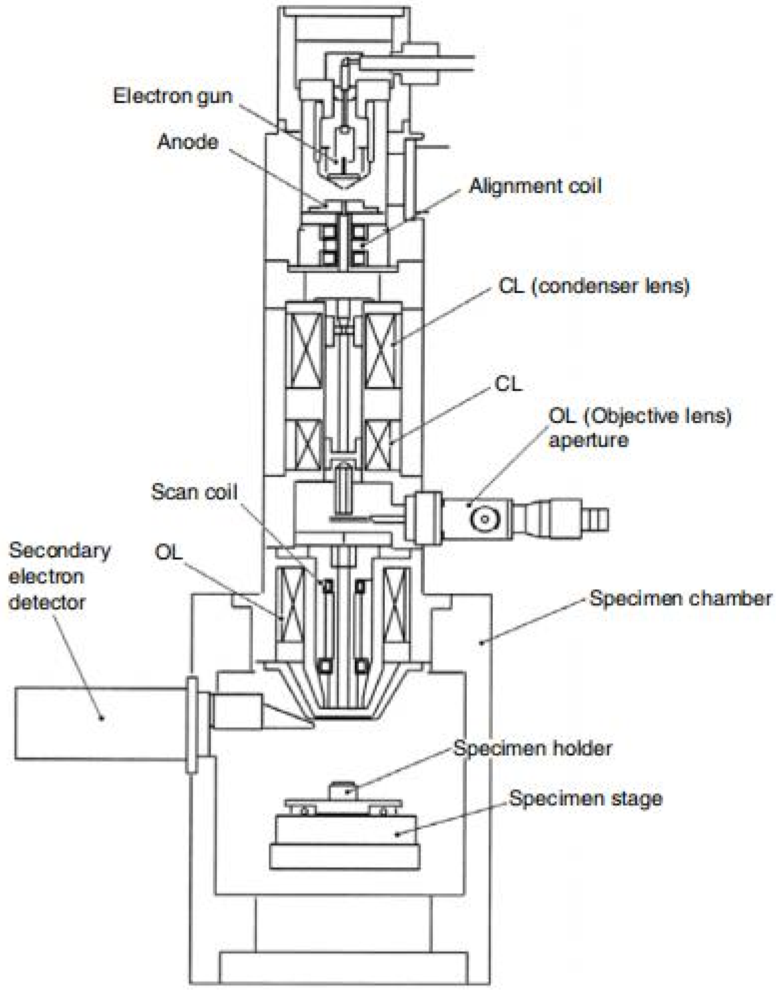

Figure 3.6 Schematic drawing of the SEM [7].

The SEM works by detecting several signals emitted from the interaction between a high energy electron beam and the sample surface (Figure 3.7). Secondary electrons are those generated on the sample surface with energies below 50eV, as opposed to backscattered electrons with energies greater than 50eV. The morphology and shape of the sample are obtained from secondary electrons, while the contrast of the image is obtained from backscattered electrons. For a given speed of light energy, the strength of the backscattered signal depends on the atomic number of the material, where the higher the atomic number, the stronger the strength. The signature X-ray signal provides information about the composition and chemical elements in the sample. X-rays result from inelastic collisions when incident electrons excite electrons in discrete orbitals of atoms in a sample.

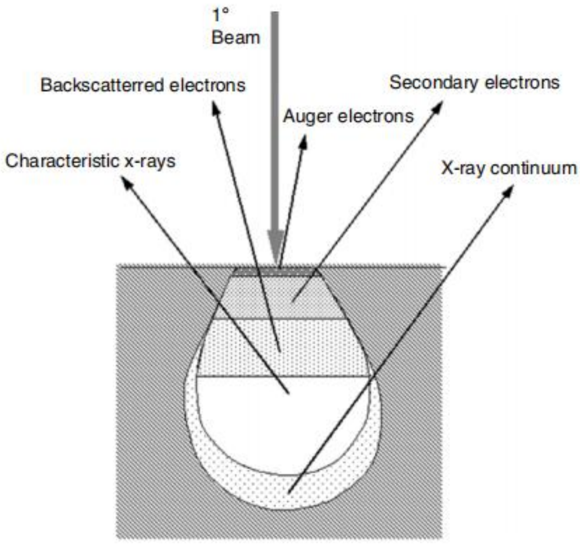

Figure 3.7 The signals generated from the interaction between the high energy electron beam and the specimen [7].

3.2.4 Ultraviolet-Visible Spectroscopy (UV-Vis)

Both ultraviolet and visible absorption spectra belong to semiconductors spectra, which are generated by the transition of valence electrons. The composition, content and structure of a substance can be analyzed, measured and inferred by the UV-Vis spectrum and the degree of absorption generated by the absorption of semiconductors of a substance to ultraviolet and visible light. Stokes shift refers to the red shift of fluorescence spectrum compared with the corresponding absorption spectrum. The solid will absorb photons (absorption) with more energy than the emitting photons (emission), so the emission spectrum will be shifted to a lower energy direction (red shift) compared to the absorption spectrum, the difference in the energy of the two photons. The difference between the wavelength of the excitation peak and the emission peak is a physical constant representing the luminescence properties of semiconductors, which is called the Stokes shift. It represents the energy expended by the semiconductors during its excited lifetime before returning to the ground state. The excited state semiconductors quickly reach the lowest vibrational level of the first excited singlet state through internal transformation and vibrational relaxation process, which is the main cause of Stokes shift. Fluorescent emission may cause the excited semiconductors to return to various vibrational levels in the ground state, and then further loss of energy, which also produces a Stokes shift. In addition, the interaction between the excited state semiconductors and the solvent molecule will also increase the Stokes shift.

Spectroscopy in the ultraviolet, visible (Vis) and nearinfrared (NIR) region of the electromagnetic spectrum is often called electronic spectroscopy because electrons are transferred from low-energy to high-energy atomic or molecular orbitals when the material is irradiated with light. Such electron transfer processes may take place in transition metal ions (d-d transitions and ligand-to-metal or metal-toligand charge transfer transitions), and inorganic and organic molecules (mainly n - r* and Tr - a* transitions). They are responsible for the color of matter. Spectroscopic investigations of solutions, gas phase and individual crystals usually take place in transmission, but it is very difficult to obtain transparent films of powders and solids (e.g., heterogeneous catalysts), making transmission experiments almost impossible [8]. In this thesis, the UV-Vis-NIR spectroscopy of nanocrystals dispersed in solution was performed in transmission mode as shown in Figure 3.8.

Figure 3.8 UV-Vis-NIR spectroscopy

3.2.5 X-ray diffraction (XRD)

3.2.5.1 Wavelength and X-rays

In the electromagnetic radiation spectrum, the wavelength in the range of 0,001-2.5 Angstrom is X-ray. It can be divided into two types according to the difference of the penetrating power of its wavelength: hard X-ray and soft X-ray. Hard X-ray has a short wavelength of 0.05-0.1 Angstrom and a strong penetration. Soft X-ray has a long wavelength of 0.1-0.5 Angstrom and a weak penetration (Figure 3.9). X-rays are actually electromagnetic waves of very short wavelength and high energy.

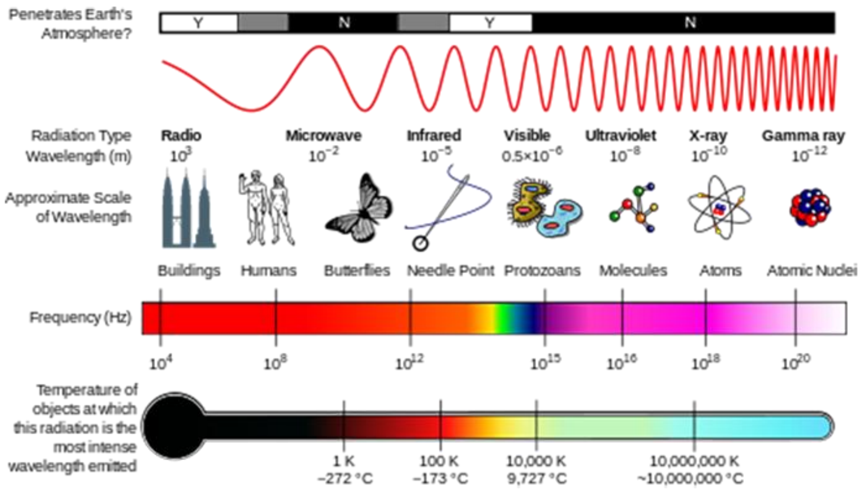

Figure 3.9 The wavelength from Gamma ray to radio [9]

Professor Rontgen (1845-1923), president of the University of Wuerzburg and director of the Institute of Physics, discovered X rays when he was engaged in the research of cathode rays [10]. The simplest way to produce X-rays is to hit a metal target with an accelerated electron. Bremsstrahlung is a continuous part of the X-ray spectrum. By increasing the acceleration voltage, the electrons carry more energy, and it is possible to knock the inner electrons out of the metal atoms. Thus, holes are formed in the inner layer, and the outer electrons transition back to the inner layer to fill the holes, while releasing photons with a wavelength of about 0.1nm. Because the energy emitted by the outer electron transition is quantized, the wavelength of the emitted photon is also concentrated in some parts, forming characteristic lines in the X spectrum, which is called characteristic radiation. It must be known that X-rays are invisible and imperceptible rays, which can cause harm to the human body.

3.2.5.2 XRD Theory

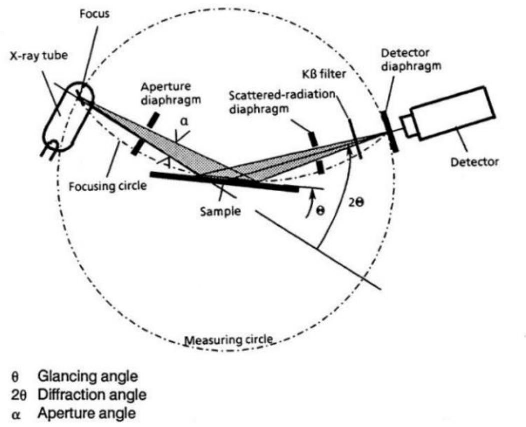

Figure 3.10 Schematic illustration of in situ HE-XRD measurements [11].

X-ray diffraction (XRD), which uses the diffraction phenomenon of X-rays in crystals to obtain the characteristics of the X-ray signal after diffraction, and then obtains the diffraction pattern after processing (Figure 3.10). Using the spectrogram information, we can not only determine the phase with the conventional microscope, but also have a "perspective eye" to see whether there are defects (dislocations) and lattice defects in the crystal.

X-rays are produced by a high-speed flow of electrons or other high-energy radiation (γ rays, neutrons, etc.) that suddenly slows down when it collides with other material and interacts with the inner atoms of the material. Different targets, with different atomic numbers and different electron configurations in their outer layers, produce different wavelengths of characteristic X-rays. The XRD results of the longer wavelength target show that the peak position of the diffraction pattern is regularly stretched along the 2θ axis. The XRD spectra of the short wavelength target are regularly compressed along the 2θ axis. However, it should be noted that the value of sample plane spacing D obtained from the obtained diffraction spectrum is consistent regardless of the type of target used in the X-ray tube, independent of the target (Figure 3.11).

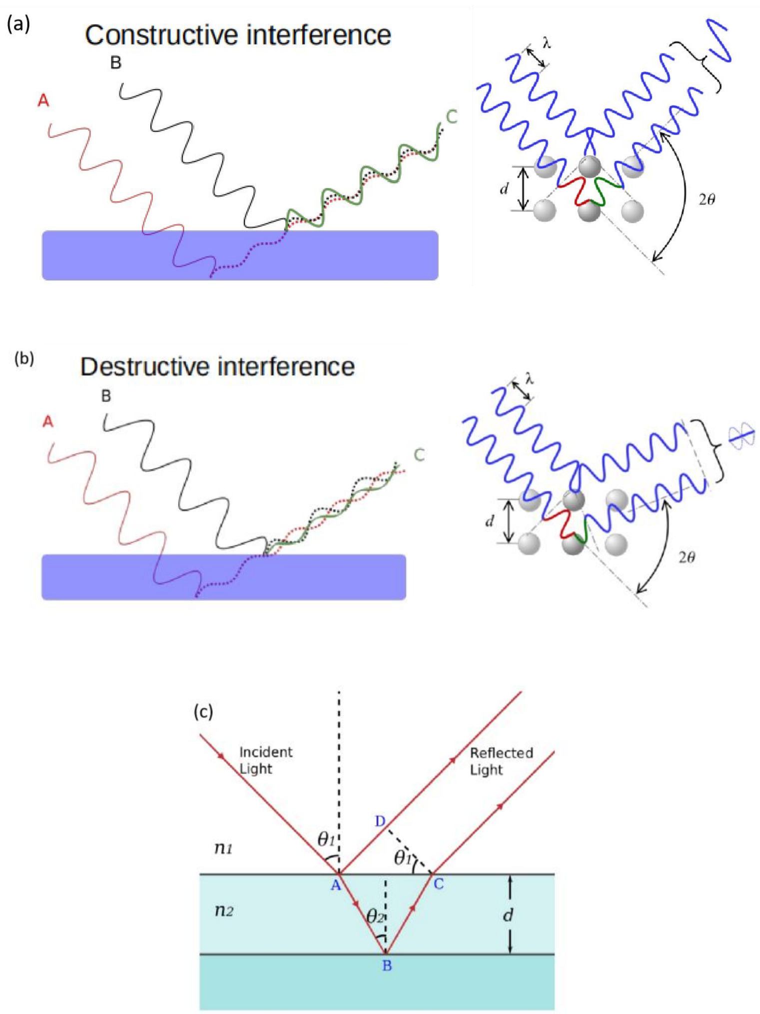

Figure 3.11 The schematic diagram of the constructive interference (a), destructive interference (b) and constructive interference in the XRD analysis (c) [12].

Bragg equation is shown below:

$2d\sin\theta = n*\lambda$ 3-3

Where θ is the incident angle, d is the spacing between crystal planes, n is the diffraction series, λ is the wavelength of entry ray, and 2θ is the diffraction Angle. The Bragg equation reflects the relationship between the direction of the diffraction line and the crystal structure. For a specific crystal, only the entry Angle satisfying Bragg equation can produce interference enhancement and show diffraction pattern (Figure 3.11 c). This is the fundamental meaning of the XRD pattern.

3.2.5.3 XRD phase analysis

With the improvement of XRD standard database, XRD phase analysis becomes more and more simple. At present, the most common operation is to compare the XRD pattern of the sample with the standard spectrum to determine the phase composition of the sample. XRD standard database includes JCPDS (PDF card), ICSD, CCDC, etc., analysis of XRD pattern software including Jade, Xpert Highscore, etc. Jade is recommended here. If the crystallization is not good, the diffraction is not obvious. So the clarity of the crystal is judged by the intensity of the diffraction. Therefore, the intensity of diffraction peaks is used to analyze the crystallinity of the lattice.

In practice, the area obtained by the integration of the strongest diffraction peak (As) is generally taken as an index to calculate the crystallinity, and compared with the area obtained by the integration of the reference substance (Ag), the crystallinity is As/Ag*100%. If one phase of a perfect crystal is replaced by another phase, then the peak strength will also change, which is the basis of quantitative analysis of phase content. The main K value method is also called RIR method and Rietveld full spectrum refinement quantitative. Among them, the basic principle of RIR method is that when a mixed material and corundum (Al_2O_3) are 1:1, there will be a ratio of the integral intensity of the strongest diffraction peak, which is the RIR value. The integral strength RIR value of the substance can always be converted to the integral strength of Al_2O_3. For a mixture, all the components in the substance are converted in this way, and finally the percentage of a particular component can be obtained by normalization.

3.3 LED Fabrication and Characterization

The device is made in a glovebox equipped with a thermal evaporator and a spin coater as shown in Figure 3.12. For the details of the LED fabrication: Glass substrates with patterned indium tin oxide (ITO) were first cleaned with deionized (DI) water, acetone and isopropanol for 20 min respectively. The substrates were dried by Argon. The hole transport layer (HTL), PEDDOT:PSS and poly(9-vinylcarbazole) (PVK) in chloroform, 8 mg • ml^{-1}, were deposited by spin coating followed by annealing at 120 ℃ for 10 min. Next, the sample was moved outside the glove box and CdSe/CdS (in toluene, 0.8 mg • ml^{-1}) was deposited by EPD. For the electron transport layer (ETL), ZnMgO in ethanol, 30 mg • ml^{-1} was spin-coated layer by layer with 3000 rpm for 30s, and annealed at 125 ℃ for 10 minutes respectively. Finally, Al electrodes (100 nm) were deposited using a thermal evaporation system through a shadow mask under a high vacuum of $\sim 1 \times 10^{-6}$ torr. The device area was 4 mm^2 as defined by the overlapping area of the ITO and Al electrodes. The devices were encapsulated in the glove-box by the cover glasses using ultraviolet-curable resin.

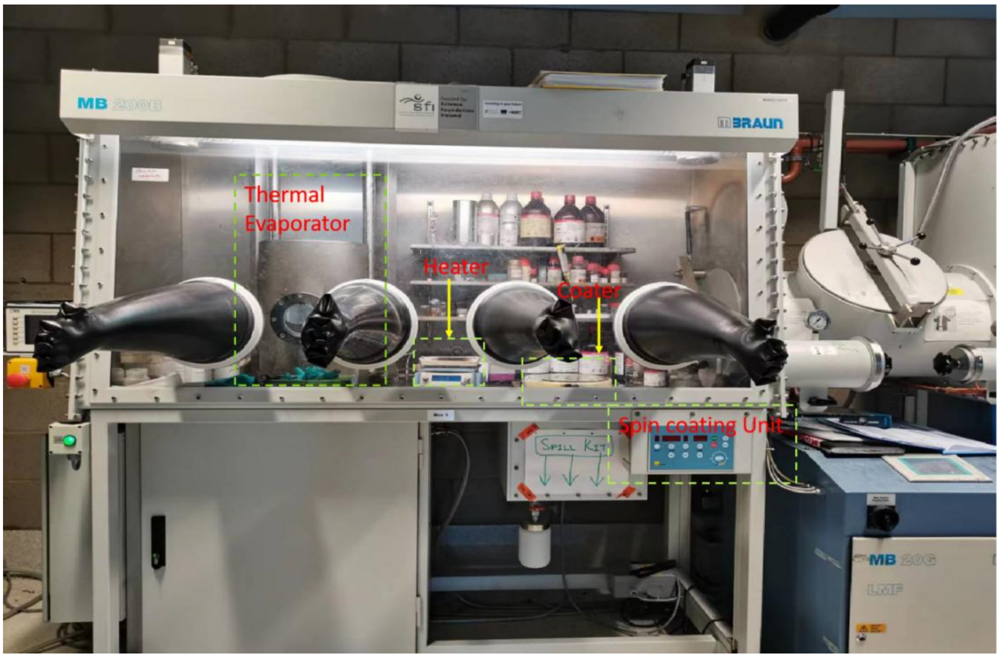

Figure 3.12 MB 20G glovebox and thermal evaporator

The electroluminescence (EL) spectra, L–J–V characteristics and external quantum efficiency (EQE) were collected by using a Keithley 2602 B source, a HMO3004 oscilloscope, an 4P3 XE25A90 integration sphere from Thorlabs, an PDA200C photodiode amplifier and a HR2000+ES spectrometer for light output measurements (Figure 3.13). The details of the theory of the EQE can be found in the ref. [13].

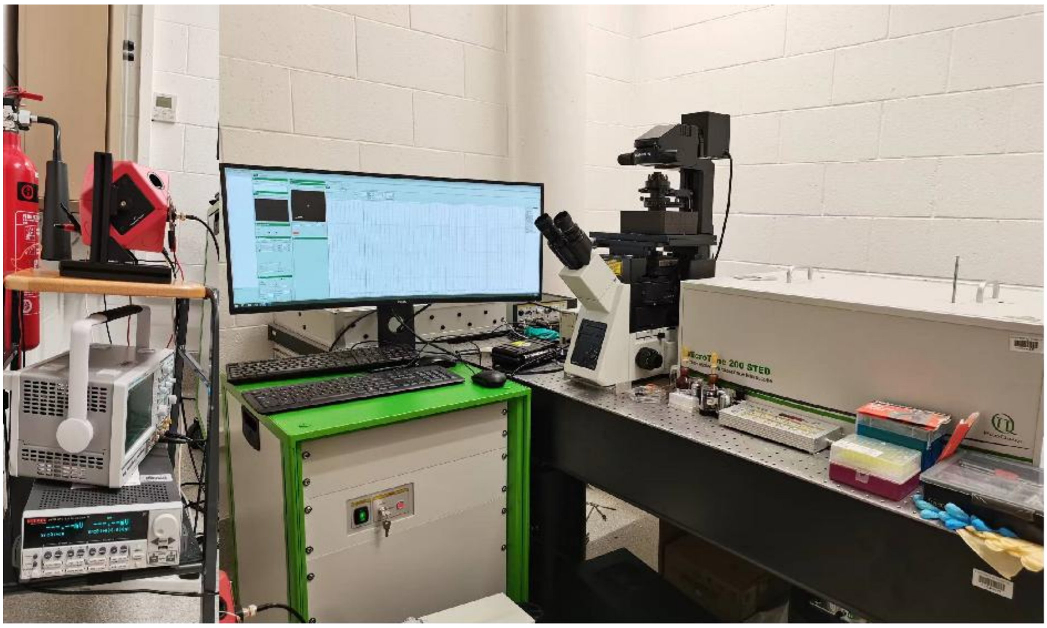

Figure 3.13 The unit for EQE test

Reference

1. Murray, C., D.J. Norris, and M.G. Bawendi, *Synthesis and characterization of nearly monodisperse CdE (E= sulfur, selenium, tellurium) semiconductor nanocrystallites.* Journal of the American Chemical Society, 1993. **115**(19): p. 8706-8715.
2. Vallikkodi, M., *Synthesis, growth and characterization of piperazinium P-aminobenzoate and piperazinium P-chlorobenzoate nonlinear optical single crystals.* Alagappa University, Karaikudi, India, 2018.
3. Weber, G. and F. Teale, *Determination of the absolute quantum yield of fluorescent solutions.* Transactions of the Faraday Society, 1957. **53**: p. 646-655.
4. de Mello, J.C., H.F. Wittmann, and R.H. Friend, *An improved experimental determination of external photoluminescence quantum efficiency.* Advanced materials, 1997. **9**(3): p. 230-232.
5. Greenham, N., et al., *Measurement of absolute photoluminescence quantum efficiencies in conjugated polymers.* Chemical physics letters, 1995. **241**(1-2): p. 89-96.
6. Porres, L., et al., *Absolute measurements of photoluminescence quantum yields of solutions using an integrating sphere.* Journal of fluorescence, 2006. **16**(2): p. 267-273.
7. Zhou, W., et al., *Fundamentals of scanning electron microscopy (SEM)*, in *Scanning microscopy for nanotechnology*. 2006, Springer. p. 1-40.
8. Weckhuysen, B.M., *Ultraviolet-visible spectroscopy.* 2004.
9. Brune, W., *How is energy related to the wavelength of radiation.* Penn State University. Retrieved from www. e-educa tion. psu. edu/meteo300/print/book/export/html/682, 2020.
10. Dennerl, K., J. Englhauser, and J. Trümper, *X-ray emissions from comets detected in the Rontgen X-ray satellite all-sky survey.* Science, 1997. **277**(5332): p. 1625-1630.

11. Bearnot, A. and A. Greene, *Study and Comparison of Coins by X-ray Diffraction (XRD); Preliminary Findings*.
12. Berthold, C. and S.M. Mentzer, *X-ray microdiffraction*, in *Archaeological soil and sediment micromorphology*. 2017, John Wiley & Sons Hoboken, NJ. p. 417-429.
13. Liu, M., Rong, B. and H. W. Salemink, *Evaluation of LED application in general lighting*, Optical Engineering, 2007. **46**(7): p. 074002-074007.

4. The Synthesis and Characterization of CdSe, CdS and $CdSe_{1-x}S_x$ Nanorods

4.1 Introduction

Since many fundamental properties of semiconductor materials have been expressed as a function of size and shape, controlling the size and shape of semiconductor nanocrystals would provide opportunities of tailoring properties of materials and offer possibilities for observing interesting and useful physical phenomena [1] [2]. Therefore, the engineering of materials in nanometer-scale has attracted much attention in optics, electronics, magnetics, catalysis, and ceramics [3]. To control the size and shape of nanocrystals, all kinds of templates, such as liquid crystals, self-assembled monolayers (SAMs), polymers, or porous aluminum oxide, were used [4] [5] [6].

Material scientists are attempting to produce novel materials. Development of a controlled-synthesis method is always the most important goal. One-dimensional nanostructures as building blocks for many novel functional materials are currently the focus of considerable interests [7] [8]. CdS, CdSe, and CdTe are synthesized because of their potential importance as nonlinear optical materials [9], quantum size effect semiconductors [10], materials for electroluminescent devices [11], and other interesting physical properties and chemical properties. They are also functional materials with technological applications [12] [13].

A fascinating phenomenon which characterizes semiconductors in the nanoscale regime is the ability to control the physical properties of the system through its dimensionality, as was demonstrated for a large number of systems including 2D quantum wells, 1D nanowires, and 0D quantum dots. Heterostructured nanorods, which are composed of two or more types of semiconductors, present an exciting example for a system in which the physical properties are strongly influenced by the 1D nature of the entire particle, but also incorporate the effects of the dimensionality, dimensions, and composition of each component on its own.

The ongoing progress in colloidal synthesis of nanocrystals allows one nowadays to synthesize a variety of nanorods with different compositions and structures, ranging from seeded nanorods to rods with asymmetric spatial compositions. The unique properties of these systems, with reduced and mixed dimensionality, attract a growing interest from the scientific point of view, and are also attractive for a range of applications including solid state lighting, lasers, light emitting diodes, flat panel displays, bio-labeling, and solar cells [14].

As is the case in other structures, the physical properties of nanorods are strongly dependent on their potential energy profile, which is governed by the chemical composition of each of the individual components constructing the system. The band-structure, together with the geometry of the system, plays a major role in determining the physical properties of the particles and in particular their spectroscopic characteristics.

The well-controlled one-dimensional arrangement of nanocrystals into electronic circuits, or nanooptical elements, is yet a “state-of-the-art” problem. Synthesized for the first time a few decades ago, CdSe nanorods [15] became exciting materials due to some important properties: up to 100% polarized luminescence [16]. Linearly arranged highly luminescent CdSe nanocrystals could be utilized as nanoemitters or high-resolution detectors of polarized light (recently, this idea was demonstrated on InP rods [17]). It has been shown that, when dispersed at high density in a organic solvent, CdSe nanorods spontaneously form liquid crystalline phases [18]. It is of great interest to use external electric and magnetic fields to align these liquid crystalline samples in order to achieve the manipulation of their orientations on a large scale. The nanocrystal LED made by aligned nanorods arrays with the assistance of electric field (electrophoretic deposition, EPD) is one of promising applications. The permanent electric dipole moments and net charge of the nanorods play an important role in the EPD process [19]. The large permanent electric dipole moment along the long axes of the nanorods has important consequences on the thermodynamic stability of liquid crystalline phases of CdSe nanorods. Further, the large permanent electric dipole moment of the ground state should influence the spatial distribution of optically generated electronhole pairs, with consequences for both linear and nonlinear optical properties of the nanorods [20].

Among various chalcogenide compounds, CdS and CdSe are the most commonly studied sensitizers due to their suitable band gap of 2.4 and 1.7 eV, respectively, and the synergistic effect of cosensitization [21]. Another heterogeneous nanostructure is the alloyed CdSeS nanoparticles. Controlling the composition of the different elements in the alloy provides a good mean of tuning the band gap of the nanoparticles [22].

4.2 Experiments

4.2.1 Chemicals

All reagents were used as received without any further purification. Cadmium oxide (> 99 %), trioctylphosphine (TOP, 97 %), trioctylphosphine oxide (TOPO, 99 %), selenium (99.98 %) and sulfur (99 %) were purchased from Sigma-Aldrich, Tetradecylphosphonic acid (TDPA, > 99 %) and n-hexylphosphonic acid (HPA, > 99 %) were obtained from Aladdin. Silicon wafers were purchased from Si-Mat.

4.2.2 Synthesis of Cadmium Selenium Nanorods

The basic synthesis route followed as reported via hot-injection method. The mixture of 0.2g of CdO, 0.71 g of TDPA, 0.16 g of HPA and 3.0 g of TOPO were loaded into a 25ml three-neck reaction flask and heated to 120 °C in argon, then evacuated under vacuum for 1 hour, and followed by refilling with argon and heated to 310 °C, during which the CdO decomposed and the colour of solution change from brown to optical clear. When the temperature reached 300 C, 1.8 ml of TOP was injected into the flask. The 0.5 ml of selenium stock solution prepared in TOP (0.146 g Selenium + 0.832 l TOP) was rapidly injected when temperature rises to 310 °C, causing a gradual colour change to reddish-brown. After injection, the growth was allowed to continue for 10 min with continuous stirring. Subsequently, the heating mantle was removed and the reaction vessel was allowed to cool down to 80 °C. The nanorods were then washed with anhydrous toluene and isopropanol (1:2) and centrifuge in 5000 rpm for 8 min to remove access ligands.. The precipitate was collected and kept for subsequent deposition.

4.2.3 Synthesis of Cadmium Sulfide Nanorods

0.165g of CdO, 0.625 g of ODPA, 0.165 g of HPA and 2.175 g of TOPO were loaded into a 25 ml threeneck flask and heated to 110 °C under Argon gas flow at which TDPA and TOPO were dissolved. The mixture is evacuated to 150-200 mTorr at 110°C for 30 minutes and then heated to 300°C under Argon gas at which CdO completely dissolves and the solution becomes clear. The mixture is cooled to 110°C and further degassed for another 30 minutes under similar vacuum range (150-200 mTorr). After this second degas, the apparatus is switched back to Argon gas line and the mixture was heated to 300°C at which 1.0 ml of sulfur stock solution (0.65 g of Sulphur powder dissolved in 8.25 g of TOP) was injected. After injection, nanocrystals grew at 300°C for 30 minutes to reach the desired size.

4.2.4 Synthesis of Cadmium Selenium Sulfide Nanorods

The basic synthesis route followed as reported with minor changes. CdO (0.11g, 1 mmol), TOPO (1.45 g, 3.87 mmol), HPA (0.11 g, 0.66 mmol) and TDPA (0.3758 g, 1.35 mmol) the mixture was heated to 120 ºC and evacuated under vacuum for 30 min, then refilled with argon, heated to 330 ºC forming a colorless solution. When the temperature reached 300 ºC, TOP (0.84 g, 2.26 mmol) was injected into the flask. The Se-S stock solution (sulfur (12.025 mg, 0.375 mmol) and selenium (49.35 mg, 0.625 mmol) powder prepared in 500 μL of TOP) was rapidly injected when temperature raise to 330 ºC, causing a gradual color change. After injection, the growth was allowed to continue for 15 min with stirring. Subsequently, the heating mantle was removed and the reaction vessel was allowed to cool down to 160 ºC. The nanorods were then washed with 5 ml of anhydrous toluene and 10 ml of isopropanol and centrifuge in 5000 rpm for 8 min to remove access ligands. The percepitate was collected and kept for subsequent deposition.

4.3 Characterization

The SEM analysis was undertaken with a Hitachi SU-70 scanning electron microscope. TEM analysis was undertaken with JEOL JEM-2010 field emission electron microscopes.

The PL was carried out in the dark room. In our case, the sample was illuminated by a 405 nm laser and the emission was collected by the objective, passed through a cut-filter and pinhole either to CCD-video camera or a spectrometer equipped with a cooled CCD camera. All optical experiments have been done at room temperature.

The EPD was carried out using a 300 V potential that was applied for 2 min between the two electrode separated in 1 cm distance, with a high voltage power supply unit (TECHNIX SR-5-F-300, S/N: BU08/04971) and the voltage was monitored using a digital multimeter (Thurlby Thandar TTi 1604). The deposition was performed at room temperature, during which the electrode was completely immersed in a deposition tank containing a solution of toluene and nanorods at a concentration of 0.20 mg/ml. The silicon wafer attached to the electrode should be thoroughly cleaned before use. After deposition, the samples were removed from the solution and dried slowly in air atmosphere for 10 minutes.

4.4 Results and Discussion

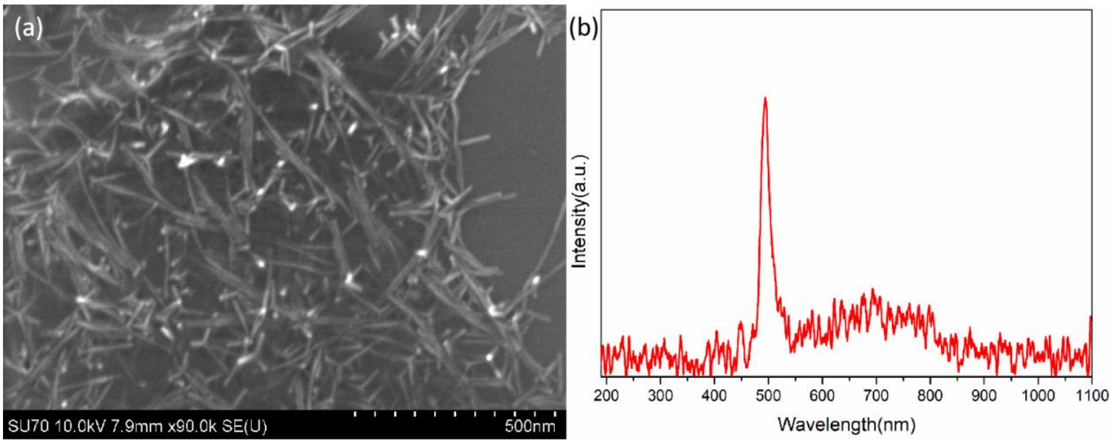

Figure 1: (a) SEM image of CdS; (b) PL spectrum of CdS.

The prepared CdS nanorods are shown in Figure 1(a). The average diameter of the nanorods is around 3 nm while the size distribution in length shows a wide range from 20nm to 300 nm. This may be due to the uneven reaction rate, which is related to the reaction temperature distribution, reaction reagent selection and dosage. The CdS nanorods exhibit two distinct emission bands which are centred at 491.8 nm and at 700 nm (shown in Figure 1(b)). The first emission band is associated with the electronic transition from conduction band to valence band and the second emission band is due to the recombination via localized surface states [23], a transition from interstitial cadmium to valence band [24]. The PLQY of the CdS is as lower as 0.17% because of the surface state. The PLQY of the nanocrystals can be improved by engineering a thin shell on the surface of the cores, which is due to the passivation of surface-deep trap states of the core by the shell coating [25]. Using density functional theory (DFT) Sargent's group has demonstrated that the steric considerations prevent these organic ligands from infiltrating the hard-to-access trenches on the surface of NCs, causing unpassivated metal surface sites to remain which may lead to the lower efficiency [26]. Therefore, ligands exchange with a short chain is another way to improve the PLQY.

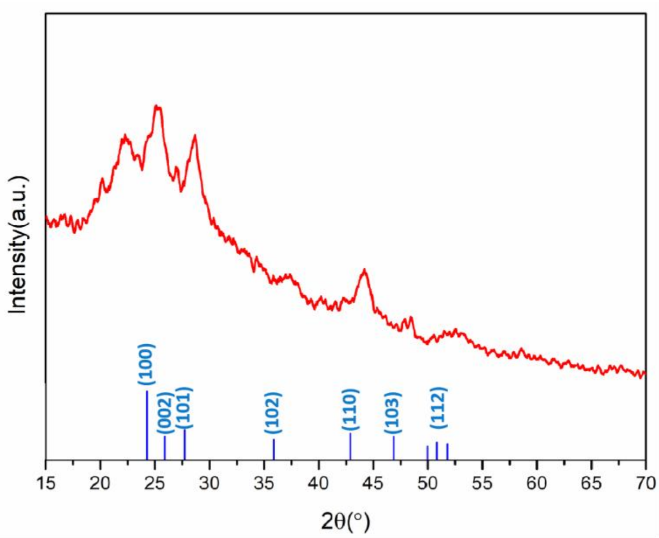

Figure 2: X-ray diffraction pattern of CdS nanorods.

The phase and average particle size of CdS nanorods were analyzed by XRD. As shown in Figure 2, all diffraction peaks can be labeled as hexagonal CdS, which is consistent with the results of JCPDS document 50-0720. The XRD peaks correspond to the reflections of the (100), (002), (101), (102), (110) and (103), (112) planes of the hexagonal CdS, respectively. The widening of diffraction peak indicates the formation of CdS nanocrystals.

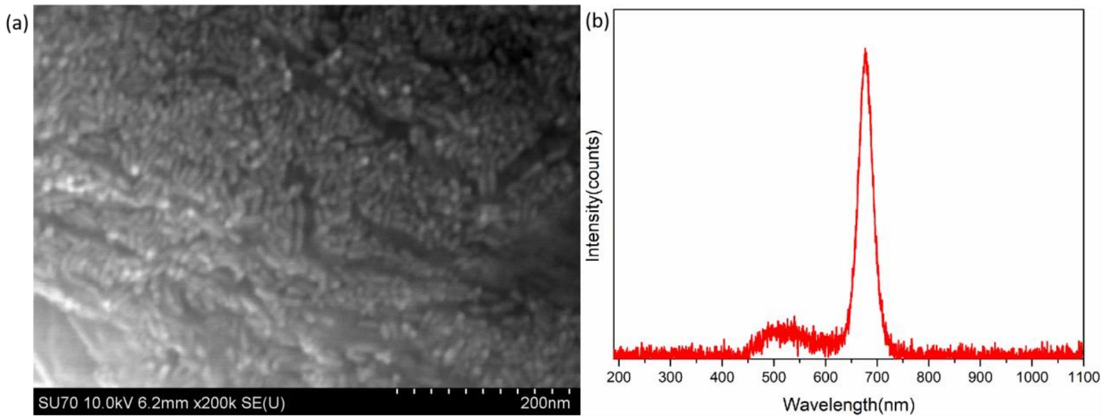

Figure 3: (a) SEM image of CdSe-330; the length is about 25-30 nm, the diameter is about 6-7 nm, the size distribution is not particularly uniform. (b) the CdSe-330 PL is 680 nm, the FWHM is 31.9 nm;

The selective growth of CdSe nanorods is achieved by injection of TOP-Se precursor to TOPO solution containing CdO, HPA and TDPA (see 4.1.4 for experimental details). Heating this mixture at 330 °C under 120 mTorr Ar for 15 min results in the growth of CdSe nanorods of mean diameter of 6.5 nm and a length distribution of 25-30nm (Figure 3(a)). After purification of the CdSe rods from unreacted Cd^{2+} and S^{2-} ions, the optical properties of the nanorods was studied. The photoluminescence (PL) spectra of the CdSe nanorods is shown in Figure 3(b) . Upon CdSe growth, the emission onset exhibits a broad peak at the wavelength around 510 nm (the FWHM is around 65 nm), and a sharp peak at the wavelength of 680 nm with a FWHM of 31.9 nm. This difference might be attributed to the different size in diameter in the CdSe solution. The emission intensity of CdSe at 680 nm was found to be 20 times higher than that of 510 nm, which may mean that there was only small amount of CdSe with the size below 6.5 nm in this reaction.

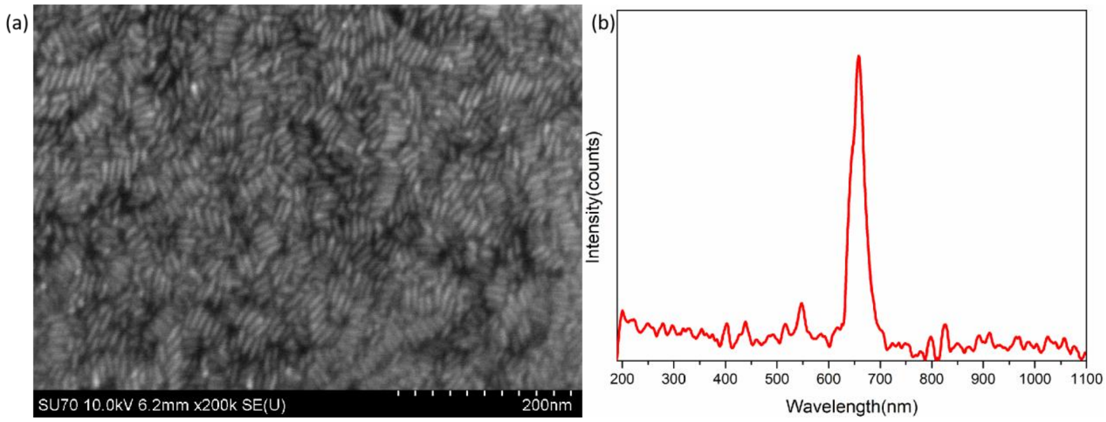

Figure 4: (a) SEM image of CdSe-320; the length is about 40 nm, the diameter is about 5.5 nm, the size distribution is relatively uniform. (b) The PL of CdSe-320 is 665nm; the FWHM is 21nm.

CdSe nanorods 40 nm in length and 5.5 nm in diameter (Figure 4(a)) were synthesized at the temperature of 320 °C for 15 min. Nanorods possess a photoluminescence band centered around 665 nm, with a FWHM of 21 nm (Figure 4(b)). Also, there was no other peak obtained in the PL spectrum. Compared with CdSe-330 sample, the big improvement in the size distribution in CdSe-320 samples could be attributed to the lower growth rate of the CdSe nanocrystals at 320 °C than those of CdSe-330 samples. Slow growth helps to form an even core at low temperature, which then becomes an even size in length.

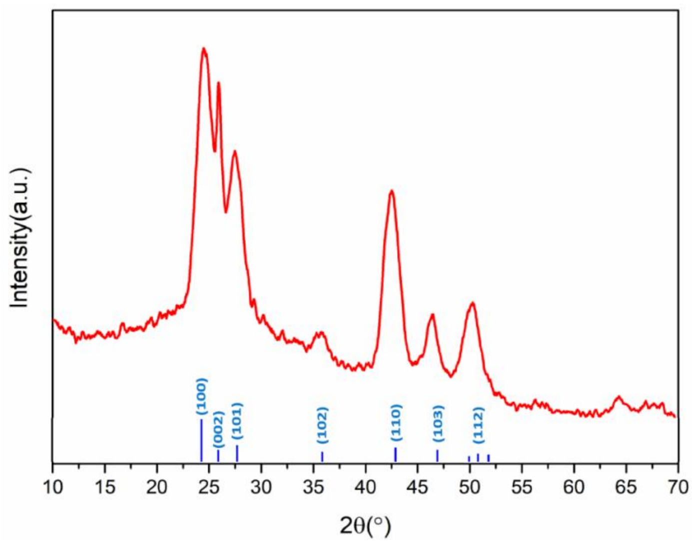

Figure 5: X-ray diffraction pattern of CdSe nanorods.

Figure 5 shows the XRD pattern of the synthesized CdSe nanorods with all the diffraction peaks corresponding to the hexagonal wurzite phases of CdS (JCPDS 41-1049). The peaks are identified to originate from (1 0 0), (0 0 2), (1 0 1), (1 0 2), (1 1 0), (1 0 3), and (1 1 2) planes of hexagonal wurtzite phase of CdS. The mechanism for the formation of wurzite CdSe is still under investigation, the strong chelation between Cd^{2+}, TDPA and HPA must be a reason for the formation of wurzite CdSe. The products are pure in phases with the calculated lattice constants, a=4.215 Å, b=4.215 Å and c=6.872 Å, which are in good agreement with the values given in JCPDS 41-1049. The presence of sharp diffraction peaks in the XRD confirms that the products are crystalline. The average grain size (D) of CdSe is calculated by the Debye–Scherrer formula, $D=0.9\lambda/\beta \cos \theta$, where, λ is the wavelength of CuKα line, β is full width at half maximum and θ is the diffraction angle. From the XRD analysis, the average particle size of the nanorods was estimated as 5.5 nm.

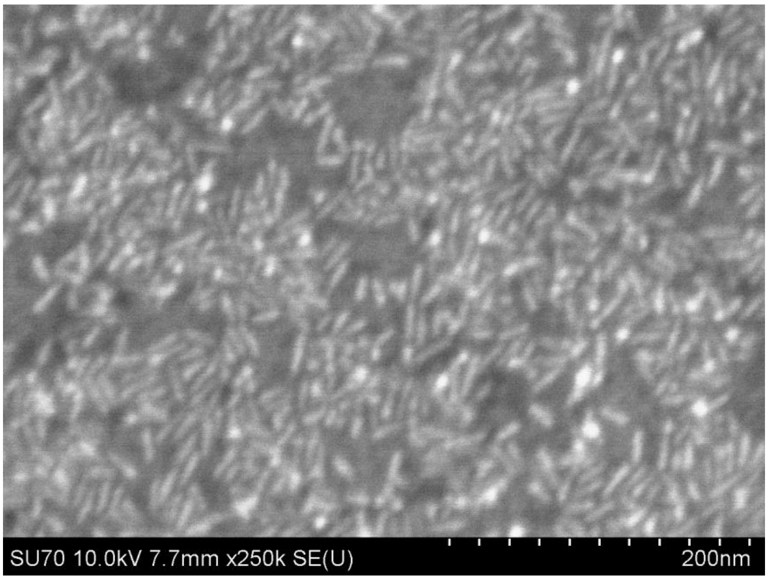

Figure 6 CdSe nanorods layer obtained via EPD

When an external DC electric field (300 V) is applied to the CdSe suspension, these nanorods are driven towards the opposite electrode and deposit forming a layer (Figure 6). SEM image shows that the film comprises of disordered nanorods instead of closed packaged array. Study showed that the assembly mechanism can be altered by carrying out a partial ligand exchange of the thiol ligands for tetradecylphosphonic acid (TDPA) on the nanorods surface [27]. The as synthesized TDPA capped rods show less propensity for assembly. Furthermore, the addition of the TDPA ligands to pre-assembled 2D films with DDT ligands results in disassembly of the 2D films into freely dispersed rods. Therefore, a vertically aligned CdSe nanorods might be achieved by EPD with lighand exchange. The PLQY of the CdSe NRs is only 0.13% which is too low for the application in the LEDs or laser device, so there is no need to do the further research on EPD with this CdSe NRs.

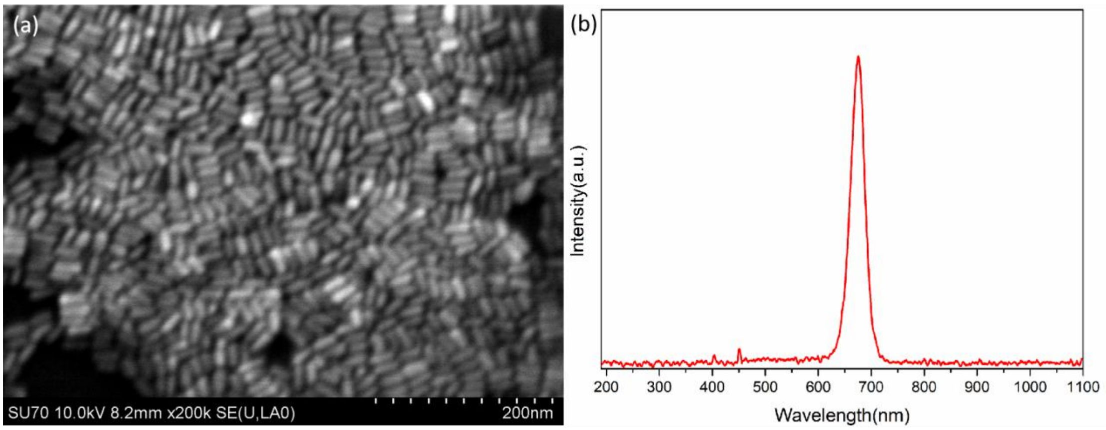

Figure 7: (a) SEM image of $CdSe_xS_{1-x}$ NRs; (b) photoluminescence spectra of $CdSe_xS_{1-x}$ NRs.

The ability to control both the composition and the aspect-ratio of $CdSe_xS_{1-x}$ system is very attractive as optical and electronic properties can be independently tuned and collectively exploited on a large scale. The photoluminescence spectra with a range from 510nm to 670 nm clearly indicates a compositional dependence for all the $CdSe_xS_{1-x}$ alloy NRs and they are independent of size [28]. The $CdSe_xS_{1-x}$ NRs was synthesized and characterized with a Se/S composition of 0.77, the SEM image shows (Figure 7(a)) that the $CdSe_xS_{1-x}$ NRs have a conventional rod shape (25 nm in length) with a narrow size distribution (FWHM=24 nm). Figure 7(b) shows the corresponding photoluminescence emission spectra of $CdSe_xS_{1-x}$ NRs with a PL peak of 674.5 nm.

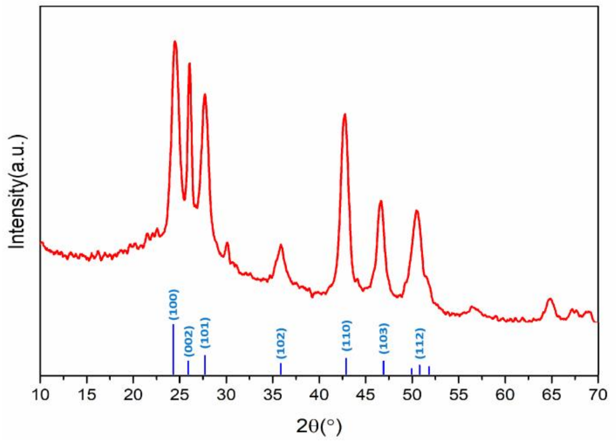

Figure 8: XRD patterns of the CdSexS1-x NRs.

Figure 8 shows the normalized X-ray diffraction (XRD) patterns of the $CdSe_xS_{1-x}$ sample. The diffraction patterns are in consistent with respective bulk wurtzite CdSeS (JCPDF 50-0720) crystals. It is clearly seen that the crystallographic phase of all the samples is in good agreement with that of the typical hexagonal wurtzite crystals. All the diffraction peaks shift toward low angles (compare with JCPDF 50-0720). The shift of the diffraction peaks could be interpreted by the enlarged interplanar spacing after incorporating bigger Se atoms [29]. If the NRs were mixtures of CdS and CdSe instead of being alloyed, the resulting XRD patterns would exhibit superposition of the patterns from the pure CdS and the pure CdSe phases. Previous study have shown the linear relationship between lattice constants and Se content indicates the successful synthesis of phase pure $CdSe_xS_{1-x}$ NRs without serious damage of the hexagonal structure [28].

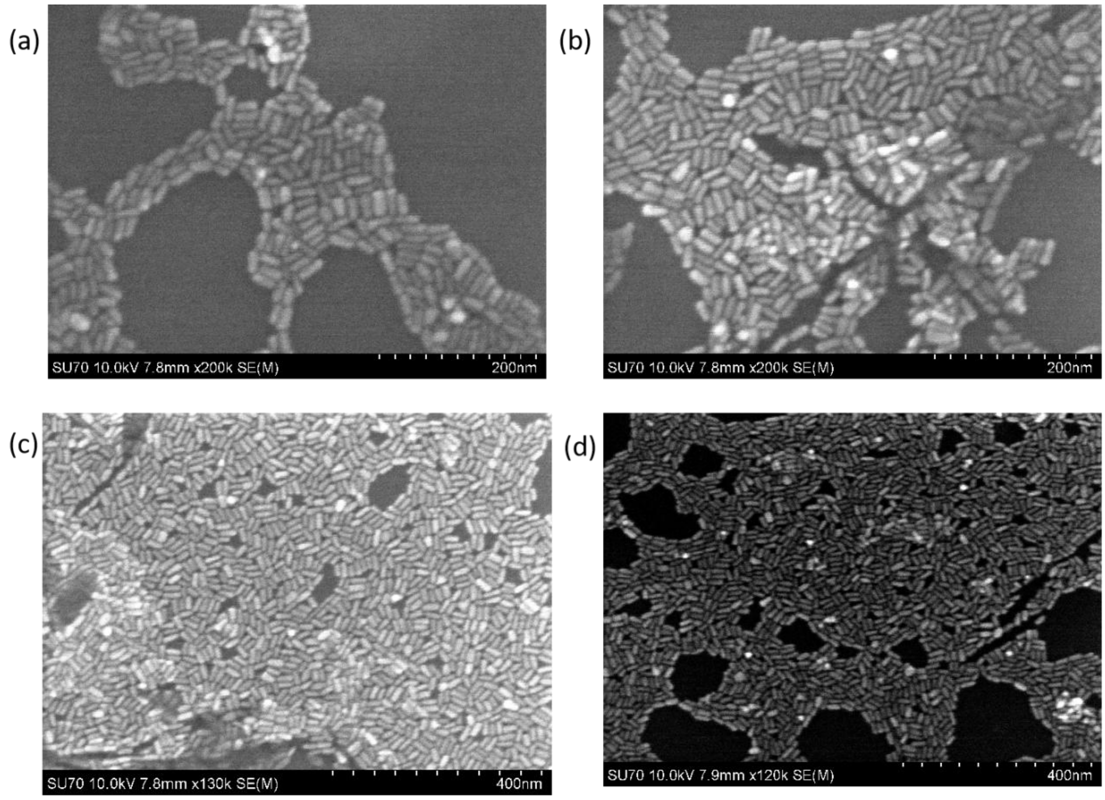

Figure 9: EPD experimental information showing: (a) CdSeS 300V 150s; (b) CdSeS 300V 300s; (c) CdSeS 500V 300s; (d) CdSeS 800V 300s;

We aim to obtain vertically aligned nanorod assemblies over several multilayers using $CdSe_xS_{1-x}$ nanorods by electrophoretic deposition. The presence of both charge and dipole on the rods allows both field driven deposition and orientational order to form close packed arrays where each rod is vertically aligned. Study showed that the ligand environment has a big influence on net charge and on assembly formation in CdSe nanorods that have long chain alkyl ligands (low charge) or pyridine ligands (high charge) [30]. Figure 9 shows the surface morphology of the $CdSe_xS_{1-x}$ NRs deposited by EPD with different deposition parameters. The $CdSe_xS_{1-x}$ NRs was washed 4 times before EPD. At 300V, the NRs is deposited on the silicon substrate with too much defects and the mono-film can not cover the substrate surface no matter how long the deposition time is. The film quality is improved by increasing the voltage to 500 V, but the micro-holes and is observed and there is only a monolayer. There are much more defects when the voltage increased to 800V. The might be because the net charge and dipole moment on nanorods has a significant influence on EPD. In the absence of external forces on a solution, the charge dipole interactions have a distance and hence concentration dependence which when optimized allows for spontaneous clustering of the rods into 2D sheets that drop to the surface under gravity sedimentation. As these interactions are Coulombic, they can be controlled by tuning the net charge through control the amount of ligand [31].

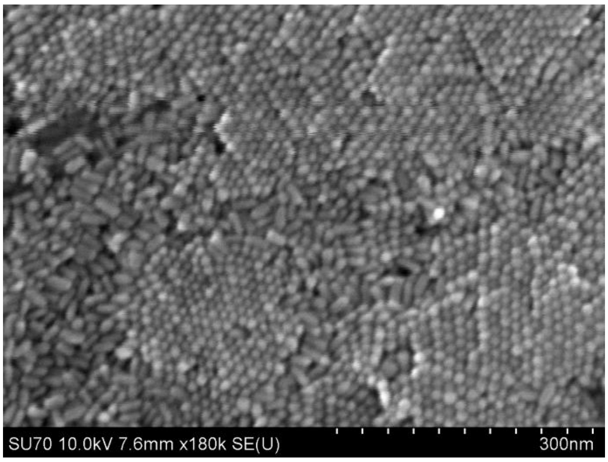

Figure 10: EPD experimental information showing: uniform layer of CdSeS nanorods obtained via EPD(Inset: scale bar is 300 nm);

There are a multitude of influential factors to be considered when nanorod assembly is investigated in solution. The physical properties of the rod such as size, shape, net charge, dipole moment, and ligand environment are significant. A low degree of polydispersity in rod length and diameter is a necessary prerequisite if close packed ordering is to be attained. While the dipole moment is inherent to the crystallographic structure (noncentrosymmetric wurtzite lattice in the case of rods), the remaining physical properties are largely controllable through repeated synthetic optimization. The presence and influence of unwanted impurities in the solvent, particularly excess surfactant, is often overlooked but can be highly detrimental to assembly formation if not controlled. Under the influence of an electric field, all these factors are equally relevant. Figure 10 is the SEM image of the $CdSe_xS_{1-x}$ NRs layer made by EPD, the $CdSe_xS_{1-x}$ NRs solution was washed 8 times before EPD. The close packaged vertically aligned NRs multilayer is obtained, and there is no microcracks or microholes in the layer. Unfortunately, it still can not be applied to the application in the LEDs as the PLQY of the $CdSe_xS_{1-x}$ is only 1.3%.

4.5 Conclusion

Colloidal nanorods, such as CdS NRs, CdSe NRs and $CdSe_xS_{1-x}$ NRs, are an important material set where electronic and optical properties are size tunable in both length and diameter and hence controllable. Organization of nanorods into assemblies at practical length scales using reproducible protocols is an promising application in wide ranging applications from photovoltaics to energy storage.

Electrophoretic deposition as a viable route to layer formation with colloidal particles is known, and has been optimized to form assemblies of nanocrystals with a high degree of order at a surface. We have shown that electrophoretic deposition is an effective route for the formation of close packed assemblies of $CdSe_xS_{1-x}$ NRs. The nanorods were organized into close packed assemblies with each rod vertically aligned extending over centimeter scale areas. It is worthy to try with EPD using CdS NRs, CdSe NRs and $CdSe_xS_{1-x}$ NRs, although the coverage of CdSe layer by EPD is not good and all the PLQY of these NRs is too low to the application in the LEDs. Their ease of assembly from solution, controllable deposition procedures and subsequent compatibility for further processing makes this route an attractive approach for integratable nanophotonics.

Reference

1. Yang, J., et al., *Formation process of CdS nanorods via solvothermal route.* Chemistry of materials, 2000. **12**(11): p. 3259-3263.
2. Yu, S.-H., et al., *Controllable synthesis of nanocrystalline CdS with different morphologies and particle sizes by a novel solvothermal process.* Journal of Materials Chemistry, 1999. **9**(6): p. 1283-1287.
3. LIU, X. and F. GUO, *PHI 5300 Instrument Manual PHI 5300 Instrument Manual, 1979.* Chemistry letters, 2004. **33**(10): p. 1284-1285.
4. Klein, J.D., et al., *Electrochemical fabrication of cadmium chalcogenide microdiode arrays.* Chemistry of materials, 1993. **5**(7): p. 902-904.
5. Dmitri, R., et al., *Electrochemical Fabrication of CdS Nanowire Arrays in Porous Anodic Aluminum Oxide Templates.* The Journal of Physical Chemistry, 1996. **100**(33): p. 14037-14047.
6. Routkevitch, D., et al., *Synthesis and resonance Raman spectroscopy of CdS nano-wire arrays.* Chemical physics, 1996. **210**(1-2): p. 343-352.
7. Li, Y.-D., et al., *Nonaqueous synthesis of CdS nanorod semiconductor.* Chemistry of materials, 1998. **10**(9): p. 2301-2303.
8. Yang, P. and C.M. Lieber, *Nanorod-superconductor composites: a pathway to materials with high critical current densities.* Science, 1996. **273**(5283): p. 1836-1840.
9. Zhang, X., et al., *Highly uniform and monodisperse Ba2ClF3 microrods: Solvothermal synthesis and characterization.* Crystal Growth and Design, 2008. **8**(12): p. 4564-4570.
10. Wu, Y., et al., *Synthesis and photovoltaic application of copper (I) sulfide nanocrystals.* Nano letters, 2008. **8**(8): p. 2551-2555.
11. Liu, L., Q. Peng, and Y. Li, *Preparation of CdSe quantum dots with full color emission based on a room temperature injection technique.* Inorganic chemistry, 2008. **47**(11): p. 5022-5028.

12. Xiong, Y., et al., *Growth and phase-transformation mechanisms of nanocrystalline CdS in Na2S solution.* The Journal of Physical Chemistry C, 2008. **112**(25): p. 9229-9233.
13. Wang, G., et al., *P123-assisted hydrothermal synthesis and characterization of rectangular parallelepiped and hexagonal prism single-crystalline MgO with three-dimensional wormholelike mesopores.* Inorganic chemistry, 2008. **47**(10): p. 4015-4022.
14. Sitt, A., I. Hadar, and U. Banin, *Band-gap engineering, optoelectronic properties and applications of colloidal heterostructured semiconductor nanorods.* Nano Today, 2013. **8**(5): p. 494-513.
15. Peng, X., et al., *Shape control of CdSe nanocrystals.* Nature, 2000. **404**(6773): p. 59-61.
16. Chen, X., et al., *Polarization spectroscopy of single CdSe quantum rods.* Physical Review B, 2001. **64**(24): p. 245304.
17. Wang, J., et al., *Highly polarized photoluminescence and photodetection from single indium phosphide nanowires.* Science, 2001. **293**(5534): p. 1455-1457.
18. Li, L.-s., et al., *Semiconductor nanorod liquid crystals.* Nano Letters, 2002. **2**(6): p. 557-560.
19. Ryan, K.M., et al., *Assembly of binary, ternary and quaternary compound semiconductor nanorods: From local to device scale ordering influenced by surface charge.* CrystEngComm, 2014. **16**(40): p. 9446-9454.
20. Li, L.-s. and A.P. Alivisatos, *Origin and scaling of the permanent dipole moment in CdSe nanorods.* Physical review letters, 2003. **90**(9): p. 097402.
21. Lee, Y.-L., C.-F. Chi, and S.-Y. Liau, *CdS/CdSe co-sensitized TiO2 photoelectrode for efficient hydrogen generation in a photoelectrochemical cell.* Chemistry of materials, 2010. **22**(3): p. 922-927.
22. Abdelhady, A.L., et al., *Flow reactor synthesis of CdSe, CdS, CdSe/CdS and CdSeS nanoparticles from single molecular precursor (s).* Journal of Materials Chemistry, 2011. **21**(46): p. 18768-18775.

23. Okamoto, S., et al., *Photoluminescence from surface-capped CdS nanocrystals by selective excitation.* Solid state communications, 1998. **105**(1): p. 7-11.
24. Tsai, C., et al., *Studies of grain size effects in rf sputtered CdS thin films.* Journal of Applied Physics, 1996. **79**(12): p. 9105-9109.
25. Thibert, A., et al., *Sequestering high-energy electrons to facilitate photocatalytic hydrogen generation in CdSe/CdS nanocrystals.* The Journal of Physical Chemistry Letters, 2011. **2**(21): p. 2688-2694.
26. Ip, A.H., et al., *Hybrid passivated colloidal quantum dot solids.* Nature nanotechnology, 2012. **7**(9): p. 577-582.
27. Liu, P., et al., *Complete assembly of Cu 2 ZnSnS 4 (CZTS) nanorods at substrate interfaces using a combination of self and directed organisation.* Chemical Communications, 2016. **52**(77): p. 11587-11590.
28. Singh, S., et al., *Colloidal synthesis of homogeneously alloyed CdSe x S 1− x nanorods with compositionally tunable photoluminescence.* Chemical Communications, 2013. **49**(87): p. 10293-10295.
29. Yang, G., et al., *Ultralong homogeneously alloyed CdSexS1-x nanowires with highly polarized and color-tunable emissions.* Advanced Optical Materials, 2014. **2**(9): p. 885-891.
30. Singh, A., N.J. English, and K.M. Ryan, *Highly ordered nanorod assemblies extending over device scale areas and in controlled multilayers by electrophoretic deposition.* The Journal of Physical Chemistry B, 2013. **117**(6): p. 1608-1615.
31. Singh, A., et al., *Directing semiconductor nanorod assembly into 1D or 2D supercrystals by altering the surface charge.* Chemical communications, 2010. **46**(38): p. 7193-7195.

5. The Synthesis and Characterization of CdSe/CdS core/shell Nanorods and Their Application in RGB LEDs

5.1 Introduction

In this chapter, we try to make red, green and blue NC-LEDs based on CdSe/CdS 'dot-in-rods' (DiRs) as an emissive layer. CdSe/CdS NRs were selected as emitters because they demonstrate high PLQY, and the emission wavelength can be tuned via the core size over a large portion of the visible range. In 2007 Carbone et al. and Talapin et al. have independently published works on high temperature seeded growth of CdSe/CdS core/shell NRs, based on a 'dot-in-a-rod' structure, with easily controllable aspect ratio and high fluorescence QY [1]. Also, CdSe/CdS core shell nanorod (NR) semiconductor is an promising NC for the application of LEDs because of their tunable emission wavelengths similar to quantum dots (QDs), linearly polarized emission [2] and a larger Stokes shift, faster radiative decay and slower bleaching kinetics than QDs [3].

The unique synthetic control and photophysical properties of CdSe/CdS nanoheterostructures make them workhorses of nanoscale science. Starting from quasi-spherical quantum dots (QDs), CdSe/CdS core/shell structures grow in several morphologies, including anisotropic nanorods [4]. Seeded growth heterostructures have been used to study new synthetic techniques [5] [1], assembly [6], energy-transfer and band structure [7] [8] [9], lasing and gain [10] [11] [12], exciton fine structure [13], blinking [14], spin [15], and polarized optical properties [16]. Exploitation of NR heterostructures in light emitting devices across a wide spectral range is contingent on understanding the relationship between microscopic structure and physical properties.

Since the first introduction of quantum-dot LEDs (QLEDs), great progress has been made over the past few years due to the rapid development of QD materials and device architectures [17]. However, even though the materials and the devices have been improved greatly, the performances such as the efficiency and the lifetime of QLEDs are still lower than those of their competitors: organic LEDs (OLEDs). For example, external quantum efficiencies (EQEs) > 20% have been routinely reported in OLEDs [18], whereas it is still rarely reported in QLEDs. Particularly, the efficiency and the lifetime of blue and green QLEDs are significantly lower than those of their OLED counterpart, which is a big concern for their future commercialization [19]. Apart from the detailed QLED architecture and processing, the NC material itself strongly affects the device performance.

The highest EQE observed from red device is usually attributable to the desirable energetic alignment between the valence band level of NC versus the highest occupied molecular orbital (HOMO) level of HTL. Specifically, the smallest band offset at NC/HTL interface is attainable from the smaller-band gap red NC compared to blue and green QDs, leading to a better hole injection and charge balance [20]. A generally lower PLQY of blue and green NCs would naturally lead to poor device performance. One convincing reason for not realizing a blue NC-LED would be associated with the difficulty in securing a blue and green NC emitter efficient enough to be applied for device fabrication, although the NC structural engineering such as the formation of alloyed core/shell interface and/or thick shell can prove beneficial in substantially improving the device performance by suppressing nonradiative Auger recombination and/or inter-NC Forster energy transfer [21] [22] [22].

To create a blue and green emission from NCs, their size that is placed in a strong quantum confinement regime should be significantly small. Thereby, its PL may be inevitably inefficient due to the small NC size-related incorrigible problems, e.g., the presence of high density of surface state and the unlikeliness of complete surface passivation of the core. Therefore, realistically, the demonstration of high-efficiency, full-color-affordable NC-LEDs seems implausible for the present. In this work, we use EPD with CdSe/CdS NRs for the fabrication of the LED, which can improve the charge balance and reduce the resistance and in turn improve the device efficiency.

5.2 Experiments

5.2.1 Chemicals

All reagents were used as received without any further purification. Cadmium oxide (> 99 %), trioctylphosphine (TOP, 97 %), trioctylphosphine oxide (TOPO, 99 %), selenium (99.98 %) and sulfur (99 %) were purchased from Sigma-Aldrich, Tetradecylphosphonic acid (TDPA, > 99 %) and n-hexylphosphonic acid (HPA, > 99 %) were obtained from Aladdin. Silicon wafers were purchased from Si-Mat and University Wafer. N-type phosphorus doped silicon wafers were purchased from Si-Mat. Poly(9-vinylcarbazole)(PVK) were purchased from Sigma Aldrich. Patterned ITO-glass substrates (sheet resistance, 20 Ω·sq−1) were purchased from Xinxiang Ltd. The $Zn_{1-x}Mg_xO$ nanoparticles was purchased from PLANCK Ltd.

5.2.2 Synthesis of Cadmium Selenium core

The CdSe cores were prepared by following the procedures reported by Carbone et . 0.06 g CdO, 0.28 g ODPA and 3.0 g TOPO were mixed in a three-neck flask, Under the protection of argon, heated to 150 ºC and exposed to vacuum for 1 hour. Then, under argon flow, the mixture was heated to above 300ºC to dissolve the CdO until it turned optically clear and colorless. At this point, 1.5 g of TOP was injected into the flask and the temperature was allowed to recover to the value required for the injection of the Se-TOP solution (0.058 g Se + 0.360 g TOP). CdSe quantum dots could be synthesized by injecting the Se-TOP at 370ºC and then stop the reaction after only 10-60 seconds. The final solution was precipitated by centrifuging and then redispersion in TOP.

5.2.3 Synthesis of Cadmium Selenium / Cadmium Sulphide Core/Shell Nanorods

The growth of CdSe/CdS core/shell nanorods: 3.0 g TOPO, 290 mg ODPA, 90 mg HPA, and 90 mg of CdO were introduced in another three-neck flask and degassed at 150°C for 1 hour. The solution was then heated up to 320°C under nitrogen, and 1.5 mL TOP was injected into the mixture. In a separate vial, 100 nmol of the CdSe cores were concentrated and mixed with 120 mg of S, and the solids were dissolved in 2 mL of TOP at ~80°C. Finally, the CdSe/S-TOP solution was rapidly injected into the former solution containing CdO and the reaction was allowed to proceed for 8 min, and then cooled down to room temperature. The nanorods were precipitated using a mixture of ethanol and toluene and then re-dispersed in toluene.

5.2.4 Device Fabrication

A patterned ITO glass substrate was cleaned with DI water, acetone and IPA in the sonicator, and then UV-ozone treated for 5 min. The hole injection layer (HIL) of PEDOT:PSS was spin-coated at 3000 rpm for 45 s, and then baked at 150 °C for 30 min. The HTL, PVK solution with a concentration of 8 mg in chlorobenzene, was spin coated on the PEDOT layer. With a NRs dispersion in toluene with a concentration of ~ 25 mg/mL, was spin-deposited on the ITO/PEDOT/PVK substrate at 3000 rpm for 30 s. A transparent ethanol solution of $Zn_{1-x}Mg_xO$ NPs with a concentration of ~ 30 mg/mL was consecutively spin-coated at 3000 rpm for 30 s, followed by the baking at 120 °C for 10 min on the NRs layer. Finally, a 40 nm thick Al cathode was thermally evaporated on top of ETL, the fabrication was carried out in a glovebox with a structure of ITO/PEDOT:PSS/PVK/NRs/$Zn_{1-x}Mg_xO$/Al.

5.3 Results and Discussion

The CdSe/CdS core-shell nanorods synthesized by seeded-type growth approach show narrow distributions of rod lengths and diameters. The CdSe/CdS nanorods present appealing characteristics of strong and tunable light emission from green to red. The synthesis is based on the co-injection of appropriate precursors and preformed spherical CdSe nanocrystal seeds (nearly monodisperse in size) in a reaction flask that contains a mixture of hot surfactants suited for the anisotropic growth of CdS nanocrystals. The synthesis is rather flexible, as there are various parameters that can be tuned in order to control the morphology of the resulting nanorods such as the diameter of the seeds, the growth temperature, and the amount of precursors and seeds added.

Figure 1 CdSe quantum dots solution

Under the ambient light, the synthesized CdSe quantum dots show colorless to red orange. Under the irradiation of the short wave ultraviolet lamp (420 nm), the colorless sample emits light from blue to green, and the colors of yellow, orange and red quantum dots are more obvious, as shown in Figure 1. The color of luminescence varies with the reaction time. This color change indicates that the quantum dots are different in size.

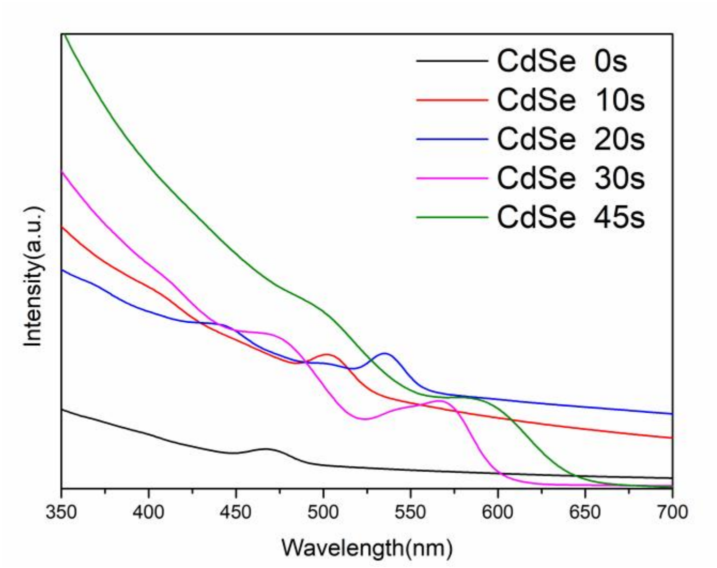

Figure 2: Absorption spectrum of the CdSe QDs sample synthesized in different reaction time.

Peaks in the absorption spectra exhibit a similar size-dependent shift, as shown in Figure 2. Nevertheless, the widths of absorption spectra are approximately 140 nm, indicating a reasonable size distribution within each sample of various reaction times.

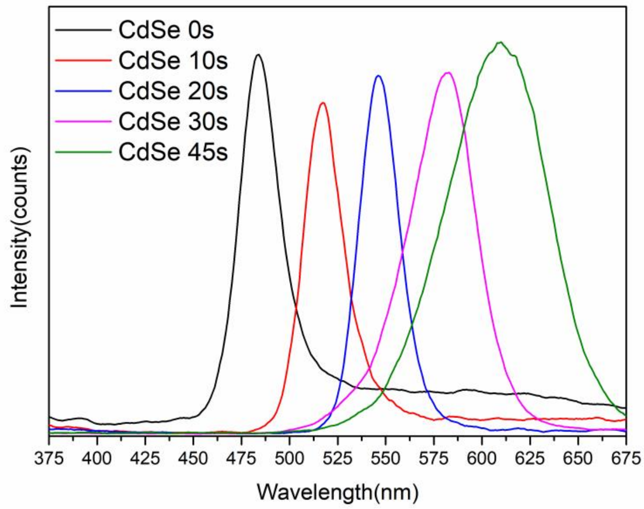

Figure 3. Normalized emission spectrum of CdSe QDs obtained by different reaction times with a 405 nm excitation wavelength. The change of the peak position demonstrates the growing of the QDs.

The luminescence of CdSe quantum dots synthesized with different reaction times is mainly determined by exciton emission. As shown in Figure 3, compared with the exciton emission spectrum synthesized with a longer reaction time, for the short reaction times, the peak value of the exciton emission spectrum is narrower. As the reaction time increased, the peak position shifted towards the longer wavelength (from 482 nm to 615 nm). This is consistent with the particle-in-a-box model [23], which states that the larger the box, the smaller the energy gap between adjacent energy levels [24]. As a result, larger quantum dots emit longer wavelengths as their size increases. The appearance of a narrow peak at 482 nm and a half-wide peak with a width of 21 nm indicate the formation of small and uniform quantum dots in a short time. Moreover, in the emission spectrum, these peak locations are at shorter wavelengths.

The comparison of emission spectra (Figure 3) and absorption spectra (Figure 2) of CdSe quantum dots illustrates the Stokes shift. Previous studies on the origin of the Stokes shift in CdSe quantum dots indicate that the electron hole exchange interaction leads to the splitting of the activated exciton state [25]. When excited, the electron is lifted to the higher of the two excited states, and decays to the lower of the excited state without radiation. Then when they relax to the ground state and combine with the hole, they emit a photon (luminescence). Moreover, Figure 2 and Figure 3 show the energy difference between the first exciton absorption peaks of core as a function of the core diameter. A larger spectral red shift is observed for structures having smaller cores.

Table 1 The summaries of the optical properties of CdSe core

NO.	Name	Time	PLQY(%)	UV (nm)	Absorption (a.u.)	PL(nm)	FWHM (nm)	Radius (nm)
1	CdSe core	0s	0.2%	467nm	0.105	482nm	29nm	2.07nm
2	CdSe core	10s	1.4%	502nm	0.354	525nm	23nm	2.36nm
3	CdSe core	20s	1.8%	535nm	0.357	557nm	27nm	2.77nm
4	CdSe core	30s	1.2%	566nm	0.231	578nm	29nm	3.40nm
5	CdSe core	40s	1.5%	594.9nm	0.226	615nm	31nm	4.36nm

There are many methods to evaluate the size of CdSe quantum dots. On the basis of the absorption spectrum, Gaussian function is used to fit the normalized and background subtracted absorption spectra, and the peak position λ (nm) is determined. According to the empirical equation of Mulvaney and colleagues [26], the diameter d (nm) of the quantum dot is calculated. The diameter of the quantum dots synthesized in 0~45 s reaction time is estimated to be between 2.07~4.36 nm as shown in table 1. It should be noted that these values are the average of quantum dots of different sizes in each sample, rather than representing single size quantum dots. The size distribution determines the width of the absorption and emission spectra. Therefore, when studying size dependent properties and particle models (more accurately, particle models in the sphere of three-dimensional quantum dots), articles often focus on the inspection of emission spectra [27]. However, it is worth noting that this model uses the separate effective masses of electrons and holes as an approximation and is only applicable to larger quantum dots [28] [29]. With the decrease of QD size, the deviation between the calculated size and the measured value becomes more and more significant [30]. Or, the empirical correlation between quantum dot size and emission peak position has been established experimentally [31]. The diameter of the quantum dot calculated from the emission maximum is 2.07 nm when the reaction time is 0 s (0 s means the reaction stops as soon as the injection is finished) and 4.36 nm when the reaction time is 45 s.

Substitution of various ligands on the surface of QDs has been shown to modulate the relative contribution of the exciton emission and the trap-state emission to the total luminescence [32] [33]. Capping the QDs with a second layer of different materials, namely, core − shell QDs, is another way to suppress the trap-state emission [34] [35].

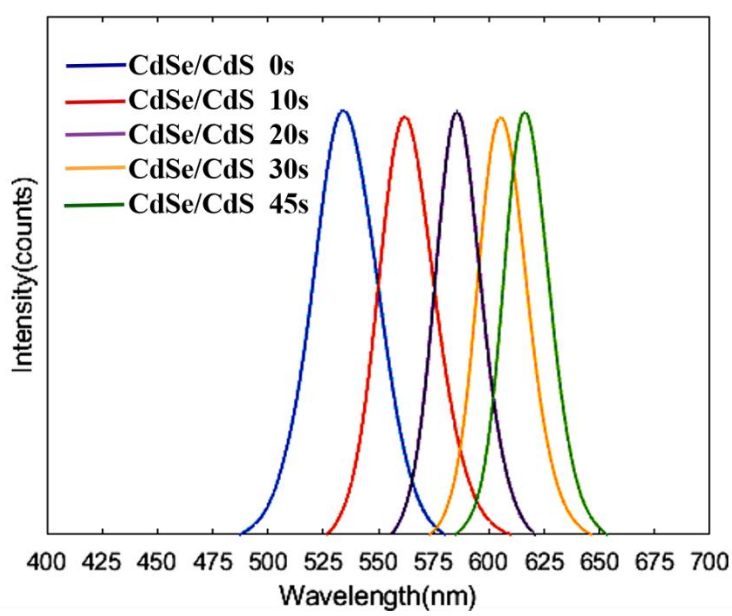

Figure 4: Photoluminescence spectra of seeded-growth CdSe/CdS core/shell nanorods made from different CdSe seeds with the corresponding color.

In order to improve the PLQY of NCs, we prepared the ordered superstructure of CdSe/CdS core/shell nanorods. These nanorods consist of a spherical CdSe core and CdS rods epitaxial grown on the {001} plane of the CdSe core (see the analysis in Figure 5 and Figure 6). The photoluminescence spectra of a series of samples in which either the core diameter (with the rod diameter being roughly the same) or the rod diameter (with the core being the same) has been independently changed, are reported in Figure 3 and Figure 4. By changing the synthetic conditions, we varied the core diameter, whereas the rod diameter was independently tuned. The small conduction band offset allows the electron-hole wave function overlap to be engineered by properly tailoring the core and rod diameter [13]. This strongly affects the optical properties of these nanostructures, as demonstrated in Figure 4.

The passivation of spherical CdSe core and elongated CdS shell produces efficient band gap photoluminescence, which is linearly polarized along the nanorods. The PL quantum efficiency of CdSe/CdS nanorods at room temperature is 2 orders of magnitude higher than that of the bare CdSe nanorods [5]. The CdSe/CdS heterostructure nanorods emit light in the spectral region, and only the CdSe nuclear energy reabsorbes the emitted light. The extinction coefficient of this spectral region is relatively small. This means that the reabsorption in CdSe/CdS heterostructure nanorod solids is much smaller than that in CdSe or any other single-phase nanorod solids [36]. This makes CdSe/CdS nanorods particularly interesting in solid-state light-emitting applications, such as phosphors, light-emitting diodes and lasers, as well as detector and light collection applications. The performance of the nanorod based hybrid solar cell [37] can be significantly improved by aligning and combining the shell of the organic cover shell ligand with the nanorod perpendicular to the substrate.

The thickness of the CdS shell is known to influence the photophysical properties of CdSe/CdS nanostructures, including quantum yield, lifetime, and blinking [38] [14]. Although CdSe/CdS dot-in-plate structures have shown large splitting of the exciton fine structure states which explains band-edge polarization properties [39], Raino et al. demonstrated that splitting of exciton fine structure states is much smaller in dot-in-rod structures compared to QDs [13]. This means the emission wavelength of the CdSe/CdS NRs can be tuned more fine than the QDs. Then the green (CdSe/CdS-0 s) and red (CdSe/CdS-45 s) NRs will be applied to the LEDs.

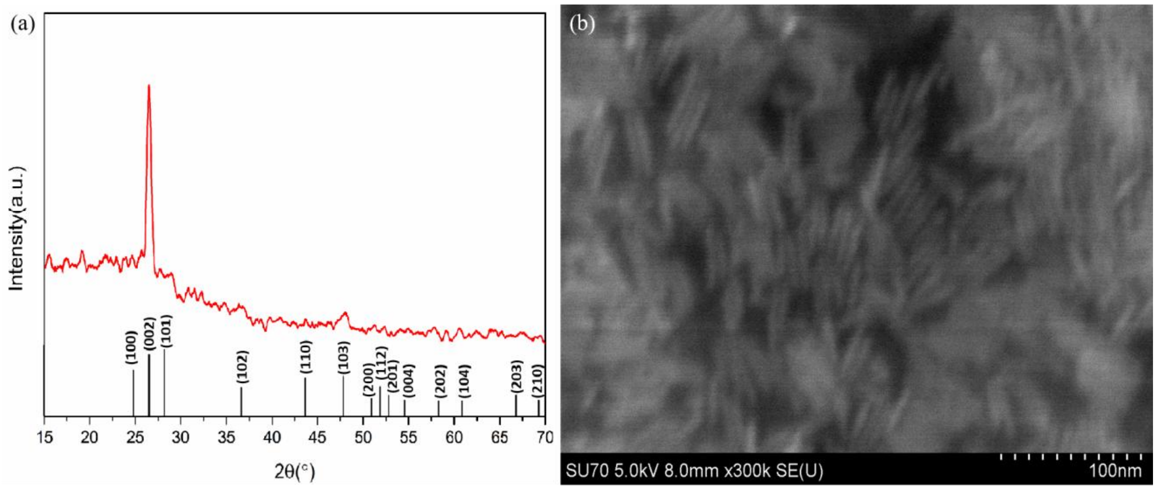

Figure 5 The XRD pattern (a) and SEM image (b) of green CdSe/CdS nanorods

Powder X-ray diffraction patterns (Figure 5(a) acquired from the XRD characterization shows a lower crystallinity, only one sharp peak is observed on the {002} plane. The SEM image of the green CdSe/CdS NRs is shown in Figure 5(b). Based on the statistical analysis of a large number of nanorods from SEM images, we could tell that the CdSe/CdS colloidal solutions are composed of monodispersed wurtzite nanorods with an average length of ~ 65 nm and a diameter of ~ 2.4 nm (according to the empirical equation calculated by Mulvaney). Compared with the diameter of the CdSe cores, this result means that near 3-4 monolayers of CdS were grown over the side surface of the CdSe/CdS NRs.

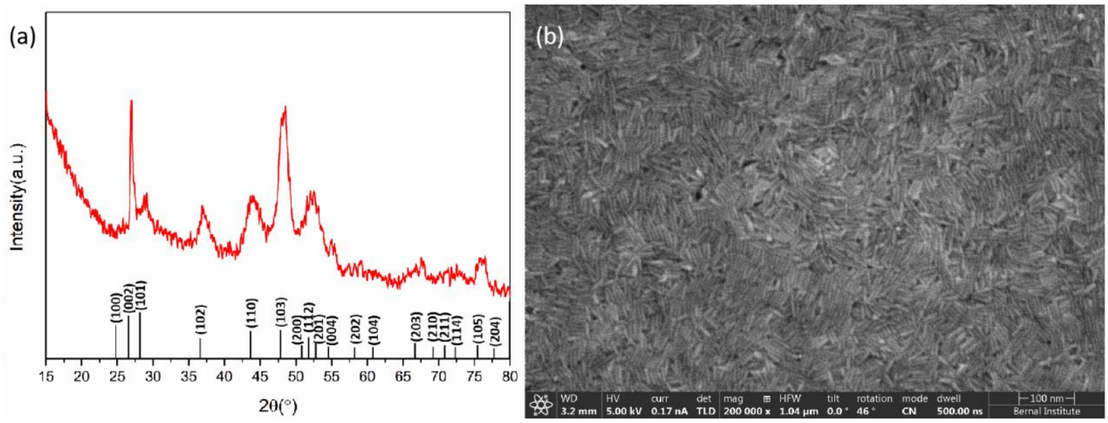

Figure 6 The XRD pattern (a) and SEM image (b) of red CdSe/CdS nanorods

The wide-angle X-ray diffraction (XRD) pattern of red CdSe/CdS nanorods (Figure 6 (a)) shows six major reflections at 2θ = 26.5°, 28.1°, 36.1°, 43.7°, 47.2° and 51.8°, which can be assigned to the 002, 101, 102, 110, 103 and 112 reflections, respectively, of cadmium chalcogenide (CdSe) with a hexagonal close-packing structure. This further prove the wurtzite structure of red CdSe/CdS NRs.

Scanning electron microscopy image (Figure 5(b)) demonstrates the morphologies of the resulting gels dried from toluene by evaporation at ambient conditions (xerogels). It can be observed that the CdSe/CdS were homogeneously grown rod-shaped nanoparticles (NPs) with lengths of 36 ± 3 nm and diameters of 5 ± 1 nm. The diameter increase of NRs from the CdSe core(CdSe-45s, 4.36 nm) is due to the epitaxial shell growth on the side surface of red NRs, which is around 8-10 monolayers were grown onto the cores, due to the higher reactivity and lower interfacial strain of the facet along the C axis [5].

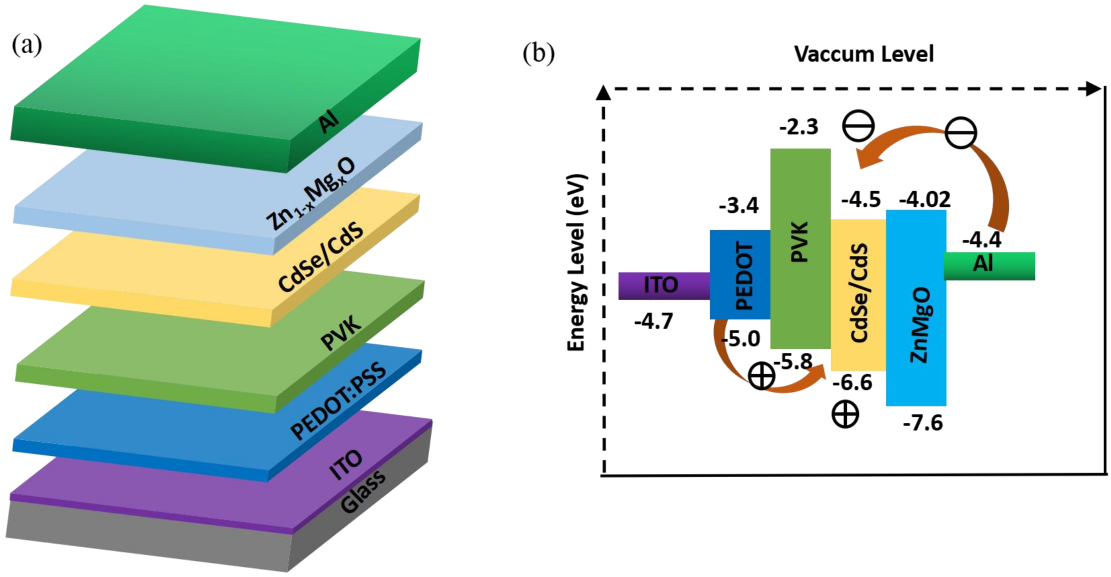

Figure 7 (a) Schematic structure illustration of the multilayered NR-LEDs. (b) Energy level diagram of the multilayered NR-LEDs.

Two kinds of NRs (Green-NRs and Red-NRs) are applied to the fabrication of NR-LEDs. The multilayer structure of NR-LED is fixed as shown in Figure 7 (a), which is composed of ITO (~100 nm) and PEDOT: PSS/PVK/NRs/$Zn_{1-x}Mg_xO$/Al (40 nm). Except that the aluminum cathode is deposited by thermal vacuum, all other layers are spin coated on the transparent anodes ITO substrate with a certain pattern. Figure 7 (b) shows the flat band energy level diagram of different layers of NR-LED. The energy level values are taken from the published reports [40] [41] [42]. The thickness of PEDOT:PSS, PVK, emission NRs layer and $Zn_{1-x}Mg_xO$ layer is around 45 nm, 40 nm, 40 nm and 40 nm respectively.

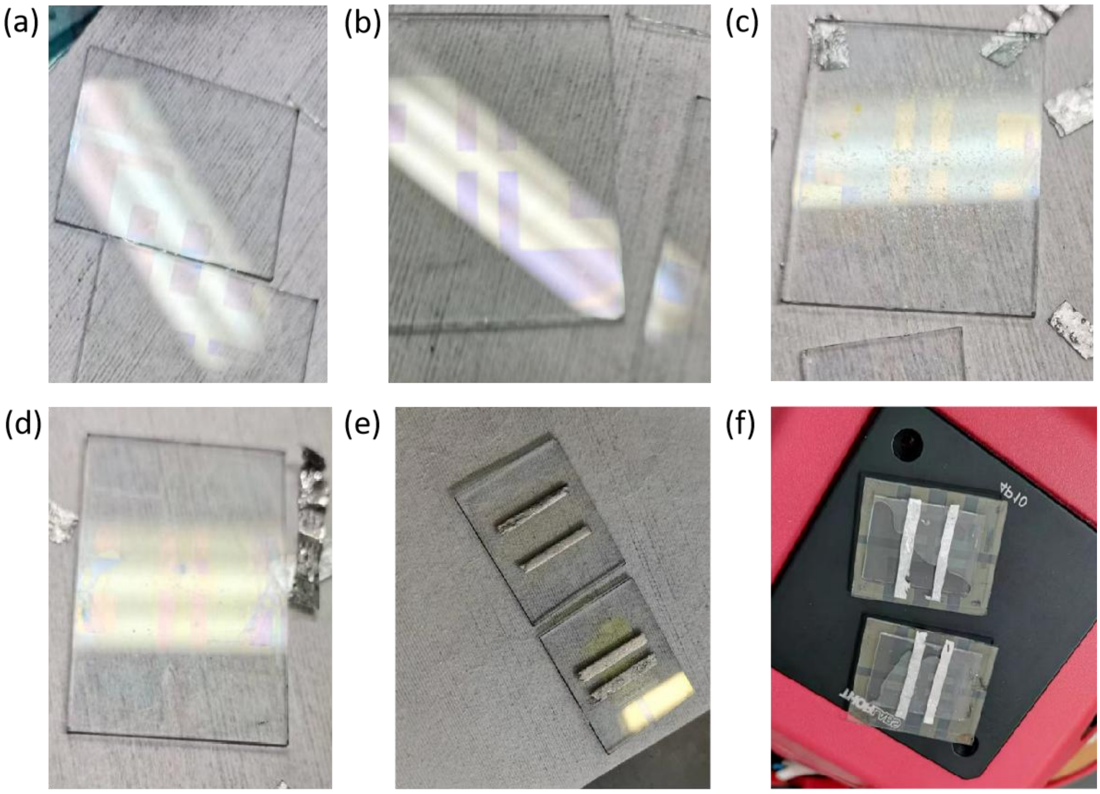

Figure 8 Device preparation process (a): PEDOT:PSS layer; (b): PVK layer; (c): NRs layer; (d): $Zn_{1-x}Mg_xO$ layer; (e): device with electrode (liquid metal); (f): packaged devices.

Figure 8 shows the whole process of device fabrication. PEDOT:PSS was spin coated on the ITO glass washed by water, aceton and ethanol, the ITO/PEDOT:PSS substrate (Figure 8(a)) shows a transparent and uniform film after heat treatment at 135 ℃ for 15 min. Next, the PVK layer was spin coated on the ITO/PEDOT:PSS substrate followed by heat treatment at 120 ℃ for 10 min in the glovebox (Figure 8(b)). Then the CdSe/CdS NRs served as emission layer were deposited by spin coating, with a concentration of 15 mg/ml (Figure 8(c)). The $Zn_{1-x}Mg_xO$ as the HTL was spin-coated in the glovebox (Figure 8(d)). After heat treatment under 120 ℃ for 10 min, the liquid metal strips were placed on the surface of the as-prepared sample for the installation of electrodes. The final device is shown in Figure 8(e). At last, the LEDs were packaged with the glass and UV-glue for the isolation of the oxygen and moisture (Figure 8(f)).

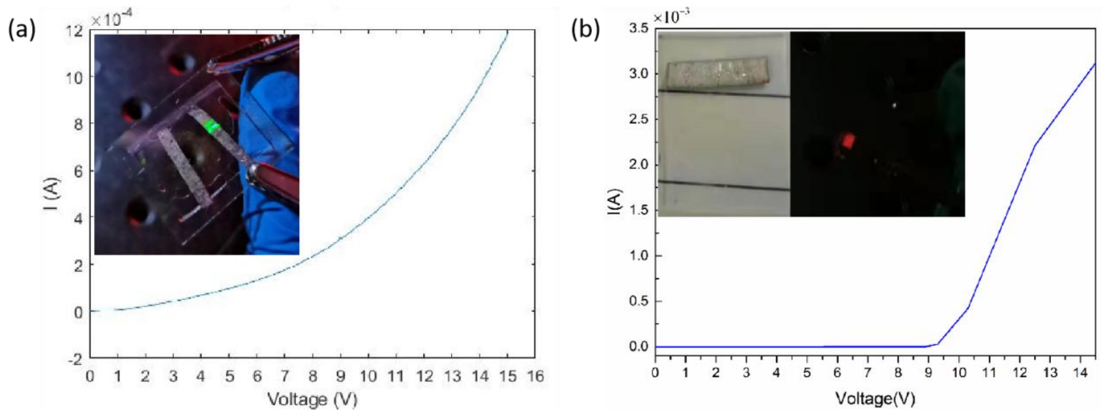

Figure 9(a) The variations of current with increasing applied voltage for green (a) and red (b) device.

The low current density observed from red-NRs based device indicates that the presence of a thicker shell as a non negligible energy barrier may more hinder charge injection into the emission layer, resulting in a decrease in the volume current [21]. Red-LED shows a lower leakage currents results in a better device efficiency than that of the Green one. The maximum EQE of the devices are 0.041 % and 0.0003 % for the green and red device respectively. Next we will use the thermal evaporator for the Al deposition as the cathode.

5.4 Conclusion

If cadmium acetate, a less harmful dihydrate, can replace cadmium oxide, it will be a considerable improvement. If cadmium oxide is lethal by inhalation, while cadmium acetate is toxic, but not fatal [43]. Cadmium oxide is a powder, not a crystal form of cadmium acetate dihydrate, so its inhalation hazard is greater. In addition, the existence of water and oxygen has been proved to affect the optical properties of CdSe quantum dots [44], and these factors are also used to help form CdSe nanocrystals [45]. Therefore, the growth of nanocrystals exposed to air is not as well controlled as that under inert conditions. The size, shape and surface composition of the final product may be more complex. The synthesis of the blue CdSe/CdS NRs should be further studied in the future, the device efficiency of the red and green

NR-LEDs can be improved by using EPD for the deposition and ligand exchange of CdSe/CdS layer.

Reference

1. Carbone, L., et al., *Synthesis and micrometer-scale assembly of colloidal CdSe/CdS nanorods prepared by a seeded growth approach.* Nano letters, 2007. **7**(10): p. 2942-2950.
2. Hu, J., et al., *Linearly polarized emission from colloidal semiconductor quantum rods.* Science, 2001. **292**(5524): p. 2060-2063.
3. Shabaev, A. and A.L. Efros, *1D exciton spectroscopy of semiconductor nanorods.* Nano letters, 2004. **4**(10): p. 1821-1825.
4. Talapin, D.V., et al., *Seeded growth of highly luminescent CdSe/CdS nanoheterostructures with rod and tetrapod morphologies.* Nano letters, 2007. **7**(10): p. 2951-2959.
5. Talapin, D.V., et al., *Highly emissive colloidal CdSe/CdS heterostructures of mixed dimensionality.* Nano Letters, 2003. **3**(12): p. 1677-1681.
6. Pietra, F., et al., *Semiconductor nanorod self-assembly at the liquid/air interface studied by in situ GISAXS and ex situ TEM.* Nano letters, 2012. **12**(11): p. 5515-5523.
7. Steiner, D., et al., *Determination of band offsets in heterostructured colloidal nanorods using scanning tunneling spectroscopy.* Nano letters, 2008. **8**(9): p. 2954-2958.
8. Sitt, A., et al., *Multiexciton engineering in seeded core/shell nanorods: transfer from type-I to quasi-type-II regimes.* Nano letters, 2009. **9**(10): p. 3470-3476.
9. Rainò, G., et al., *Probing the wave function delocalization in CdSe/CdS dot-in-rod nanocrystals by time-and temperature-resolved spectroscopy.* ACS nano, 2011. **5**(5): p. 4031-4036.
10. Krahne, R., et al., *Amplified spontaneous emission from core and shell transitions in CdSe/CdS nanorods fabricated by seeded growth.* Applied Physics Letters, 2011. **98**(6): p. 063105.

11. Liao, Y., et al., *Low Threshold, Amplified Spontaneous Emission from Core-Seeded Semiconductor Nanotetrapods Incorporated into a Sol–Gel Matrix.* Advanced Materials, 2012. **24**(23): p. OP159-OP164.
12. Xing, G., et al., *Ultralow-threshold two-photon pumped amplified spontaneous emission and lasing from seeded CdSe/CdS nanorod heterostructures.* Acs Nano, 2012. **6**(12): p. 10835-10844.
13. Rainò, G., et al., *Controlling the exciton fine structure splitting in CdSe/CdS dot-in-rod nanojunctions.* ACS nano, 2012. **6**(3): p. 1979-1987.
14. Pisanello, F., et al., *Non-blinking single-photon generation with anisotropic colloidal nanocrystals: towards room-temperature, efficient, colloidal quantum sources.* Advanced Materials, 2013. **25**(14): p. 1974-1980.
15. van Schooten, K.J., et al., *Spin-Dependent Exciton Quenching and Spin Coherence in CdSe/CdS Nanocrystals.* Nano letters, 2013. **13**(1): p. 65-71.
16. Sitt, A., et al., *Highly emissive nano rod-in-rod heterostructures with strong linear polarization.* Nano letters, 2011. **11**(5): p. 2054-2060.
17. Dai, X., et al., *Solution-processed, high-performance light-emitting diodes based on quantum dots.* Nature, 2014. **515**(7525): p. 96-99.
18. Kim, K.H., et al., *Highly efficient organic light-emitting diodes with phosphorescent emitters having high quantum yield and horizontal orientation of transition dipole moments.* Advanced Materials, 2014. **26**(23): p. 3844-3847.
19. Lee, C., et al. *13-1: Invited Paper: White Quantum Dot Light-Emitting Diodes With Improved Efficiency and Color Stability*. in *SID Symposium Digest of Technical Papers*. 2017. Wiley Online Library.
20. Shen, H., et al., *High-efficient deep-blue light-emitting diodes by using high quality ZnxCd1-xS/ZnS core/shell quantum dots.* Advanced Functional Materials, 2014. **24**(16): p. 2367-2373.
21. Lee, K.-H., et al., *Highly efficient, color-pure, color-stable blue quantum dot light-emitting devices.* ACS nano, 2013. **7**(8): p. 7295-7302.

22. Lee, K.-H., et al., *Over 40 cd/A efficient green quantum dot electroluminescent device comprising uniquely large-sized quantum dots.* ACS nano, 2014. **8**(5): p. 4893-4901.

23. Rice, C.V. and G.A. Giffin, *Quantum dots in a polymer composite: a convenient particle-in-a-box laboratory experiment.* Journal of chemical education, 2008. **85**(6): p. 842.

24. Landry, M.L., et al., *Simple syntheses of CdSe quantum dots.* Journal of Chemical Education, 2014. **91**(2): p. 274-279.

25. Nirmal, M. and L. Brus, *Luminescence photophysics in semiconductor nanocrystals.* Accounts of chemical research, 1999. **32**(5): p. 407-414.

26. Jasieniak, J., et al., *Re-examination of the size-dependent absorption properties of CdSe quantum dots.* The Journal of Physical Chemistry C, 2009. **113**(45): p. 19468-19474.

27. Winkler, L., et al., *Quantum dots: an experiment for physical or materials chemistry.* Journal of chemical education, 2005. **82**(11): p. 1700.

28. Bawendi, M.G., M.L. Steigerwald, and L.E. Brus, *The quantum mechanics of larger semiconductor clusters ("quantum dots").* Annu. Rev. Phys. Chem, 1990. **41**(1): p. 477-496.

29. Kippeny, T., L.A. Swafford, and S.J. Rosenthal, *Semiconductor nanocrystals: a powerful visual aid for introducing the particle in a box.* Journal of chemical education, 2002. **79**(9): p. 1094.

30. Murray, C., D.J. Norris, and M.G. Bawendi, *Synthesis and characterization of nearly monodisperse CdE (E= sulfur, selenium, tellurium) semiconductor nanocrystallites.* Journal of the American Chemical Society, 1993. **115**(19): p. 8706-8715.

31. Qu, L. and X. Peng, *Control of photoluminescence properties of CdSe nanocrystals in growth.* Journal of the American Chemical Society, 2002. **124**(9): p. 2049-2055.

32. Kalyuzhny, G. and R.W. Murray, *Ligand effects on optical properties of CdSe nanocrystals.* The Journal of Physical Chemistry B, 2005. **109**(15): p. 7012-7021.
33. Landes, C.F., M. Braun, and M.A. El-Sayed, *On the nanoparticle to molecular size transition: fluorescence quenching studies.* The Journal of Physical Chemistry B, 2001. **105**(43): p. 10554-10558.
34. Kortan, A., et al., *Nucleation and growth of CdSe on ZnS quantum crystallite seeds, and vice versa, in inverse micelle media.* Journal of the American Chemical Society, 1990. **112**(4): p. 1327-1332.
35. Hines, M.A. and P. Guyot-Sionnest, *Synthesis and characterization of strongly luminescing ZnS-capped CdSe nanocrystals.* The Journal of Physical Chemistry, 1996. **100**(2): p. 468-471.
36. Talapin, D.V., et al., *CdSe and CdSe/CdS nanorod solids.* Journal of the American Chemical Society, 2004. **126**(40): p. 12984-12988.
37. Huynh, W., *WU; Dittmer, J.; Alivisatos, AP.* Science, 2002. **295**: p. 2425.
38. She, C., et al., *Using shape to control photoluminescence from CdSe/CdS core/shell nanorods.* The Journal of Physical Chemistry Letters, 2011. **2**(12): p. 1469-1475.
39. Cassette, E., et al., *Colloidal CdSe/CdS dot-in-plate nanocrystals with 2D-polarized emission.* ACS nano, 2012. **6**(8): p. 6741-6750.
40. Shen, H., et al., *High-efficiency, low turn-on voltage blue-violet quantum-dot-based light-emitting diodes.* Nano letters, 2015. **15**(2): p. 1211-1216.
41. Tan, Z., et al., *Bright and color-saturated emission from blue light-emitting diodes based on solution-processed colloidal nanocrystal quantum dots.* Nano letters, 2007. **7**(12): p. 3803-3807.
42. Mashford, B.S., et al., *High-efficiency quantum-dot light-emitting devices with enhanced charge injection.* Nature photonics, 2013. **7**(5): p. 407-412.
43. Sigma-Aldrich, C., *Material Safety Data Sheet.* Skin, 1910: p. 1000.

44. Nazzal, A.Y., et al., *Environmental effects on photoluminescence of highly luminescent CdSe and CdSe/ZnS core/shell nanocrystals in polymer thin films.* The Journal of Physical Chemistry B, 2004. **108**(18): p. 5507-5515.

45. Li, R., et al., *Amine-assisted facetted etching of CdSe nanocrystals.* Journal of the American Chemical Society, 2005. **127**(8): p. 2524-2532.

6. Future Work

To date, red quantum dot light emitting diodes have achieved a maximum external quantum efficiency of 30.9% [1], an impressive EQE of more than 22.9% was reported for green NC-LEDs with Se throughout the core/shell region, which is comparable with those of the state-of-the-art phosphorescent OLEDs [2]. However, compared with red and green NC-LEDs, the operation lifetime of blue NC-LEDs still remains poor. This is the main obstacle for the commercialization of II – VI semiconductor nanocrystals. High-quality blue NCs is one of the key factors that can eventually determine the efficiency and stability of devices. An inorganic shell can be used to passivate the surface defects of blue NCs to improve the PLQY of the blue NCs. In addition, ligand modification is another main method to decrease the fluorescence quenching and non-radiative recombination.

In this work, the synthesis of blue NRs has been widely carried out but not success yet. Because their size is placed in a strong quantum confinement regime which should be significantly small, this is difficult to control in the synthesis and the growth of the NCs.

6.1 Blue-Emitting Perovskite ($CsPbX_3$; X = Cl, Br, I) Nanorods

Light-emitting perovskite nanocrystals have recently emerged as the most efficient energy material for lighting and have been extensively studied for the past few years [3] [4] [5], owing to their long carrier lifetimes, large absorption cross sections, near-unity photoluminescence quantum yields (PLQYs), and PL color tunability over the whole visible spectrum [6]. Report of perovskite nanorods was established for energy applications [7], the monodisperse and optically stable nanocrystals are synthesized, and these would facilitate patterning as well as obtaining the stable emission [8].

6.2 Chemicals and Synthesis

Cs_2CO_3 was obtained from J&K Chemicals. Oleic acid (OA, 90%), 1-octadecene (ODE, 90%) and $CdBr_2$ (ultra dry, 99.999%) were purchased from Alfa Aesar. Oleylamine (OLA, 80-90%) and $PbBr_2$ (99.999%) were purchased from Aladdin. All the chemicals were used as received without any further purification. For the synthesis of $CsPbBr_3$ NCs, 10.0 mL ODE, 0.138 g $PbBr_2$, 1.0 mL OA and 1.0 mL OLA were loaded into a 50 mL three-necked flask, degassed and dried by applying vacuum for 1 h at 120˚C; after the solution became clear, the temperature was raised to 220 ˚C and 1 mL of cesium oleate solution was quickly injected. 5 s later, the reaction mixture was cooled down to room temperature in an ice-water bath. The solution was centrifuged for 10 min at 5000 rpm, and the obtained precipitate was redispersed in 5.0 mL of hexane, centrifuged down for 10 min at 10000 rpm, redispersed in 3.0 mL of hexane, centrifuged down again for 5 min at 12000 rpm, and redispersed in 1.0 mL of hexane.

6.3 Result and Discussion

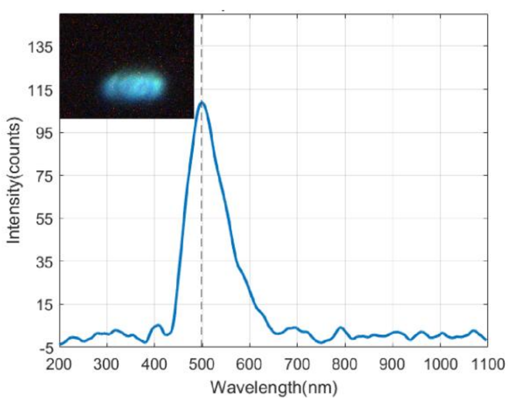

Figure 1. The PL spectrum of $CsPbBr_3$

The optical spectra of $CsPbBr_3$ was measured and is presented in Figure 1. A peak photoluminescence spectra was observed at 499 nm. However, significant noise and lower PL intensity under the integration time of 5s was recorded. The weak intensity might be due to a large amount of defects in the nanostructures formed during synthesis. This sample can not meet the requirements of the applications in LEDs not only because lower PLQY but also the PL, which is far beyond the blue color due to the big size in the NCs.

6.4 Conclusion

We aim to obtain the nanorods with high optical performance for the application in the LEDs, which means the PLQY of the NRs should be more than 50% in the solution. The CdS NRs, CdSe NRs, $CdSe_{1-x}S_x$ NRs can be synthesized successfully with a length of 20-200nm, in addition, the close-packaged vertically aligned $CdSe_{1-x}S_x$ film can be fabricated by EPD. However, the PLQY of all kind of NRs is lower than 5% which can not meet the requirement of the LEDs application.

The CdSe/CdS NRs exhibit high PLQY in films with tunable emission wavelength, which can be synthesized by controlling the size of the CdSe core. The NR-LED is fabricated successfully, especially the green NR-LED although it behaves a poor performance. The synthesis of blue NRs should be further studied, that is, the smaller size of CdSe core should be synthesized, the size of the core should be less than 2 nm then the blue CdSe/CdS NRs could be obtained with a thin shell according to our previous experience.

Perovskite NRs is one of the possible materials for the application in blue NR-LEDs, it is also worthy to try the further study of the synthesis. Also, EPD can be applied to the fabrication of blue NR-LEDs in the vertically aligned close-packaged NRs layer, which might improve the device efficiency.

Reference

1. Song, J., et al., Over 30% external quantum efficiency light-emitting diodes by engineering quantum dot-assisted energy level match for hole transport layer. Advanced Functional Materials, 2019. **29**(33): p. 1808377.
2. Helander, M., et al., Chlorinated indium tin oxide electrodes with high work function for organic device compatibility. Science, 2011. **332**(6032): p. 944-947.
3. Protesescu, L., et al., Nanocrystals of cesium lead halide perovskites (CsPbX3, X= Cl, Br, and I): novel optoelectronic materials showing bright emission with wide color gamut. Nano letters, 2015. **15**(6): p. 3692-3696.
4. Shamsi, J., et al., Metal halide perovskite nanocrystals: synthesis, post-synthesis modifications, and their optical properties. Chemical reviews, 2019. **119**(5): p. 3296-3348.
5. Huang, H., et al., Lead halide perovskite nanocrystals in the research spotlight: stability and defect tolerance. ACS energy letters, 2017. **2**(9): p. 2071-2083.
6. Shen, X., et al., Zn-alloyed CsPbI3 nanocrystals for highly efficient perovskite light-emitting devices. Nano letters, 2019. **19**(3): p. 1552-1559.
7. Mehetor, S.K., H. Ghosh, and N. Pradhan, Blue-emitting CsPbBr3 perovskite quantum rods and their wide-area 2D self-assembly. ACS Energy Letters, 2019. **4**(6): p. 1437-1442.
8. Guo, J., et al., Cd-Rich Alloyed CsPb1-xCdxBr3 Perovskite Nanorods with Tunable Blue Emission and Fermi Levels Fabricated through Crystal Phase Engineering. Advanced Science, 2020. **7**(15): p. 2000930.